UNIVERSIDAD
DE GRANADA

INSTITUTO de ASTROFISICA de ANDALUCIA
CSIC
I·A·A

Programa de Doctorado en Física y Matemáticas

Study of the chemical and morphological evolution of molecular clouds, using observations of high density gas tracers

Dissertation presented by:
Guillermo Manjarrez Esquivel

Advisors: Dr. José Francisco Gómez Rivero
Dr. Itziar de Gregorio Monsalvo

Granada, 2018

Agradecimientos

Agradezco a mis directores de tesis, José Francisco Gómez Rivero e Itziar de Gregorio Monsalvo por todo el apoyo que me proporcionaron para la realización de este trabajo.

Mi agradecimiento también para Guillem, Mayra, Ana Karla y los compañeros que formaron parte del grupo de Radioastronomía durante mi estancia en el Instituto de Astrofísica de Andalucía. De todos ellos aprendí mucho.

Igualmente agradezco al personal del IAA por todo el apoyo que recibí en el instituto.

También agradezco a los amigos y amigas que hicieron de mi estancia en Granada una gran experiencia de vida. Agradezco a mi familia, que me apoyó en todo momento.

Summary

Stars are formed in dense regions within molecular clouds. The different phenomena associated with the star formation processes may be characterized by studying its dust and gas content. The analysis of thermal emission of different molecular species is a powerful tool to characterize the physical, kinematical, and chemical properties of these regions. The abundance of some of these molecules changes as the clouds evolve. In this context, the so called "early-type molecules", such as CCS, have higher abundance in the first stages of cloud evolution than in star forming regions, while the opposite trend is seen in late-type molecules, such as NH_3 (Suzuki et al. 1992). Therefore, the abundance ratio $[CCS]/[NH_3]$ was proposed as an indicator of cloud evolution, with its value being higher for pre-stellar clouds and decreasing as star formation proceeds (Suzuki et al. 1992). However, in their study of the star-forming region B1-IRS, De Gregorio-Monsalvo et al. (2005) found some evidence that the production of CCS takes place not only at the earlier stages of the cloud evolution, but also at later stage, after the onset of star formation. This implied that the abundance ratio $[CCS]/[NH_3]$ may properly characterize the evolutionary stage of active star forming regions.

In this thesis we present a follow-up of these studies, analyzing the emission of CCS and NH_3 at small scales in a sample of molecular clouds at different stages of their evolution, from starless cores to active star forming regions. Our aim was to investigate if the spatial anticorrelation between CCS and NH_3 previously observed in B1-IRS at small scales ($\simeq 5''$) is present in other clouds and over a range of evolutionary stages. We also aimed at studying a possible CCS enhancement due to the interaction between the ambient dense gas and molecular outflows. Our sample included some dense starless cores in TMC-1, the very young star forming region GF9-2, and the region surrounding the protostars L1448 IRS3 and L1448C.

To carry out these studies, we observed the CCS and NH_3 emission in these regions at high angular resolution using the Very Large Array (VLA) interferometer. In addition, we observed other molecular tracers like CO and water masers to trace energetic mass-loss processes associated with young stellar objects in the studied regions, as well as continuum emission tracing dust (at millimeter wavelengths) and ionized gas (at centimeter wavelengths). These included data taken with the Effelsberg radio telescope and archival data from the Atacama Large Millimeter/submillimeter Array. Our data provided us with detailed information of the morphology, kinematics and physical conditions surrounding young protostars.

In the dark pre-stellar cloud TMC-1, our results showed that the cores B and D present a clear chemical differentiation. We found that the CCS-NH_3 anticorrelation stands even at small scales ($\sim 4''$) within each core. Core B showed intense NH_3 emission with filamentary structure, and seems to be in a relatively advanced stage of cloud evolution. We also found that the spacing between cores ($\sim$ 0.1 pc) is in agreement with the scale of fragmentation of collapsing cores in filaments derived from models. On the other hand, Core D presents CCS emission with a more clumpy structure, suggesting that this core is very young and less evolved than core B.

In GF9-2 (a cloud that contains a very young class 0 protostar that does not power an extensive molecular outflow), we found a clear CCS-NH_3 anticorrelation, with no evidence of CCS enhancement due to star-forming activity. We also identified a possible "blue spot" signature (as defined by Mayén-Gijón et al. 2014), suggesting the presence of infall and rotation. This is the first time this signature is found in a low mass star forming region. The protostar in GF9-2 is also the lowest luminosity young stellar object (YSO) for which a possible association with water maser emission has been reported, but our VLA observations could not confirm it. We then carried out observations of water masers in a sample of low luminosity YSOs and brown dwarfs, to find out the luminosity limit at which water maser emission can be produced. We did not detect any emission in our targets, which suggests that the correlation between water maser luminosities and bolometric luminosities does not hold at the lower end of the (sub)stellar mass spectrum.

In the L1448 region (an active star forming region that contains multiple YSOs and outflows) we also observed spatial anticorrelation between CCS and NH_3, around the YSO L1448C. The presence of relatively strong CCS cores close to the outflow trajectory suggests that the CCS abundance is enhanced by star-forming activity, like in B1-IRS. The velocity gradients of CCS and NH_3 have opposite signs south of L1448C, illustrating the complementarity of both molecules, and that observing only one of them would provide a biased view of the physical processes in the region. Using ALMA data we found a dust jet traced by millimeter continuum emission. This is the first time that thermal dust emission is detected in a jet, and traced up to its origin from a circumstellar disk. Our results suggested that jets can be powered by disk winds launched from a wide range of radii, as proposed in D-wind models. In this source, we also detected a Keplerian disk with $C^{18}O$ observations, with a radius $\simeq$ 450 au, which is larger than in other Class-0 protostars.

In AFGL 437 (a high mass star forming region with a poorly collimated outflow), we suggest that the low-collimation CO outflow could be the superposition of individual outflows from different sources, rather than being the interaction of the wind from a single object with an anisotropic environment, as previously suggested.

One of the main general results of the thesis is that the chemical evolution of molecular clouds (in particular, the abundance of CCS and NH_3) is not only a time dependent process, but also depends on different physical conditions present in advanced stages of the formation of a star. Therefore, the abundance ratio CCS-NH_3 may not be useful to study the stage of the evolution of active star forming regions with multiple YSOs and/or very energetic outflows, since their interactions with ambient gas may trigger CCS regeneration, which may provide misleading conclusions if a linear evolutionary interpretation is applied.

Resumen

Las estrellas se forman en las regiones más densas de las nubes moleculares. Los diferentes fenómenos asociados a los procesos de formación estelar pueden caracterizarse estudiando su contenido de gas y polvo. El análisis de la emisión térmica de diferentes especies moleculares y sus transiciones son una poderosa herramienta para caracterizar las propiedades físicas, cinemáticas y químicas de esas regiones. La abundancia de algunas de estas moléculas cambia conforme las nubes evolucionan. En este contexto, las llamadas "moléculas tempranas", como CCS, presentan una mayor abundancia en las primeras etapas de evolución de las nubes que en regiones de formación estelar, mientras que la tendencia opuesta se observa en las moléculas de tipo tardío, como NH_3 (Suzuki et al. 1992). Así, el cociente de abundancias $[CCS]/[NH_3]$ fue propuesto como un indicador de evolución de las nubes, siendo mayor para nubes preestelares y este disminuye al ir avanzando la formación estelar (Suzuki et al. 1992). Sin embargo, en su estudio de la región B1-IRS, De Gregorio-Monsalvo et al. (2005) encontraron evidencia de que la producción de CCS tiene lugar no solo en las etapas tempranas de la evolución de las nubes, sino también en etapas tardías, después de la formación de la estrella. Esto también implicó que el uso del cociente de abundancias $[CCS]/[NH_3]$ podría no ser útil para caracterizar apropiadamente la etapa evolutiva de las regiones de formación estelar activa.

En esta tesis continuamos con estos estudios, analizando la emisión de CCS y NH_3 a pequeña escala en una muestra de nubes moleculares en diferentes etapas de evolución, que van de núcleos densos sin estrella a regiones de formación estelar activa. Nuestro objetivo es investigar si la anticorrelación espacial entre CCS y NH_3 previamente observada en B1-IRS está presente en otras nubes y sobre un intervalo de etapas evolutivas. También estudiamos el posible enriquecimiento de CCS debido a la interacción entre el gas ambiente denso y flujos moleculares. La muestra contiene algunos núcleos densos de la nube TMC-1, la muy joven región de formación estelar GF9-2, y la región alrededor de las protoestrellas L1448 IRS3 y L1448C.

Para llevar a cabo estos estudios, observamos la emisión de CCS y NH_3 en estas regiones con alta resolución angular usando el interferómetro Very Large Array (VLA). Además observamos otros trazadores moleculares como CO y máseres de agua para trazar procesos energéticos de pérdida de masa asociados con objetos estelares jóvenes en las zonas estudiadas, así como la emisión del continuo trazadora de polvo (a longitudes de onda milimétricas) y gas ionizado (a longitudes de onda centimétricas). Estos incluyeron datos obtenidos con el radiotelescopio de Effelsberg y datos de archivo del Atacama Large

Millimeter/submillimeter Array. Nuestros datos nos proporcionaron información detallada de la morfología, cinemática y condiciones físicas alrededor de protoestrellas jóvenes.

En la nube oscura TMC-1, nuestros resultados mostraron que los núcleos densos B y D presentan una clara diferenciación química. Encontramos que la anticorrelación CCS-NH_3 se mantiene incluso a pequeñas escalas ($\sim 4''$) dentro de cada núcleo. El núcleo denso B mostró intensa emisión de NH_3 con estructura filamentaria, y parece estar en una etapa de evolución relativamente avanzada para una nube molecular. También encontramos que la separación entre los núcleos es de ~ 0.1 pc, valor consistente con la escala de fragmentación de filamentos en núcleos que podrían colapsarán, según algunos modelos. Por otro lado, el núcleo denso D presenta emisión de CCS con estructura grumosa, sugiriendo que este núcleo está en una etapa muy temprana de evolución y es menos evolucionado que el núcleo B.

En GF9-2 (una nube que contiene una protoestrella clase 0 que no presenta un flujo molecular extenso), encontramos una clara anticorrelación CCS-NH_3, sin evidencia de enriquecimiento de CCS debida a la actividad de la formación estelar. También identificamos un posible sello conocido como "mancha azul" (blue spot), que sugiere la presencia de rotación y colapso (según la definición de Mayén-Gijón et al. 2014). Esta es la primera ocasión que este sello se encuentra en una región de formación estelar de baja masa. La protoestrella localizada en GF9-2 es el objeto estelar joven (YSO) de menor luminosidad para el que se ha reportado una posible asociación con emisión de máser de agua, pero nuestras observaciones con el VLA no pudieron confirmarlo. Entonces llevamos a cabo una búsqueda de emisión de máser de agua en una muestra de YSOs de baja luminosidad y enanas marrones, para encontrar el límite de luminosidad en el cual la emisión máser puede producirse. No detectamos emisión alguna en nuestras fuentes, lo que sugiere que la correlación entre luminosidades de máser de agua y luminosidades bolométricas no se mantiene en la parte final baja del espectro de masa (sub)estelar.

En la región L1448, (una región de formación estelar activa que contiene múltiples YSOs y flujos moleculares) observamos la anticorrelación espacial entre CCS y NH_3 alrededor del YSO L1448C. La presencia de grumos relativamente intensos cerca de la trayectoria del flujo molecular sugiere que la abundancia de CCS es enriquecida en L1448C (como en B1-IRS). Por otro lado, los gradientes de velocidad de CCS y NH_3 tienen signos opuestos al sur de L1448C, ilustrando la complementariedad de ambas moléculas, y que observar solo una de ellas proporciona una visión sesgada de los procesos físicos en la región. Usando los datos de ALMA encontramos un jet de polvo trazado por la emisión del continuo milimétrico. Esta es la primera ocasión que la emisión térmica de polvo es detectada en un jet, y es trazada hasta su origen en un disco circumestelar. Nuestros resultados sugieren que los jets pueden ser generados por vientos del disco eyectados en un amplio intervalo de radios, tal como lo proponen los modelos D-wind. En esta fuente también detectamos un disco Kepleriano con observaciones de $C^{18}O$, con una Ley Kepleriana que se puede trazar hasta un radio de ~ 450 au, el cual es mayor que en otras protoestrellas clase 0.

En AFLG 437 (una región de formación estelar de alta masa con un flujo molecular de baja colimación) sugerimos que la baja colimación del flujo de CO podría ser el resultado de la superposición de los flujos individuales de diferentes fuentes, más que la interacción de un viento de un objeto individual con un ambiente anisotrópico, como previamente se sugirió.

Uno de los principales resultados de la tesis es que la evolución de las nubes moleculares (en particular, la abundancia de CCS y NH_3) no solo es dependiente del tiempo, sino que también depende de las diferentes condiciones físicas presentes en etapas avanzadas de la formación estelar. En consecuencia, el cociente CCS-NH_3 podría no ser útil como reloj químico en regiones de formación estelar con múltiples YSOs o con flujos moleculares muy energéticos. Esto debido a que las interacciones de los flujos con el gas ambiente podrían provocar la regeneración de CCS, lo que podría dar lugar a conclusiones equivocadas si se aplica la interpretación de evolución lineal.

Contents

Chapter 1

Introduction

1.1 Molecular clouds: the sites of star formation

Stars are formed in the molecular clouds that, in our Galaxy, are located in the spiral arms. Molecular clouds mostly consist of a mixture of molecular gas (mainly H_2) and dust grains, with typical temperatures of ~ 10 K (Shu et al. 1987; Heyer & Dame 2015). Giant molecular clouds (GMCs) are the largest (from ~ 20 to ~ 100 pc, Beuther et al. 2007) and more massive ($10^4 - 10^6$ $M_\odot$) structures of molecular gas in the Galaxy (Blitz 1993; Rice et al. 2016), and contain most of the galactic H_2. These giant clouds show a hierarchical structure, with smaller components seen inside the larger ones when observed with increasingly higher angular resolution (Bergin & Tafalla 2007). These substructures are dark clouds, clumps and dense cores, whose characteristics are shown in table 1.1. Clumps have a certain degree of velocity coherence, so they can be isolated both spatially and kinematically from the rest of the cloud. On the other hand, a core is gravitationally bound, and may potentially form a star or a system of stars by gravitational collapse (André et al. 2014). In this work, we will frequently refer to dense cores that do not contain a central protostellar object as “starless cores”.

More recently, filaments in molecular clouds have gained importance in star formation studies. These filaments are elongated structures of dust and molecular gas, significantly overdense with respect to their surroundings, which are clearly seen in Spitzer and Herschel images (see Fig. 1.1) at infrared and submm wavelengths (André et al. 2010; Palmeirim et al. 2013). The filamentary structures were known in previous works on other wavelengths (e.g. Schneider & Elmegreen 1979, Malinen 2012), but the Herschel observations have shown they are an important component of GMCs (Molinari et al. 2010). Filaments can be very long, with lengths of ~ 1 pc or more (André et al. 2014), up to several tens of pc in the case of some Infrared Dark clouds (IRDSs) (Jackson et al. 2010; Beuther et al. 2011). In general, filaments are quite linear, with minimal overall curvature and no sharp changes in direction (André et al. 2014).

The origin of these filamentary structures is still not well understood (André et al. 2014). Different models have been proposed to explain the formation of filaments, such as

Table 1.1: Characteristics of structures molecular clouds (adapted from Bergin & Tafalla 2007, Beuther et al. 2007, Blitz 1993).

	GMC	Clouds	Clumps	Dense Cores
Mass ($M_\odot$)	$10^4 - 10^6$	$10^3 - 10^4$	50-500	0.5-5
Size (pc)	$20 - 100$	2-15	0.3-3	0.03-0.2
Mean density (cm^{-3})	$50 - 100$	$50 - 500$	$10^3 - 10^4$	$10^4 - 10^5$
Temperature (K)	$10 - 15$	≈ 10	10-20	8-12
Examples	Orion	Oph, Musca Taurus	B213, L1709	L1544, L1498, B68 L1517B

colliding flows (Gómez & Vázquez-Semadeni 2014), cloud-cloud collisions (Klein & Woods 1998; Balfour et al. 2015), or gravitational instability of flattened clouds (e.g. Larson 1985, Curry 2000, Kuznetsova et al. 2018). Once filaments are formed they can be fragmented into smaller components (André et al. 2014) due to gravitational instabilities, to generate dense cores and clumps (the clouds where stars may be formed). For these reasons, filaments appear to be a main evolutionary stage during the formation of dense cores, clumps and stars (Beuther et al. 2015). Filaments have coherent velocity substructure (subfilaments) both in high- and low-mass star forming regions (André et al. 2014).

In this thesis, we will mainly deal with the early stages of star formation of low mass stars. Low and high mass stars are formed in molecular clouds located in different regions of the Galaxy (Shu et al. 1987). For example, clouds like Taurus, Perseus, Lupus and Auriga are sites of low mass star formation (Ungerechts & Thaddeus 1987; Dame et al. 2001), where stars form in dense cores. On the other hand, high mass stars are formed in clusters of stars spanning a wide range of masses (Beuther et al. 2007; Zinnecker & Yorke 2007). Examples of high mass star forming regions are the complexes of Orion and W3 (Maddalena et al. 1986; Thronson et al. 1985).

1.1.1 The star forming process

In our current understanding, the formation of stars may begin with the development of filaments inside molecular clouds, which get fragmented into clumps or cores (Schneider & Elmegreen 1979; Myers 2009; André et al. 2010; Beuther et al. 2015). These dense clouds are supported against gravitational collapse due a combination of magnetic, kinetic and turbulent pressure. However, gravitational instabilities can break this equilibrium, leading to a gravitational collapse. These instabilities may be related to shock waves, collisions or turbulence (Palous et al. 1994; Nakano 1998; Wang et al. 2004; Mocz & Burkhart 2018).

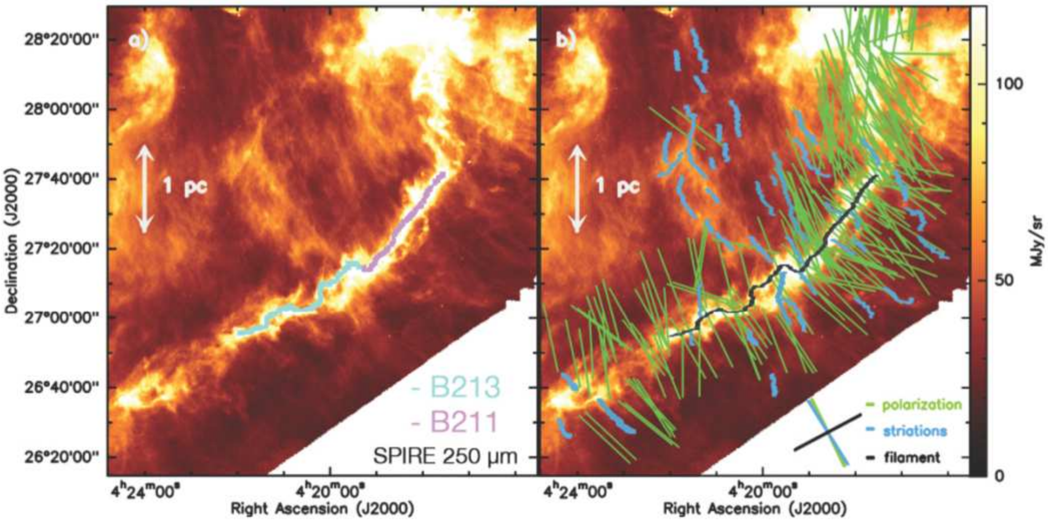

Figure 1.1: (a) Herschel/SPIRE 250 μm dust continuum image of the B211/B213/L1495 region in Taurus. (b) Display of optical and infrared polarization vectors tracing the magnetic field orientation, overlaid on the (a) image. Taken from Palmeirim et al. (2013).

To form a star, gravity must overcome the internal energy of a cloud. If we disregard the effects of magnetic field and turbulence, the maximum mass that this cloud may have without collapsing is given by the Jeans Mass (M_J, Jeans, 1902), which can be expressed as

$$M_J = 18 M_{\odot} T_K^{1.5} n^{-0.5}, \tag{1.1}$$

where T_K is the kinetic temperature (in K) and n is the particle density (in cm^{-3}). Once gravity overcomes pressure and magnetic forces, it collapses on a free-fall time-scale. In this stage, the evolution of the cloud will depend on its mass, according to the standard model of star formation, which considers the formation of high ($M_* \gtrsim 8$ $M_{\odot}$) and low mass ($M_* \lesssim 8$ $M_{\odot}$) stars separately.

In the standard model, high mass stars are quickly formed in massive dense clumps (Shu et al. 1987). They evolve so fast, that some of them can reach the main sequence while still actively accreting mass. (Kahn 1974; Beuther et al. 2007). On the other hand, low mass stars are formed in dense cores in quasistatic equilibrium (Shu et al. 1987), which are supported against collapse by a combination of thermal, kinetic and magnetic energies. These cores evolve slowly trough ambipolar diffusion, which let them increase mass, until the mass is enough to collapse (Shu et al. 1987; Mouschovias 1987; McKee et al. 1993; Machida et al. 2018).

The low mass star formation process is illustrated in Fig. 1.2. In this case, very quickly after the collapse started a centrifugal barrier will be produced, due to angular momentum conservation. This will prevent infalling material from accreting directly onto the protostar

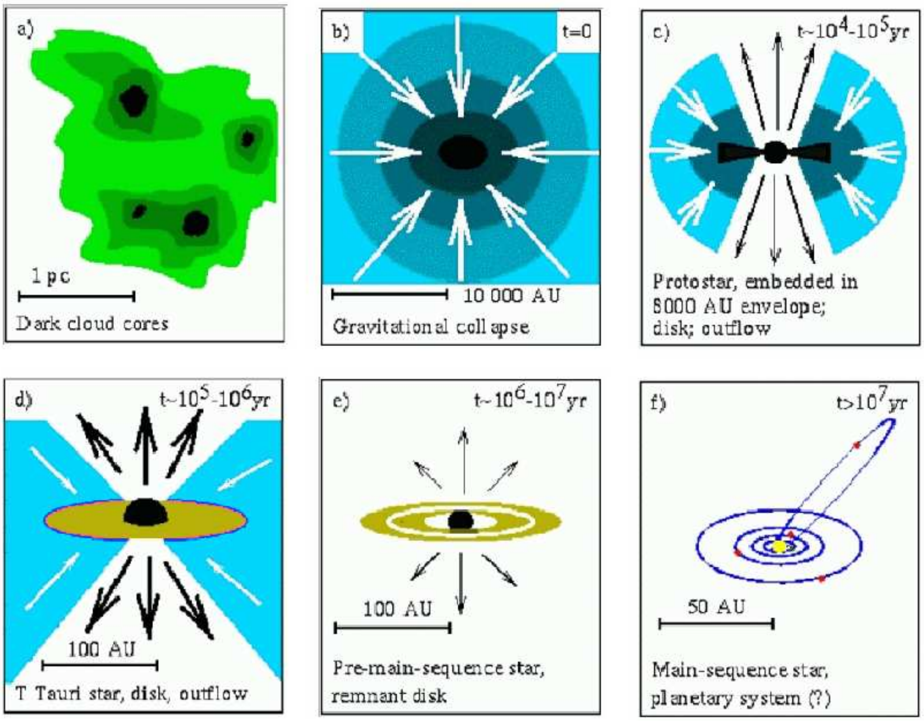

Figure 1.2: Schematic view of the low-mass star-formation process (taken from Hogerheijde 1998).

(Shu et al. 1987). Instead, the infalling material soon forms a highly flattened structure and then to a rotating disk surrounding the protostellar object (Shu et al. 1987), as shown in panel Fig. 1.2c. The diameter of these disks in the earliest stages can range from a few tens to several hundreds AU (Williams & Cieza 2011; Yen et al. 2017; Lee et al. 2018). Initially, the central temperature of the object is not enough to ignite nuclear reactions.

After most of the material has fallen into the disk, an accretion process begins. In this phase, the material of the disk is transported onto the central protostar (see Fig. 1.2 (d) and 1.3). This process requires transfer of angular momentum (Hartmann et al. 2016). In this stage, mass-loss process like winds, jets and outflows are experienced by the source. The presence of accretion processes and outflow activity appears to be correlated, given that outflows may be the agent to transfer angular momentum, which may facilitate the accretion. We will discuss about the mass-loss process in more detail in the next sections.

When the envelope is dispersed (Fig. 1.2 e), the disk contains only a few percent of the central stellar mass. It then evolves by experiencing diverse processes like viscous transport, grain growth, photoevaporation, etc. (Williams & Cieza 2011), which may lead to the formation of planetary systems (Fig. 1.2 f).

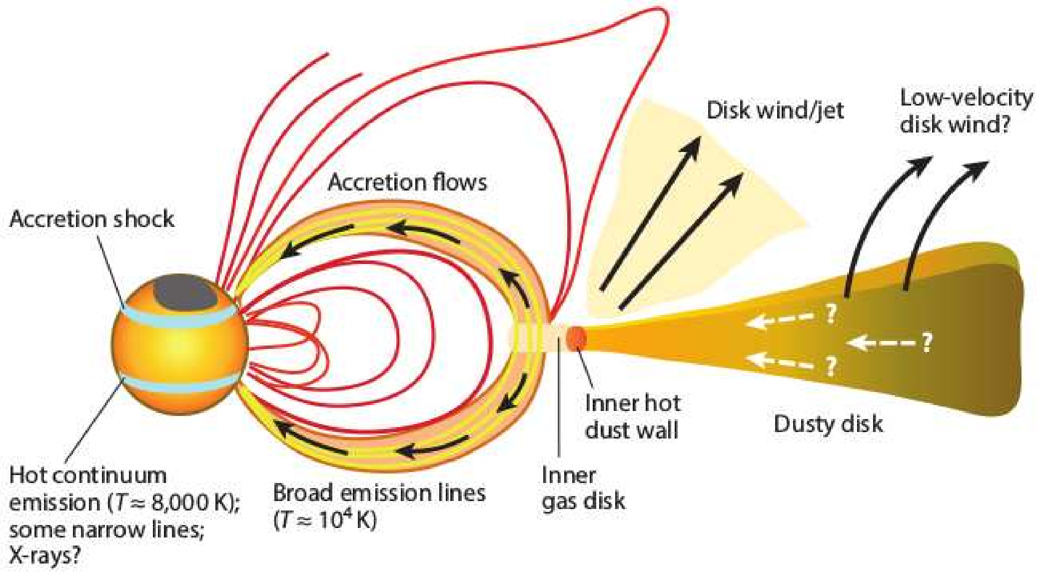

Figure 1.3: Schematic view of a young stellar source accreting from a disk through a stellar magnetosphere for low mass stars (~ 1 M$_\odot$). Taken from Hartmann et al. (2016).

1.1.2 Young stellar objects

In the earliest stages of the evolution of stars, young stellar objects (YSOs) are embedded in their surrounding envelope of dust and gas. Thus, the energy from the YSO heats up the dust of this envelope which is re-emitted in the infrared. The shape of the spectral energy distribution (SED) of YSOs has been traditionally used to classify them, based on the IR spectral index given by $\alpha_{IR} = d\log(\lambda F_\lambda)/d\log(\lambda)$. The different classes bear a relationship with their evolutionary stage.

Fig. 1.4 illustrates the YSO classification along with the spectral energy distribution. They are classified as:

1. Class 0.

   They have a SED resembling a single blackbody with low temperature (T< 70 K) (André et al. 1993; Chen et al. 1995). They are identified by their strong submillimeter emission (André et al. 1993), and do not present optical or near-IR emission (Williams & Cieza 2011). These objects are in the earliest detectable phase of low-mass stellar evolution. They are very young protostars, in which a hydrostatic core has formed but not yet accumulated the majority of its final mass (André 1995). They are deeply embedded in a circumstellar envelope (André et al. 2000), and acquire mass by accreting the material that surrounds them (White et al. 2007). They have an estimated age of $\sim 1-3\times10^4$ yr (André et al. 2000). We can identify bona fide class 0 objects by the presence of further evidence of protostellar activity, such as a collimated molecular outflow, an internal heating source or compact centimeter

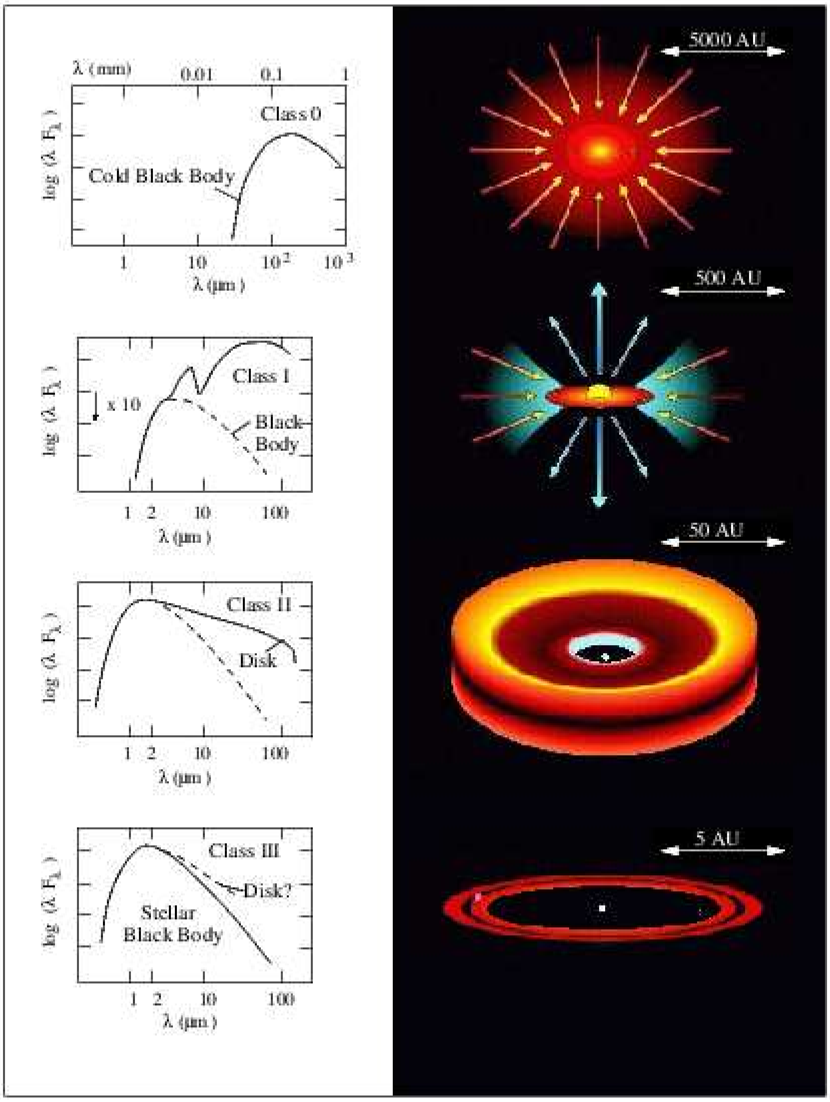

Figure 1.4: Evolution of YSOs, based in the description of Lada (1987) and André (1994). The left panels show the SEDs corresponding to each class from Class 0 to Class III sources (André 1994), and the right panels show a representation of their physical structure (van Boekel et al. 2006).

source (which may be tracing a jet, Anglada 1996, Anglada et al. 2018). Sources in this stage usually show the most powerful outflows (André et al. 2000).

2. Class I.

   The SED of these objects is broader than a blackbody and present an infrared excess. They are detected in the near infrared (André et al. 2000) and are characterized by $0 < \alpha_{IR} \leq 3$ (Lada 1987), but they are not detected in the optical. Class I objects are protostars still deeply immersed in their parental cloud, embedded within a envelope of circumstellar material, which is infalling, accumulating in a disk and being channeled to the protostar (White et al. 2007). These objects are in a more advanced stage of evolution than class 0 objects, with an estimated time in this stage of $1 - 2 \times 10^5$ yr (Kenyon & Hartmann 1995), and present a bolometric temperature $70 < T_{bol} < 650$ K (Chen et al. 1995). They are also associated to molecular outflows, but they are less energetic than in the previous phase (Bontemps et al. 1996; André et al. 2000).

3. Class II.

   These objects have a SED broader than a blackbody, and are characterized by $-2 < \alpha \leq 0$ (Lada 1987). They can be detected in the optical and in the infrared, with weaker emission in the latter than earlier classes. Class II objects are interpreted as pre-main-sequence stars with a circumstellar disk, but show little or not circumstellar envelope (White et al. 2007), given that their weaker IR emission indicates that they have less dust surrounding them than Class I objects. Their lifetime can range from a few times 10^5 yr to a few times 10^7 yr (André & Montmerle 1994) and have bolometric temperatures $T_{bol} \sim 650 - 2880$ K (Chen et al. 1995). Classical T Tauri stars belong to this class (Lada 1987).

4. Class III.

   They have a SED similar to a blackbody at a single temperature, > 2880 K (Chen et al. 1995; André et al. 2000), and are characterized by $-3 < \alpha \leq -2$. They are detected in the optical with little or no infrared excess emission. In these sources circumstellar disks are almost dissipated, either incorporated into the star or removed from its vicinity. Thus, they present no or very weak accretion. The lifetime of these objects are comparable to the lifetime of Class II sources (André & Montmerle 1994). Post T Tauri stars belong to this class (André & Montmerle 1994). These are the most evolved YSOs.

1.2 Outflows and jets in young stellar objects

Mass loss is observed during the early stages of star formation, both in low and high mass stars. YSOs produce accretion-powered ejections of material during their formation, with morphologies that range from jets to less collimated outflows and quasispherical winds. These ejections may be composed of atomic, molecular or ionized material over a wide range of excitation conditions, showing emission from ultraviolet to radio wavelengths. The unified scenario of molecular outflows explain that a jet sweeps gas surrounding the YSO, generating a molecular outflow.

1.2.1 Molecular outflows

Outflows of molecular gas were discovered through CO (carbon monoxide) lines (see section 1.3) in the mid-1970s (Kwan & Scoville 1976; Zuckerman et al. 1976), and their bipolar structure confirmed later (Snell et al. 1980; Rodríguez et al. 1980). Bipolar molecular outflows are commonly found in YSOs (Bally & Lada 1983; Lada 1985; Wu et al. 2004), which consist of two spatially separated lobes of material (one redshifted and the other blueshifted) moving away from an embedded YSO. They appear to be originated very close to the exciting source (for example at a distance of 25 AU in the outflow of the protostar TMC1A, Bjerkeli et al. 2016). It is thought that outflows consist of gas swept up by an underlying wind (Bachiller 1996; Frank et al. 2014).

Typical scales of outflows are $0.1 - 1$ pc (Arce et al. 2007), with kinetic energy that can reach $10^{47} - 10^{48}$ erg, and dynamical ages $\sim 10^3 - 10^5$ years (Bachiller 1996). The amount of mass in a molecular outflow can range from 10^{-2} to 200 $M_\odot$. The velocities of molecular outflows are typically < 30 km s^{-1}, although several highly collimated outflows exhibit high velocities (> 40 km s^{-1}, Konigl & Pudritz 2000; Frank et al. 2014).

The outflow activity seems to decline with time, given that the most energetic and collimated outflows are seen in class 0 YSOs (André et al. 2000; Arce et al. 2007), and they become less intense in later phases. Some characteristics observed in these objects (like morphology and velocity) depend on the tracer used to study them. The CO molecule, being the most abundant molecule after H_2, is the tracer more commonly used to study molecular outflows (Fukui et al. 1993; Wu et al. 2004). The low rotational transitions of CO are useful to trace outflows, while, at the other extreme, the higher transitions of CO along with molecules like SiO, H_2O are useful to study regions with high density and temperature, such as at the shock interface of outflows against their parent cloud.

1.2.2 Jets

In contrast with molecular outflows, a jet is a narrow, highly-collimated, bipolar structure of atomic or molecular gas with high velocities ($v \sim 100 - 1000$ km s^{-1}, Frank et al. 2014). These jets contain hot and ionized gas which may be detected in the optical, infrared or radio. They appear to be originated very close (< 50 AU) to the central protostar (Rodríguez et al. 1990b; Rodríguez & Reipurth 1994).

At optical and infrared wavelengths, jets can be observed with the emission of lines that traces ionized and shocked gas, for example the forbidden lines of [OI] $\lambda\lambda 6300, 6363$; [NII] 6583; [SII]$\lambda\lambda$ 6716, 6731, or recombination lines like Hα. Moreover, the H_2 emission in the near infrared traces shocks propagating into molecular gas (Bally 2016). The brightest of such lines is the $1 - 0$ S(1) line at 2.1 μm, which is excited in shocks with velocities of $10 - 50$ km s^{-1} (Bachiller 1996).

Radio continuum emission at centimeter wavelengths is frequently associated with YSOs. This emission is usually weak, compact (Anglada 1995, 1996), and elongated in the direction of the large scale outflow. It traces the region where the outflow is originated, very close to the exciting YSO. The radio continuum emission is interpreted as free-free emission from ionized, collimated outflows at the base of larger scale optical jets and molecular outflows (Rodríguez 1995). It is thought that the ionizing mechanism of the radio jet is related to shocks (Anglada 1996; Anglada et al. 2018). This type of structures are known as thermal radio jets.

Jets can also appear like a linear chain of bright knots, with characteristic optical line spectra, identified as Herbig-Haro (HH) objects (see for example the reviews of Reipurth & Bally 2001, Bally 2016 and references therein). These objects are observed in optical forbidden lines, hydrogen Balmer emission lines and radio continuum (Reipurth & Bally 2001). Typical tangential velocities are of the order of $100 - 200$ km s^{-1}, with velocities as high as 500 km s^{-1} (Reipurth & Bally 2001). Many HH jets have associated CO outflows, where the corresponding CO outflow have the same orientation, similar extension and compatible kinematics (Bachiller 1996). It is believed that HH objects are created when highly collimated jets interact with the surrounding material, heating and ionizing that material.

Early works assumed that the dimension of HH flows was around a fraction of a parsec (Reipurth & Bally 2001). However, some of these objects showed to be parsec-scale flows, called giant HH flows, for example HH111 with a total extent of $\sim$ 7.7 pc (Reipurth et al. 1997), HH34 of $\sim$ 3 pc (Bally & Devine 1994; Eisloffel & Mundt 1997), and HH355 with a total extent of $\sim$ 1.55 pc (Reipurth et al. 1997). They often terminate in a bow shock-like structure identified as the leading working surface where the jet impacts on a slower ambient gas (e.g., Raga et al. 2015).

1.2.3 Angular momentum in outflows

Observations suggest that there is a relationship between the accretion process and mass loss (jets, winds and outflows). For example, there is a correlation between the equivalent width of the [O I] λ6300 line of winds from classical T Tauri stars and the near-IR color excess of optically thick T Tauri disks (see Fig. 1.5), which suggests that the presence of energetic winds is coupled with the presence of optically thick circumstellar disks (Edwards et al. 1993). Additionally, the bolometric luminosity of protostars (which is dominated by accretion) correlates well with the mass-loss rate of outflows (Watson et al. 2016).

Other correlations support this link, for example the one between the momentum rate of molecular outflows (see Fig. 1.5) and the mass of the YSOs circumstellar material (Cabrit & Andre 1991; Bontemps et al. 1996). These relationships between properties of mass-loss and disks suggest that disks are necessary to drive winds. In this scenario, it is thought that accretion disks are the reservoir of momentum and energy that provides the mechanical power of molecular outflows (Bachiller 1996).

To explain how the angular momentum of the disk is transferred to the wind, several

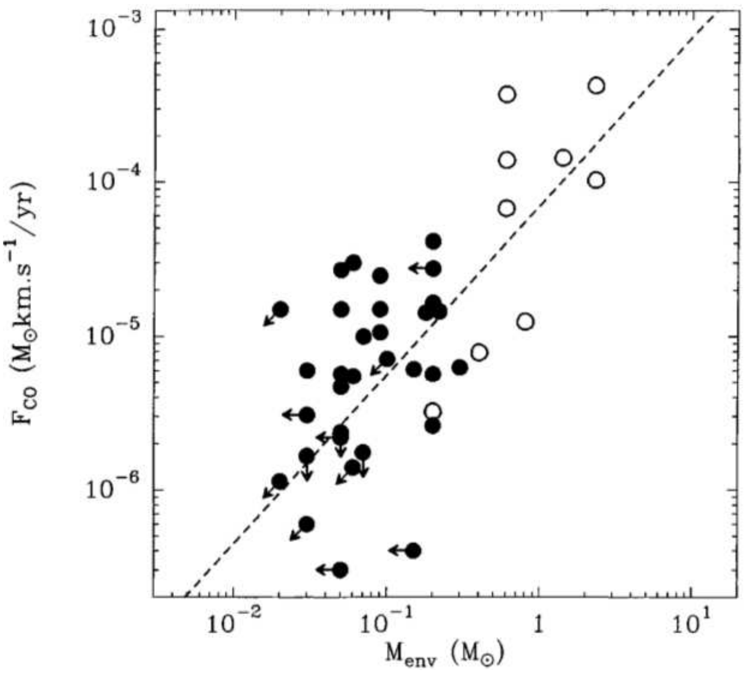

Figure 1.5: Rate of CO outflows vs circumstellar mass for a sample of Class 0 (open circles) and Class I (filled circles) YSOs. The dashed line represent the best fit $F_{CO} - M_{env}$ correlation for the entire sample. Taken from Bontemps et al. (1996).

models have been proposed (see for example Arce et al. 2007 and references therein). Wind-driven models explain that a wind blows the ambient material around the protostar, and forms the shell of swept-up material that characterize the outflow (Li & Shu 1996; Matzner & McKee 1999). These models consider that the launching process of the outflow takes place in a region that can be either located close to the protostar (X-wind models) or farther away in the protostellar disk (D-wind models).

X-wind models (see Fig. 1.6) explain that the flows emerge because the stellar magnetic field lines are inflated and opened up due to their interaction with the inner edges of the accretion disk, which let a centrifugal wind to flow along the field lines (Shu et al. 2000). The generated winds (X-winds) are collimated into jets, which interact with the surrounding material and produce the molecular outflows. In these models, stellar magnetic field lines transfer the excess angular momentum of the inflowing material to the inner sections of the X-region. This excess angular momentum is removed from the X-region by open field lines.

On the other hand, D-wind models consider that the outflow can be produced by centrifugally driven winds from disks (Konigl & Pudritz 2000). In these models, the wind is originated in open magnetic field lines distributed over a wide range of disk radii, which also allows the removal of angular momentum from the disk. In more recent studies, unified models consider both jet and winds scenarios, where a magneto centrifugal mechanism has

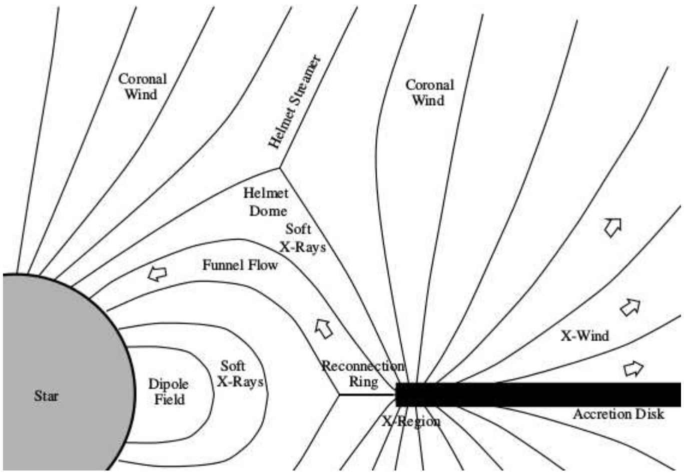

Figure 1.6: Schematic of the X-wind model. Taken from Shu et al. (2000).

a fundamental role to explain the production of flows in young stellar objects (Shang et al. 2007).

1.2.4 Effects of outflows in the chemistry of clouds

Outflows have significant impact in the chemistry of their parental cloud, because they propagate through the ambient medium creating shock waves (Arce et al. 2007; Bally et al. 2007). These waves compress and heat the material, which may trigger processes that usually do not operate in quiescent environments (Bachiller 1996; Richer et al. 2000). Outflows can inject momentum and energy into the surrounding molecular cloud at distances ranging from a few UA to up to tens of parsecs away from the source (Arce et al. 2007). They may induce enrichment of the chemical composition in the close vicinity of the YSO. For example, the abundance of certain molecules like SiO (Bachiller et al. 1991; Schilke et al. 1997), SO (Martin-Pintado et al. 1992; Bachiller et al. 2001), and CH_3OH (Sandell et al. 1994; Bachiller et al. 2001), is enhanced along the trajectory of molecular outflows.

1.3 Molecules and chemistry in star forming regions

Molecular clouds can be studied with the emission of dust and molecular transitions that trace the presence of H_2. The dust particles present in the clouds are composed of silicates and carbonaceous matter, with size that ranges from 10 nm to 1.0 μm (Davies et al. 2017). They absorb the radiation of wavelengths shorter than their size, and re-emit it as continuum emission at longer wavelengths. Dust emission can be useful to study some characteristics of clouds, like their structure or mass, but it does not provide any kinematic information.

Most of the gaseous component of these clouds (H_2) is not visible, given that the H_2 molecule has no permanent electric dipole moment, implying that no dipole rotational transitions are allowed. This is why other molecules that trace H_2 are observed instead, with CO being the most widely used (Bachiller 1996; Bolatto et al. 2013). To study the physical conditions and kinematics of molecular clouds the emission of molecules can provide significant information. Under typical conditions, molecular clouds (where $T_K \simeq 10$ K) provide the energy required to excite molecular rotational transitions (energies $10^{-3} - 10^{-4}$ eV, corresponding to radio wavelengths). Vibrational and electronic transitions require more energy to be excited and, in general, they are not observed in molecular clouds, except when excited in shocks.

Currently around 2000 molecules have been found in the interstellar medium or circumstellar environments (Endres et al. 2016), from diatomic molecules to molecules with more than 12 atoms. The most widely used molecule to study molecular gas in the interstellar medium is $^{12}C^{16}O$ (usually written as CO), which can be found in regions with relatively low densities ($\sim 100 - 1000$ cm^{-3}). It is the most abundant molecule after H_2, with CO/H_2 abundance ranging from 2.5×10^{-5} cm^{-3} (Rodríguez et al. 1982) to 10^{-4} cm^{-3} (Garden et al. 1991). At higher densities ($\gtrsim 10^4$ cm^{-3}) CO molecules may freeze onto dust grains (Bergin et al. 1995). Moreover, given its high molecular abundance, CO transitions quickly become optically thick. Thus, CO may not be useful to study the coldest, innermost, high-density regions of molecular clouds, where stars are formed (Bergin & Tafalla 2007). These regions can be studied with less abundant tracers (like CO isotopologues) or specific tracers of dense gas.

Molecular transitions that can be used as high-density tracers are those that are thermalized at a very high density. This is determined by the critical density, which represents the density at which the rates for collisional processes become comparable to those for radiative processes. It is expressed with $n_{crit} = A_{ji}/\gamma_{ji}$, where A_{ji} is the Einstein coefficient for spontaneous emission and γ_{ji} is the collisional deexcitation coefficient between levels j (upper) and i (lower). For densities higher than the critical density, the upper level is populated by collisions and the excitation temperature approaches the kinetic temperature. For example, the critical density for the CO $J = (1 \rightarrow 0)$ transition is $n_{crit} \sim 2200$ cm^{-3} (Bolatto et al. 2013), while tracers of high-density can be the inversion transition of NH_3 ($n_{crit} \sim 10^4$ cm^{-3}, Friesen et al. 2009), or transitions of N_2H^+, HC_3N, HCO^+ ($n_{crit} \sim 10^5$ cm^{-3}, Di Francesco et al. 2004, Herbst & van Dishoeck 2009).

The abundance of molecules changes during the different stages of star formation, as shown in Fig. 1.7. This is a schematic view of the star formation process, which indicates the characteristic molecules at each stage. In this figure, we see that molecular tracers in a star forming region may be associated with the physical conditions of each of their components. Indeed, the study of molecular species can also give us information about the evolutive stage of clouds. For instance, the presence of deuterated molecules can be used to identify clouds in early evolutive stage (Bacmann et al. 2003; Friesen et al. 2013).

Some molecules (called early type molecules) like CS, HC_3N, C_2H and CCS have higher abundance in the first stages of cloud evolution and therefore, are more easily detected in cold and pre-stellar dark clouds, being significantly less abundant in star forming regions.

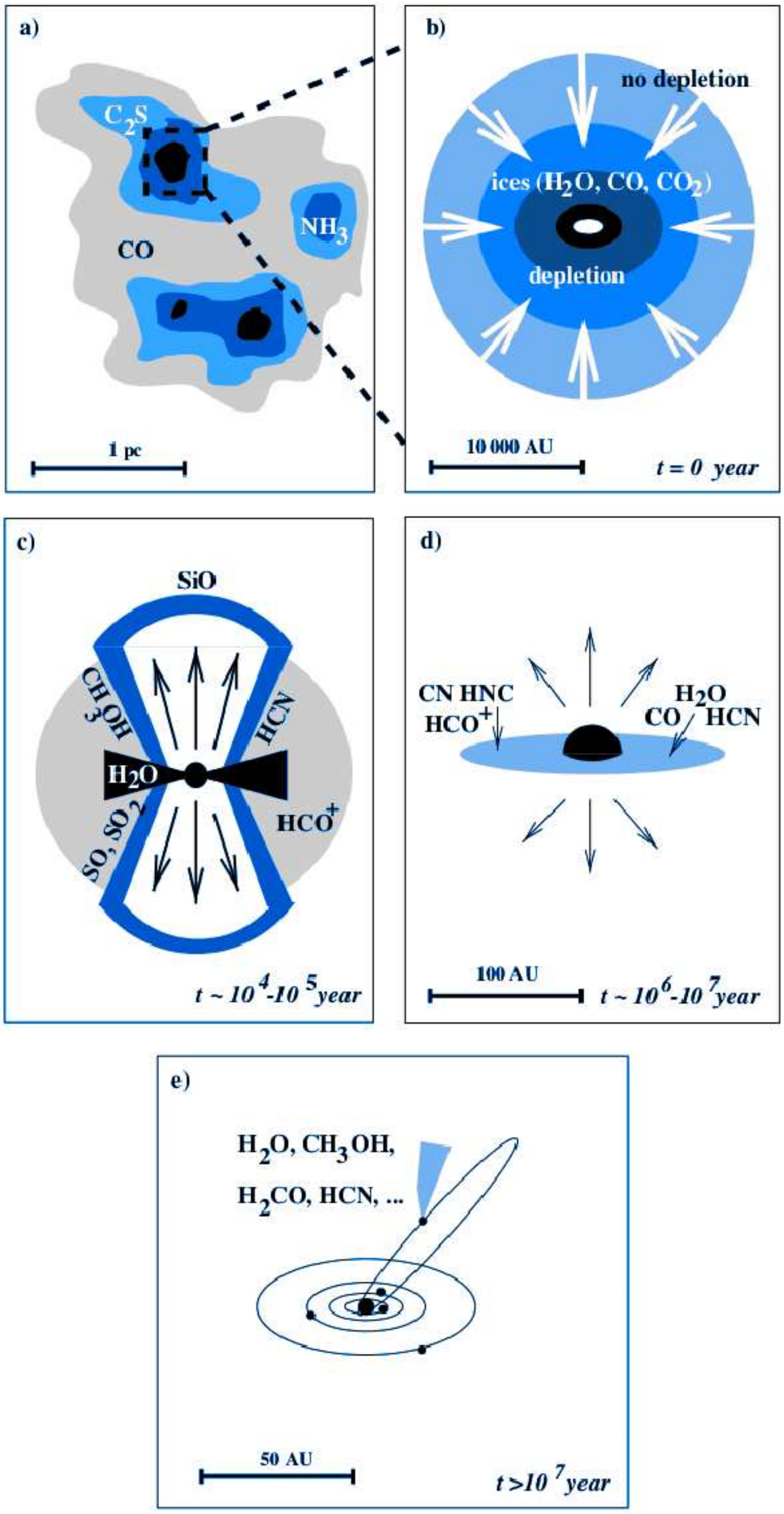

Figure 1.7: Molecules in star forming environments (Taken from Van Dishoek & Blake 1998).

On the other hand, late type molecules (like SO, SO_2, N_2H^+, NH_3) have higher abundance in active star forming regions, at later stages of cloud evolution (Suzuki et al. 1992).

To study the relation between chemical and physical evolution of dark clouds, Suzuki et al. (1992) observed a sample of dense cores with single dish in transitions of CCS, HC_3N, HC_5N (early type molecules) and NH_3 (late type molecule). They found that carbon-chain molecules correlated well among them, but not with NH_3. The CCS molecule was found abundant in cold quiescent dark clouds and was much less abundant in star forming regions. They proposed that if CCS is used in combination with a late-type molecule like ammonia (NH_3), the abundance ratio [CCS]/[NH_3] can be used as indicator of cloud evolution and star formation (Suzuki et al. 1992).

1.3.1 CCS and NH_3 in dark clouds and star forming regions

The CCS molecule (dicarbon monosulfide) is a linear molecule with useful transitions to study the physical conditions in dark clouds (Suzuki et al. 1992). It has no hyperfine structure, which simplifies the interpretation of its spectra. The critical densities of the most widely observed CCS transitions are 3×10^4 to 4×10^5 cm^{-3} (Wolkovitch et al. 1997). For the physical conditions of dark clouds, the lower rotational transitions of CCS can be excited. These include, for instance, the $J_N = 2_1 - 1_0$ and $J_N = 4_3 - 3_2$ transitions at 22 and 45 GHz, respectively.

Some transitions of CCS were first observed in cold, starless and quiescent cores through single-dish observations (Suzuki et al. 1992; Benson et al. 1998). Its lines were found to be intense and abundant in these sources. Thus, it was assumed that this molecule is abundant in starless cores, but it is soon destroyed when the star formation begins.

NH_3 is a pyramidal molecule, discovered in the interstellar medium by Cheung et al. (1968). It is a high density tracer, with a critical density for thermalization $n_{crit} \simeq 10^4$ cm^{-3} for the (1,1) inversion transition. The transitions of this molecule are commonly found in molecular clouds and active star forming regions of low and high mass, in structures like circumstellar envelopes (Ho & Townes 1983). More characteristics of these molecules can be found in the Appendix.

These two molecules were compared by Hirahara et al. (1992), who found a spatial anticorrelation between CCS and NH_3 in the Taurus Molecular Cloud 1 (TMC-1) at low spatial resolution ($\sim 74''$) using the Nobeyama single dish telescope. They found that Core B of TMC-1 had higher abundance of NH_3 while Core D showed higher abundance of CCS and cyanopolyynes, and interpreted the anticorrelation as due to the different evolutionary stage of the individual cores.

To explain the spatial anticorrelation between CCS and NH_3, Suzuki et al. (1992) proposed an scenario of chemical evolution of a contracting cloud core (see Fig. 1.8). This begins with an initially diffuse cloud, which contains atoms of C and S ionized by the interstellar ultraviolet radiation. When the core collapses and increases its density, CCS and carbon-chain molecules are formed efficiently. As the cloud continues to evolve, most of the carbon atoms in the central core are incorporated into CO molecules, while

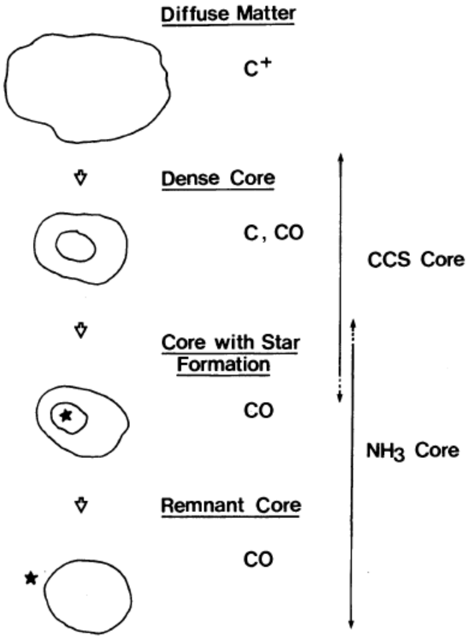

Figure 1.8: Proposed chemical evolution scheme of CCS-NH_3 (Suzuki et al. 1992).

the production of carbon-chain molecules becomes less efficient, and the overall result is that the abundance of the latter decreases. This chemical process takes place while NH_3 gradually becomes more abundant in the central part of the core.

Observations in regions like L1544 or L1498 (see Fig. 1.9) showed that CCS emission traces the outer regions of the cores but it is absent at their center (Ohashi et al. 1999). This suggested that CCS molecules can be depleted onto dust grains due to adsorption, or react with other molecules to produce CO, leaving a central hole of CCS emission (Aikawa et al. 2001; Bergin & Langer 1997). This results appeared to be consistent with the Suzuki et al. (1992) scenario, confirming CCS as an “early time” molecule.

However, CCS was also found in active star forming regions, like B335 and L483 (Velusamy et al. 1995; Hirota et al. 2010). Furthermore, in a sample of active star forming regions observed with single-dish, de Gregorio-Monsalvo et al. (2006) found several CCS-emitting Class 0 sources. Follow-up interferometric observations towards the Class 0 source B1-IRS (De Gregorio-Monsalvo et al. 2005) showed for the first time that the CCS-NH_3 spatial anticorrelation stands at small scales ($\sim 5''$). These observations revealed a velocity pattern around the YSO that may be related to the molecular outflow. This suggested that CCS might be locally enhanced via shock-induced chemistry. These results would imply that the CCS production could be triggered not only at first stages of the cloud evolution, but also at later stages, after the onset of the star formation. They also indicate that the use of the abundance ratio [CCS]/[NH_3] may not be straightforwardly used to trace cloud evolution.

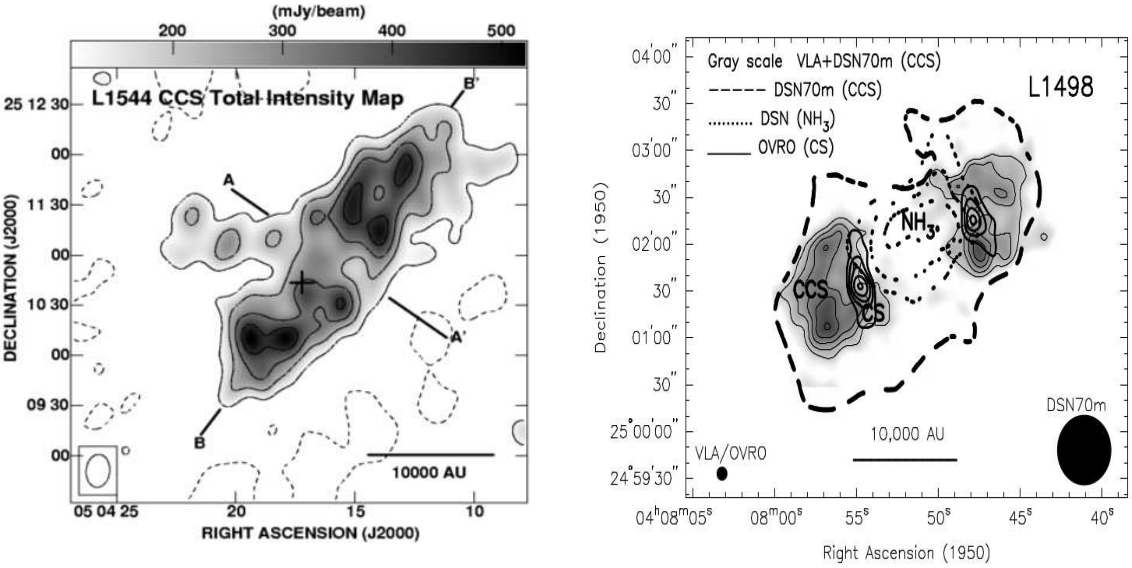

Figure 1.9: (Left) Map of L1544 observed with the BIMA array (Taken from Ohashi et al. 1999). (Right) Map of CCS, CS and NH_3 of the prestellar core L1498 (Taken from van Dishoek & Blake 1998).

Other studies also questioned the validity of this abundance ratio as an indicator of cloud evolution. For example, in a sample of 42 Bok globules (isolated clouds which may be forming stars) Marka et al. (2012) found [NH_3]/[CCS] abundance ratios that were roughly similar, regardless of the evolutionary stage, and suggested that this ratio alone cannot be interpreted as an evolutionary tracer.

For a sample of IRDCs, a type of cold ($T < 20$ K) and dense ($> 10^5$ cm^{-3}) clouds related to the formation of high mass stars and stellar clusters, Devine et al. (2011) found that CCS and NH_3 are spatially anticorrelated (with observations of $6''$ resolution), with NH_3 being present in high-density clumps, and CCS tracing lower-density envelopes around these clumps. Their results appear to be consistent with the chemical evolution suggested by Suzuki et al. (1992). However, the spatial location of some of their CCS peaks (at regions of subcloud-subcloud or outflow-subcloud interface) may suggest collisions could provoke desorption of CCS molecules from dust at these positions. This could indicate that some parts of the cloud may appear to be in an earlier stage of evolution (due to their higher CCS emission), when they are actually in a more advanced stage.

1.3.2 Motivation of this thesis

In this thesis we will study physical and chemical properties during the star formation process, mainly in low-mass star forming regions. For this purpose we will study YSOs and their ambient gas along different evolutionary stages. Our main tool of study will be molecular lines that trace high density gas ($> 10^3$ cm^3) at radio wavelengths, because they provide a wealth of information about the gaseous component of the clouds, in particular, their velocity structure, mass, and temperature. Moreover, a comparison between different tracers they provide information about the chemical evolution of clouds, given that the molecular abundance may change with cloud age, or as a consequence of several physical process present in star forming environments (like the presence of outflows, collapse, shocks, etc.).

Our main tools in this thesis were observations of transitions of CCS and NH_3 molecules, as tracers of different stages of evolution of young stellar objects. These data were obtained with the Very Large Array (VLA) interferometer, at high angular resolution ($4 - 10''$). We combined these interferometer CCS data with single-dish observations of the same molecule obtained with NASA's Goldstone 70-m antenna in one of our target sources. We also present molecular line data of CO and continuum emission tracing dust (in the millimeter rage) obtained from the public archives of the Atacama Large Millimeter Array (ALMA), as well as continuum emission in the centimeter range, tracing ionized gas, from the VLA archive. Finally, we processed H_2O maser we obtained with the VLA and the Effelsberg antenna.

In particular, we intend to study:

- The mutual interaction between the ambient dense gas with that of the molecular outflow and test whether the enhancement of the CSS observed in regions interacting with molecular outflow is a local phenomenon located at small scales.
- Whether the CCS-NH_3 spatial anticorrelation previously observed in the YSO B1-IRS is present in throughout different evolutionary stages, from starless cores to other young objects.
- The chemical process responsible for the anticorrelation observed between the CCS and the NH_3 in active star forming regions.
- The feasibility of the use of the ratio between CCS and NH_3, as an indicator of chemical evolution.
- The conditions of core collapse and jet launching in YSOs, at scales of a few hundred AU.

For this purpose we selected a sample of regions in different stage of evolution, from dense starless cores to active star forming regions, and are presented in different chapters sorted by increasing relative age. Two of our targets (GF9-2 and L1448C) where chosen since they are star forming regions with intense emission in transitions of CCS and NH_3 based on the single-dish surveys of De Gregorio-Monsalvo et al. (2005) and Suzuki et al. (1992).

We start this thesis (chapter 2) with a review of the challenges faced when mapping extended emission using an interferometer, and a description of the techniques used for this mapping. During the data processing for this thesis we had make use of these techniques, as the total extent of the emission in some regions we studied is larger than the VLA could properly sample.

In chapter 3, we present our observations of TMC-1. This is a filamentary dark cloud which does not contain any YSOs, molecular outflows or other significant sign of protostellar evolution. These characteristics make TMC-1 a well-suited region to study the physical and chemical conditions in a very early stage of molecular cloud evolution. In particular, we could measure the spatial scales of filament fragmentation that will eventually give rise to collapsing cores.

GF9-2 (chapter 4) is a cloud that contains a very young class 0 source, but it does not yet power an extensive molecular outflow. Thus we could study dense gas around an object that is in an early stage of stellar evolution, without the disturbances of an outflow. In particular, we were able to trace possible collapse motions.

GF9-2 is also the lowest luminosity YSO in which water maser emission (a tracer of shocks) has been reported (but using a single-dish telescope). Our interferometric observations could not confirm that this object is associated to this type of emission. This prompted us to carry out a sensitive search for it in other low-luminosity YSOs and brown dwarfs, to probe the low-luminosity limit at which water maser emission can be produced. This survey is presented in Chapter 5.

L1448 (chapter 6) is a star-forming region that contains multiple YSOs and outflows (including both Class 0 and I objects). Thus, we studied the CCS and NH_3 emission in a region with intense star-forming activity, to compare it with the more quiescent targets in the previous chapters. In particular, we could test whether outflows can re-enhance the CCS abundance.

One of the class 0 YSOs in this region (L1448C) is studied in detail in chapter 7, using ALMA data with an angular resolution of $\simeq 0.4''$. These observations allowed us to study the protoplanetary disk around it and trace the origin of the collimated jet all the way up to the disk surface. We obtained the first direct evidence of dust in the body of a jet, and discussed its implication for models of jet ejection.

In chapter 8 we will extend our research to the study of the outflow process in the high-mass star forming region AFGL 437. We intended to test whether the outflow in the region is intrinsically bipolar, or its morphology is just a projection effect, as proposed in previous works. We obtained additional information to determine the main energy source in the region.

Chapter 2

Observing extended emission with radio interferometers

Molecular line emission from molecular clouds can be very extended. For example a dense core can reach up to $\simeq 0.2$ pc, which would represent $\sim 300''$ at the distance of the Taurus molecular cloud (140 pc). These angular scales can be mapped with single-dish radio telescopes, although with a relatively low angular resolution (between $30-40''$ at 1.3 cm for the GBT and the Effelsberg radiotelescopes). When these clouds are observed with interferometers (to obtain images of higher angular resolution), there are some problems that limit the size of the region that can be properly mapped.

One is known as the "short spacing problem", which refers to the limitation imposed by the shortest distance between any pair of antennas in the interferometer. The largest angular scale an interferometer can sample is $\theta \sim \lambda / r_s$ where r_s is the shortest baseline. Therefore, structures with larger angular scales will be missed. The short spacing problem can be solved complementing the interferometer observations with the data from a single dish antenna, and/or a more compact interferometer.

The other limiting factor when observing extended emission is the antenna primary beam. Each antenna of an interferometer receives radiation from a limited solid angle on the sky. This imposes an obvious constraint to the field of view that can be observed with and interferometer. This is usually quantified with the primary beam size, which is the full width at half maximum (FWHM) of the beam pattern of the individual antennas. To observe objects more extended than the primary beam size, we can perform several pointings around the source to create a mosaic, which would allow us to cover larger areas.

Depending on the specific target region and the interferometer used, we may need one or both these techniques (combination with single-dish data and/or mosaicing). In this chapter we will analyze how the extended emission is observed with interferometers and single dishes, and how the resulting data can be mutually complemented. We begin the chapter with some basic concepts of the operation of radio interferometers, which are described in more detail in references such as Thompson et al. (2001), Taylor et al. (1999) and Rohlfs & Wilson (2010).

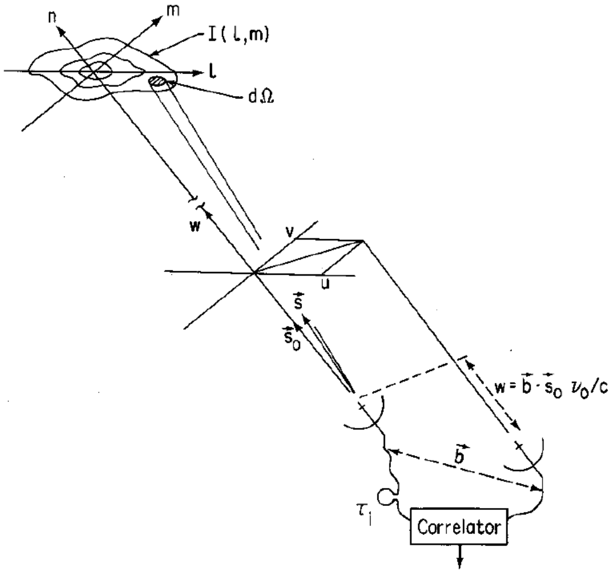

Figure 2.1: A two element interferometer with the coordinate systems used in interferometry. Taken from Taylor et al. (1999).

2.1 Some definitions

An aperture synthesis radio telescope (a radio interferometer) is a device to measure the coherence function of a sky brightness distribution. The components of a two element interferometer are represented in Fig. 2.1, that shows two parabolic antennas separated by a distance $\vec{b}$ (the baseline) pointing towards a source in the sky with direction $\vec{s}_0$ (called phase tracking center). The sky source has a brightness distribution $I(l, m)$, where the coordinates (l, m) are defined on a tangent plane at the observed position. This plane (known as the image plane) represents a projection of the sky sphere at that point.

The projection of the interferometer baselines on the sky define a plane called $u - v$ plane or spatial frequency plane. A wavefront from the source arrives at each antenna with a different time delay (τ). The signals are recorded and sent to the correlator. For a source with a brightness distribution $I(l, m)$, the response of an interferometer can be expressed with the visibility $V(u, v)$ function defined as

$$V(u,v) = \iint I(l,m)A(l,m)e^{-2\pi i(ul+vm)}dl\ dm \tag{2.1}$$

where $A(l, m)$ is the normalized antenna reception pattern or primary beam of the antennas, which describes the relative sensitivity as a function of the angular separation from the phase center of the observation. The field of view of an interferometer is limited by the size of the primary beam, which depends on the observing wavelength and the size of each antenna by

$$\theta_{\rm pb} \simeq \lambda/D \tag{2.2}$$

where $\theta_{\rm pb}$ is the FWHM of the primary beam, λ is the wavelength, and D is the diameter of the antennas.

Equation 2.1 can be inverted to

$$A(l,m)I(l,m) = \int\int V(u,v)e^{2\pi i(ul+vm)}du\ dv \tag{2.3}$$

where the visibility V has a complex value, with units of flux density (Jansky, 1 Jy $= 10^{-23}$ erg s^{-1} cm^{-2} Hz^{-1}) and I has units of surface brightness (flux density per unit solid angle).

Most interferometers are composed of more than two antennas, which may be distributed over different type of arrays (e.g., linear, bidimensional, etc.). The antennas may be separated by distances ranging from the antenna diameter to much larger distances. For example the shortest and largest baselines of the most compact VLA antenna distribution (its D configuration) are 35 m and 1 km, respectively.

2.2 Effects of sampling in the $u - v$ plane

In the $u - v$ plane, the observations performed with an interferometer provide samples of the visibility function $V(u,v)$ over distances varying between shortest baselines (the minimum antenna separation) to the longest ones. The largest baseline d determine the spatial resolution of the interferometer to $\theta_{\rm beam} \simeq \lambda/d$, which implies that, for larger antenna separations, an interferometer would give higher spatial resolution. On the other hand, the shortest baselines (r_s) determine the largest angular scales visible to the interferometer to $\theta_{\rm las} \simeq \lambda/r_s$. The lack of visibilities at distances shorter than r_s is known as the “short spacing problem”.

The visibility function is measured only at a finite number of points in the $u-v$ plane, which can be represented by the sampling function $S(u,v)$. The value of this function is one at the sampled points of the $u-v$ plane, and zero elsewhere. Using $S(u,v)$ in equation 2.3 we obtain:

$$I_\nu^D(l,m) = \iint V(u,v)S(u,v)e^{2\pi i(ul+vm)}du\ dv \tag{2.4}$$

Where I^D is known as the dirty image. The Fourier transform of the sampling function is the dirty beam or the point source response of the interferometer:

$$B(l,m) = \iint S(u,v)e^{2\pi i(ul+vm)}du\ dv \tag{2.5}$$

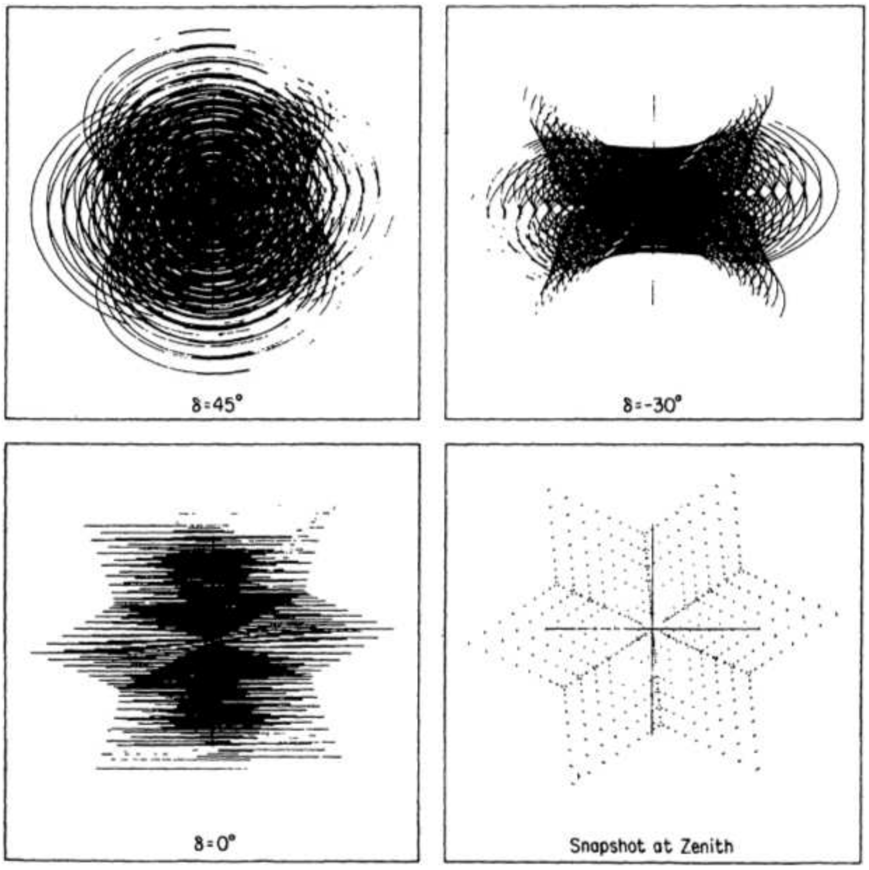

Figure 2.2: Coverage of the $u-v$ plane with the 27 antennas of the VLA. Long tracks for $\delta = 0°$, $\delta = 45°$ and $\delta = -30°$. The coverage of a snapshot observation is also shown in this Fig. (taken from Taylor et al. 1999).

This expression shows that the $u-v$ coverage determines the beam shape, and therefore, the response of the interferometer to the sky brightness distribution. The $u-v$ coverage of an interferometer shows empty regions or holes, that are not sampled. For example, an earth-tracking interferometer samples baseline projections following elliptical tracks in the $u-v$ plane. Then, a $u-v$ coverage of this instrument would show gaps between these elliptical tracks, and also at the origin of the plane.

In Fig. 2.2, we show the $u-v$ coverage for a snapshot and long-track observations performed with the VLA. The $u-v$ coverage of the snapshot observations is sparse and clearly shows a hole at the center of the $u-v$ plane. The longer observations have a better $u-v$ coverage than the snapshot, but they still have gaps or holes in the sampling. The coverage is determined by the array configuration, the source position and the length of the observation. Moreover, when the data is edited, the coverage may change due to flagging of baselines, antennas, time intervals, etc., modifying the $u-v$ coverage, and thus the dirty beam.

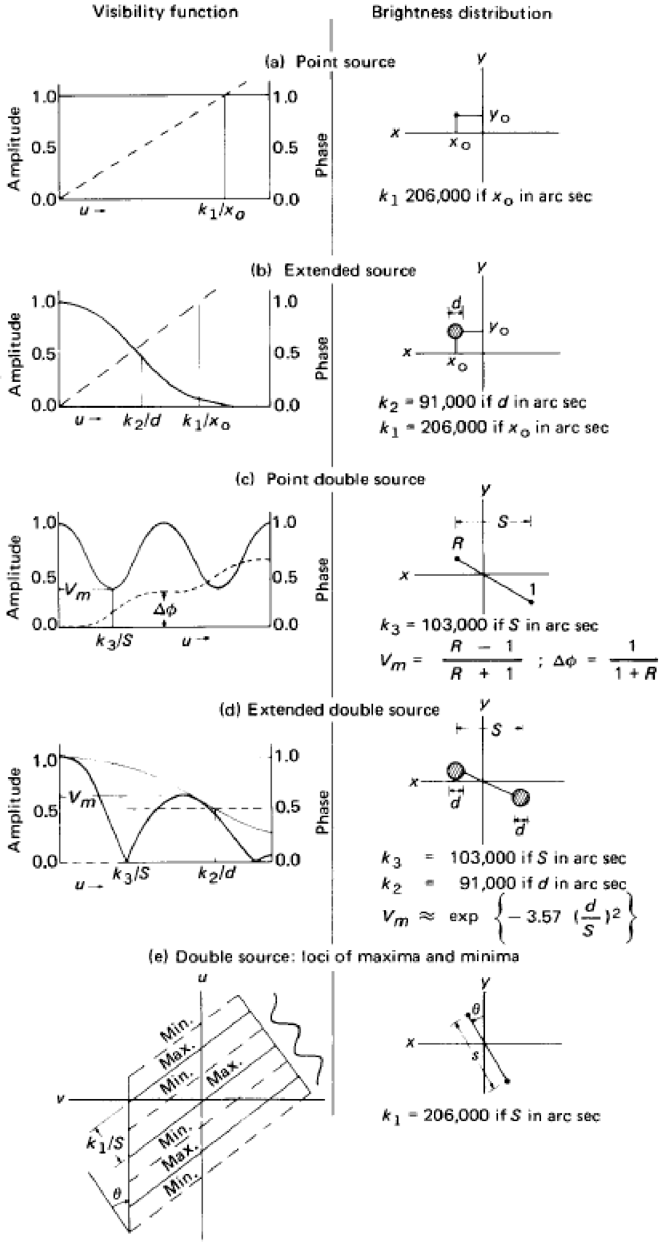

Figure 2.3: Visibility functions for some brightness distribution models (taken from Taylor et al. 1999).

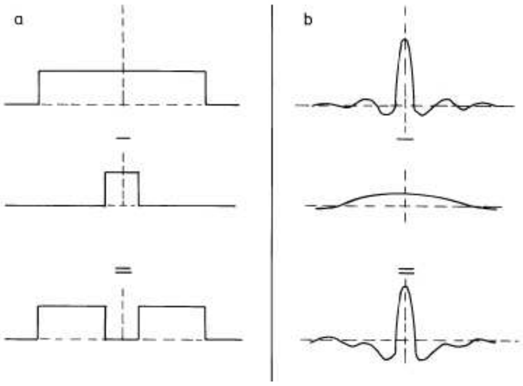

Figure 2.4: The instrumental response to the missing short spacings (from Braun & Walterbos 1985).

The impact of the missing short spacings can be seen through the visibility functions of different brightness distributions, like the ones shown on Fig. 2.3. A point source show visibilities with constant amplitude for all $u-v$ distances (panel a), while the visibilities of an extended source (panel b) have higher amplitudes at short $u-v$ distances. Therefore, the lack of visibilities at positions close to the center of the $u-v$ plane means that an interferometer would recover only a fraction of the total flux of an extended source. Since short $u-v$ distances correspond to large angular scales in the brightness distribution, the central hole in the $u-v$ plane limits the largest scale that an interferometer can map. This problem can seriously hinder certain observations. For example, in the observations of Pety et al. (2013), Langer et al. (1995) and De Gregorio-Monsalvo et al. (2005) it is estimated that the interferometer missed up to 90% of the actual flux density of the source.

The incomplete coverage of the inner region of the $u-v$ plane may cause strong negative sidelobes in the dirty beam as exemplified in Fig. 2.4. In the left panels (a), we see plots of $u-v$ coverages (sampling functions), and in the right ones, (b), we see their corresponding instrumental response to a point source. An ideal coverage (short spacings included) is shown at the upper left panel, whose response show negative and positive side lobes around the main lobe. The $u-v$ coverage with an incomplete sampling is shown at the bottom panels. The result in this case is a dirty beam where the negative lobes become more pronounced than in the one with full $u-v$ coverage.

Negative sidelobes can be easily removed from a map in the case of a point source, by applying deconvolution, for instance, with the CLEAN algorithm (Högbom 1974). However, for extended sources, deconvolution does not work as efficiently, and negative features cannot be properly accounted for.

2.3 Techniques to map extended emission with interferometers

As mentioned before, to map a region larger than the primary beam of the interferometer, one can observe multiple pointings to create a discrete mosaic that covering a larger total area (Sault et al. 1996), although this may only retrieve a fraction of the total flux. In this kind of mosaic, the sampling pattern and the spacing of the pointing centers determine the sensitivity of the final combined image. We applied this mosaicing in the observations presented in Chapters 3 and 6. The data processing of this technique is implemented in the synthesis imaging tasks of the major software packages for interferometry (e.g., CASA or AIPS).

On the other hand, it is possible to recover (or at least estimate) the missing visibilities of an interferometer if they are measured by other instrument (like a single dish or a more compact interferometer). If we have single dish observations, we can recover the total flux of the source. Therefore we may produce images having the higher angular resolution of the interferometer, and the total power and larger scale given by the single dish mapping.

In the rest of this section we will discuss some aspects of the combination of single dish and interferometer observations. Its practical implementation is more complex and less straightforward than mosaicing, so a detailed description is useful as a guidance for this and future works.

2.3.1 Combination of single-dish and interferometer data

The impact of missing short spacings can be alleviated with the combination of single-dish and interferometer data. Some techniques involve the combination in the image domain (Stanimirovic 2002), while in others it is performed in the $u-v$ domain (Bajaja & van Albada 1979; Vogel et al. 1984; Rodríguez-Fernández et al. 2008; Kurono et al. 2009). In this work, we have focused on the data combination in the $u-v$ domain.

In the case of the interferometer, the sampled visibility function can be expressed as

$$V_s(u,v) = \{V_{tr}(u,v) * a_I(u',v')\}S(u,v) \tag{2.6}$$

where a_I and $V_{tr}(u,v)$ are, respectively, the Fourier transforms of the primary beam pattern of the interferometer antennas (A) and of the true brightness distribution (I), and S is the sampling function. The symbol "*" the denotes the convolution product.

On the other hand, the brightness distribution observed with a single dish can be written as:

$$I_{obs}(l,m) = [I_{tr}(l,m) * B_{sd}] \cdot S_{sd}(l,m) \tag{2.7}$$

where $I_{obs}(l,m)$ is the measured brightness, I_{tr} is the sky true brightness distribution, B_{sd} is the single-dish beam and $\mathrm{S}_{sd}(l,m)$ is the sampling grid of the single dish observations. The Fourier transform of this equation can be written as

$$V_{obs}(u,v) = [V_{tr}(u,v) \cdot b_{sd}(u,v)] * s_{sd}(u',v') \tag{2.8}$$

If Nyquist (or better) sampling is used in the single dish mapping, for the (u,v) range of interest (Bajaja & van Albada 1979; Vogel et al. 1984) we can ignore the s_{sd} term and write:

$$V_{tr}(u,v) = V_{obs}(u,v) / b_{sd}(u,v) \tag{2.9}$$

where the term b_{sd} is a continuous function with values up to D (the antenna diameter).

Finally, when substituting 2.9 in 2.6, we obtain data values that can be combined with the visibilities of the interferometer

$$V_s(u,v) = \{[V_{obs}(u,v) / b_{sd}(u,v)] * a_I(u',v')\} s_I(u,v) \tag{2.10}$$

Then, given a single dish antenna with radius larger than the separation of the interferometer's antennas we can merge the "visibilities" obtained from our single dish data with the ones of the interferometer. The resulting data set can then produce an image using standard imaging routines in interferometry.

2.3.2 Practical considerations

Several aspects of the observations should be taken into account to generate the visibilities from the single dish data and to combine them with the ones of the interferometer. The specific steps could vary from case to case, depending on the telescopes used, the observation strategy, the software used to process the data, etc.

Some general considerations for this combination are:

1. The single dish antenna should have a diameter larger than the length of the shortest baseline of the interferometer (at least twice), to have enough overlap of spatial frequencies between the interferometric and single-dish data. This is important to properly match the flux scale of both data sets, whose calibrations may differ by some offset. For instance, in the case of the D configuration of the VLA with dmin=35m, a single dish of diameter $\geq$ 70 m can provide a good overlap. Useful antennas in this case would be the Green Bank Telescope (100 m), the Effelsberg radiotelescope (100 m) and the 70 m antennas of NASA's Deep Space Network.

2. To avoid degradation of the spectral resolution, the two data sets should have the same resolution. Therefore, the data set with the highest spectral resolution should be smoothed.

3. The single dish map should be Nyquist-sampled or better, in order to avoid aliasing.

4. The size of the area sampled with the single dish should be larger (about twice) than the area of the primary beam of the interferometer, to avoid the edge effects of the Fourier transform.

5. The visibilities of the interferometer and single dish should have comparable signal-to-noise ratio in the region of overlapping (Vogel et al. 1984), to avoid degradation of the combined map.

2.3.3 Combination process

To obtain the single-dish visibilities, we need to follow several steps. For example, once we have the calibrated single-dish data set, the next step is to grid the data into a regular mesh.

Frequently, the following step is to make a soft fall to zero at the edges of the single-dish map using a window function (apodization). A way to do this is to create a larger image of the map by convolving the gridded map with a Gaussian of FWHM similar to the one of primary beam of the interferometer.

Later, a Fourier transform is applied to the gridded data, which converts it into spatial frequencies in the $u - v$ plane. Assuming a good knowledge of the single dish beam, our single dish data is then deconvolved from the beam by dividing the gridded data by the Fourier transform of the beam. Finally, the data is transformed to the image plane, where it is multiplied with the interferometer primary beam.

In order to obtain the visibilities on a regular grid, the data is transformed back to the $u - v$ plane and gridded. The visibilities are calculated for $u - v$ distances from 0 to $D - d$, where d is the diameter of the interferometer antennas, and D is the diameter of the single dish. At this point, we can combine the resulting single-dish visibilities with the interferometric ones, and proceed with imaging and deconvolution in the usual way used with interferometric data.

2.3.4 Relative calibration

Before merging the interferometric and single dish data, it is necessary to compare their flux scales, as they may show some difference in the flux calibration (for example due to offsets in the flux calibration, quality of the gain calibrators, etc.). Ideally, one could observe an unresolved, non-variable source both with the single dish antenna and the interferometer, to obtain a reliable correction to the flux density scale between the interferometer and the single-dish data:

$$f = \frac{S_{int}}{S_{sd}} \tag{2.11}$$

However, is often difficult to find the appropriate source for this flux correction, specially in the case of molecular line observations. A more practical approach is to estimate

f by comparing the amplitude of the visibilities in the region where the ones of the single dish and the interferometer overlap. As indicated before, this step requires that the single dish has a diameter at least twice the length of the shortest interferometric baseline. This requirement may be difficult to accomplish for some interferometers and their configurations. A possible solution is to use the data of more compact interferometer arrays to reduce the hole in the center of $u-v$ plane, and use a single dish of smaller size to further improve the $u-v$ coverage.

2.3.5 Relative weighting

When combining the data in the $u-v$ plane, relative weights must be applied to each data set. This weighting plays an important role in the data combination, although the impact of weighting schemes is not straightforward.

For an interferometer, a weighted, sampled visibility function V^W can be defined by

$$V^W(u,v) = \sum_{k=1}^{M} R_k T_k D_k \delta(u-u_k, v-v_k) V'(u_k, v_k). \tag{2.12}$$

where the coefficients R_k, T_k and D_k are weights assigned to the visibility points. R_k is a weight that indicates the reliability of the visibility and T_k (taper) is used to downweight the data at the outer edge of the $u-v$ coverage.

Of particular interest is D_k, the density weighting function used to offset the high concentration of $u-v$ tracks near the center of the plane. When $D_k = 1$ is called natural weighting (treat all points alike) and if $D_k = 1/N_s(k)$ is known as uniform weighting. $N_s(k)$ is the number of data points in a region of the $u-v$ plane.

Natural weighting gives the best signal to noise ratio for detecting weak sources. However this weighting tends to emphasize the data from the shortest baselines, since the inner part of the $u-v$ plane is usually more populated.

In the case of the single dish observations, the pseudo-visibilities derived from the single dish may have a weight estimated according to criteria like the noise of the single dish data, optimal weighting for a given observing time, etc. Finally, the weights of the pseudovisilities can be escalated to the interferometric ones, which implies estimating scaling factors.

2.4 Our work on combination of single-dish and interferometer data

In this thesis, we attempted a combination of single-dish (Goldstone 70m antenna) and interferometer data (VLA) for spectral line emission of the CCS molecule in TMC-1. This is described in section 3.2.3. We have also applied this technique successfully in the past. In particular, we would like to mention the Master thesis of this author presented at the

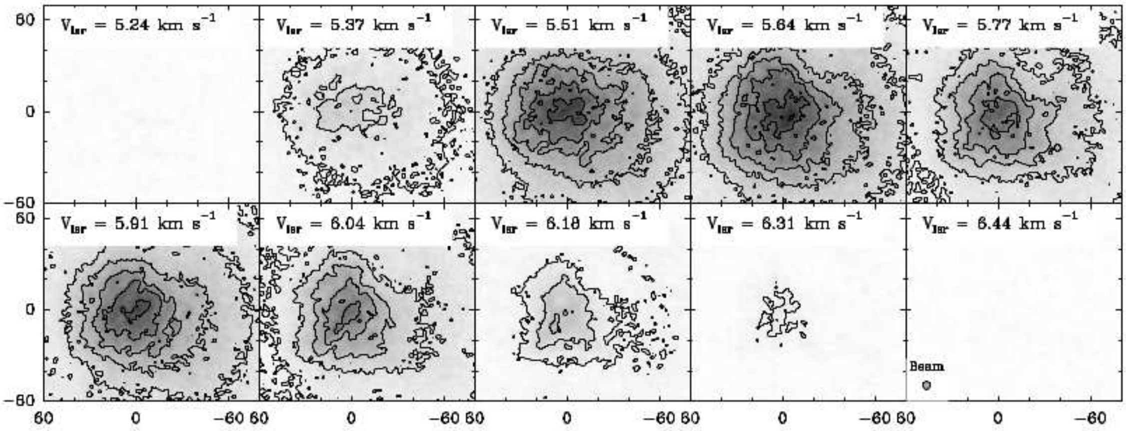

Figure 2.5: Velocity channels of the combined data of the dense core L1517B. Taken from Manjarrez (2008).

Universidad Nacional Autónoma de México (Manjarrez 2008). In that case we combined NH_3 (1,1) data of the region L1517B in the u-v domain (see Fig. 2.5). This combination was carried out with single dish observations we obtained with the 70m antenna at Robledo de Chavela (part of NASA Deep Space Network), and interferometer data with the VLA.

Chapter 3

Dense molecular gas in the pre-stellar region TMC-1

3.1 Introduction

3.1.1 The Taurus-Auriga complex

Taurus-Auriga is a complex of molecular clouds located at a distance of $\simeq$ 140 pc (Kenyon et al. 1994), containing clouds in different evolutive stages, from starless ones to star forming regions. Therefore, it contains the closest sites of current and future active star formation, which allows the study of star formation history at maximum spatial resolution.

The total mass of the complex is estimated to be $\sim 3 \times 10^4 M_\odot$ (Goldsmith et al. 2008; Ungerechts & Thaddeus 1987), distributed over a linear extent of about 30 pc (Ungerechts & Thaddeus 1987). The large-scale structure of the complex shows clouds in the form of filaments composed of smaller clouds ($\sim$ 1 pc), which in their turn contain smaller cores ($\sim$ 0.1 pc). The Taurus-Auriga complex has a low stellar density ($1-10$ stars pc^{-3}, Gómez et al. 1993, Luhman 2000), suggesting that stars are forming in relative isolation. Many low-mass YSOs, from class 0 to T Tauri stars, are found in the complex (Weintraub 1990; Hartmann 2002; Carney et al. 2016).

3.1.2 TMC-1

TMC-1 is a filamentary dark cloud, part of the Taurus-Auriga complex. It is a quiescent dense structure that forms a ridge in the southeast-northwest direction, covering an area of $\simeq 1.2 \times 0.4$ pc (Langer et al. 1995) and with a mass $\simeq 20-30$ M$_\odot$ (Pratap et al. 1997; Langer et al. 1995). TMC-1 does not contain any known YSO, molecular outflow or water masers, indicating that there is no ongoing active star formation in the region. The only exception is IRAS 04381+2540, a class I source (Young et al. 2003) located near the northwest end of TMC-1, but outside the main ridge. This source has a bipolar outflow

(Bontemps et al. 1996; Chandler et al. 1996) and it is probably the only source that may have some influence in the evolution of the TMC-1 ridge (Markwick et al. 2000).

TMC-1 is well known for its chemical richness. Its relative isolation and strong chemical differentiation makes this cloud an ideal laboratory to study the chemistry of dark clouds at the early stages of their evolution. The molecular abundances in the cloud show an interesting pattern. Maps of the emission of some molecules, like cyanopolyynes ($HC_{2n-1}N$ with $n = 1, 2, 3, 4, 5, 6$), C_4H, CCS, and OH peak at the southeastern part of TMC-1 (Little et al. 1979; Churchwell et al. 1978; Harju et al. 2000). On the other hand, molecules like NH_3, SO, HCO^+ and N_2H^+ peak at the northwest of the cloud. These two molecular peaks (hereafter referred to as the "cyanopolyyne peak" and the "ammonia peak") are separated by $\sim 7'$. This trend suggests that the abundance of molecules like cyanopolyynes and NH_3 are anticorrelated (Little et al. 1979; Olano et al. 1988; Pratap et al. 1997).

The substructure of TMC-1 was studied by Hirahara et al. (1992), who identified six dark cores with observations of CCS and NH_3 (shown in Fig. 3.1) and named them from north to south with letters A to E, plus X (the latter associated with IRAS 04381+2540). In the following we will follow this core nomenclature, which is different from that used by other authors. Hirahara et al. (1992) suggested that the observed chemical differentiation reflects a different evolutionary stage in the cores, with those in the southeast being in a relatively earlier stage than the ones in the northwest. This is further supported by the presence of IRAS 04381+2540 in the northwestern region.

Higher-resolution observations of CCS by Peng et al. (1998) showed further microstructure in core D of TMC-1. These authors pointed out that emission originates in three narrow velocity components, centered at 5.7, 5.9, and 6.1 km s^{-1}. These components seem to trace three parallel filaments along the ridge. The filaments are composed by a total of 45 clumps, with masses and sizes between $0.04 - 0.6$ $M_\odot$ and $0.02 - 0.04$ pc. Most of these clumps appear to be gravitationally unbound, and only five (all within the 6.1 km s^{-1} feature) may be unstable to gravitational collapse. This microstructure of unbound clumps suggests that core D is very young, because they should disperse in less than 10^5 years, unless there is a mechanism that confines the clumps. Moreover, Hartquist et al. (2001) did not find any chemical model consistent with a larger age, and they suggested that core D of TMC-1 is extremely young, with an estimated age of 6×10^4 years.

Here we will analyze high resolution observations performed with the VLA on cores B and D of TMC-1, in transitions of CCS and NH_3. Our aim is to study the physical and chemical evolution of a prestellar region with the help of these two molecular tracers at small scales ($\simeq 5''$).

3.2 Observations

3.2.1 Field selection

We chose to study the cores B and D of the cloud TMC-1 (see Fig. 3.1) due to the clear differences of NH_3 and CCS emission found in them. Core D is the strongest source

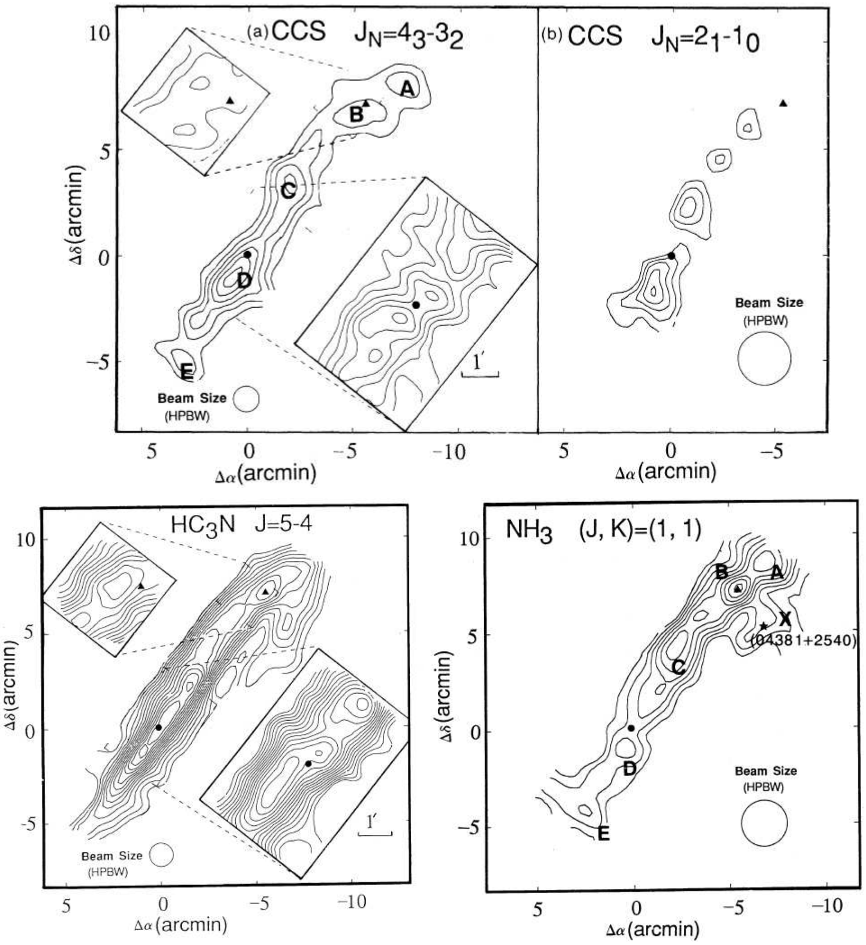

Figure 3.1: Integrated intensity maps of the transitions CCS ($J_N = 2_1 - 1_0$), CCS ($J_N = 4_3 - 3_2$), HC_3N ($J = 5 - 4$), and NH_3 (1,1) observed in TMC-1 by Hirahara et al. (1992). The right ascension and declination axes are shown in offsets with respect to the cyanopolyyne peak. The filled circle and triangle mark the position of the cyanopolyyne and ammonia peaks, respectively. The letters A-E identify the six cores defined by Hirahara et al. (1992). The star marks the position of the source IRAS 04381+2540.

of CCS emission in the survey of Suzuki et al. (1992), and has been proposed as a site of future low-mass star formation (Peng et al. 1998), making it an ideal source to study the CCS emission at early stages of molecular cloud evolution. However, the CCS emission appears to be anticorrelated with that of NH_3 on scales of several arcmin along the TMC-1 ridge (Hirahara et al. 1992). The strongest NH_3 emission is found in core B, (Hirahara et al. 1992) which makes this core an interesting target to compare with cores where CCS is more intense.

In the cases where emission is stronger (NH_3 in core B, and CCS in core D), there is significant extended emission, at scales larger than the primary beam of the VLA at 1 cm (diameter $\simeq 2'$). Its study at these wavelengths requires to observe several fields to produce mosaics. On the other hand, where the emission is weaker −CCS (core B) and NH_3 (core D)− a single field seems to cover it properly.

Taking into account these previous considerations, we planned to observe cores B and D of TMC-1 with the VLA in order to investigate whether the small scale anticorrelation ($\sim 5''$) between CCS and NH_3 observed in B1-IRS (De Gregorio-Monsalvo et al. 2005) extends to starless cores and, among these, in regions with different relative evolutionary stages. To cover the whole extent of the molecular emission observed with single dish, we observed in core D four fields for the CCS transition and one field for the weaker NH_3. For core B, the stronger NH_3 emission was covered by a 3-field mosaic, and the weaker CCS emission by one field. The distribution of these fields is represented in Fig. 3.2. The cyanopolyyne peak is located at R.A. (J2000) = $04^{\rm h}41^{\rm m}42\overset{\rm s}{.}5$, Dec. (J2000) = $25^\circ41'27\overset{''}{.}00$, and the ammonia peak at R.A. (J2000) = $04^{\rm h}41^{\rm m}23\overset{\rm s}{.}0$, Dec. (J2000) = $25^\circ48'13\overset{''}{.}33$ (Hirahara et al. 1992).

3.2.2 Technical setup and data reduction of interferometric data

We carried out observations of the NH_3 (1,1) and CCS $J_N = 2_1 - 1_0$ transitions (rest frequencies 23694.495 and 22344.033 MHz respectively) towards cores B and D of TMC-1 in 2005, using the Karl G. Jansky Very Large Array (VLA) of the National Radio astronomy Observatory in its D configuration (project AC793). The field identification, phase center, transitions and synthesized beam sizes of the observations are listed in Table 3.1. The CCS transition was observed in the 2AD mode obtaining both right and left circular polarizations, with a bandwidth of 0.78 MHz (centered at $V_{\rm lsr}$ = 5.7 km s^{-1}), sampled over 255 channels that provide a spectral resolution of 3.051 kHz (0.038 km s^{-1}). The NH_3 (1,1) transition was observed in the 1A spectral line mode that provided only one circular polarization (right), but a broad enough bandwidth to cover the inner satellite lines of NH_3. The bandwidth was 1.56 MHz centered at $V_{\rm lsr}$ = 5.7 km s^{-1}, sampled over 511 channels that yield a spectral resolution of 3.051 kHz (0.038 km s^{-1}).

We used the source J0137+331 (3C48) as the primary flux calibrator, with adopted flux densities of 1.12 Jy and 1.05 Jy at 22.3 and 23.7 GHz, respectively, using the 1999.2 VLA coefficients (Perley & Taylor 2003). Our phase calibrator was J0431+206, with bootstrapped flux density values of 0.68 Jy and 0.63 Jy, respectively. The source J0319+415 (3C84) was used as a bandpass calibrator. Data reduction was performed using the Astro-

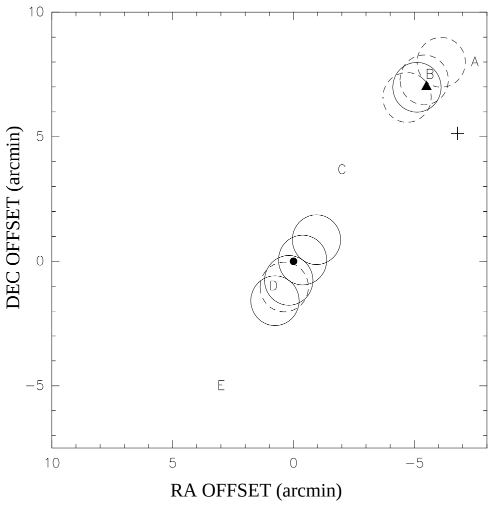

Figure 3.2: Distribution of the fields in our VLA observations of TMC-1. Coordinates are relative offsets with respect to the cyanopolyynes peak. Circles indicate the primary beam area (diameter $\simeq 2'$) at 1.3 cm. The solid and dashed circles correspond to the fields observed in CCS and NH_3 (1,1) respectively. Letters A−E indicate the peak position of the cores identified by Hirahara et al. (1992). The position of the cyanopolyyne peak is indicated by a filled circle and the NH_3 peak with the filled triangle. The cross indicates the position of the infrared source IRAS 04381+2540.

Field ID	R.A. (J2000)	Dec. (J2000)	Transition	$\theta_{\rm fwhm}{}^1$ (arcsec)	$\theta_{\rm pa}{}^2$ (degrees)
Core B					
B1	04 41 21.761	25 48 03.00	NH_3(1,1)	3.5×3.2	58.3
B2	04 41 18.635	25 48 45.62	NH_3(1,1)	3.5×3.2	58.8
B3	04 41 15.508	25 49 28.23	NH_3(1,1)	3.5×3.2	58.3
B4	04 41 19.949	25 48 27.73	CCS $J_N = 2_1 - 1_0$	3.7×3.3	−54.4
Core D					
D1	04 41 45.857	25 39 51.75	CCS $J_N = 2_1 - 1_0$	3.6×3.4	−84.5
D2	04 41 43.333	25 40 40.92	CCS $J_N = 2_1 - 1_0$	3.7×3.3	−54.6
D3	04 41 40.809	25 41 30.09	CCS $J_N = 2_1 - 1_0$	3.6×3.4	−85.7
D4	04 41 38.286	25 42 19.27	CCS $J_N = 2_1 - 1_0$	3.6×3.3	−51.6
D5	04 41 44.168	25 40 24.86	NH_3(1,1)	3.5×3.2	57.3

[1]:Full width at half maximum of the synthesized beam.

[2]:Position angle (north to east) of the synthesized beam.

Table 3.1: Fields observed in TMC-1 cores B and D with the VLA. The CCS observations were performed on 2005 November 18, and the NH_3 (1,1) observations on 2005 November 13, 15, 20 and December 05.

nomical Image Processing System (AIPS) of the NRAO using the recommended procedures for high-frequency data processing.

We made maps of the two transitions using a weighting of visibilities with robust parameter 5 (equivalent to natural weighting) and convolved the resulting images with a $10''$ beam to improve the signal to noise ratio for extended emission. Mosaics were built using task 'FLATN'. Fits to NH_3 spectra (section 3.4) were carried out with the Continuum and Line Analysis Single-dish Software (CLASS) of the Instituto de Radioastronomía Milimétrica (IRAM).

3.2.3 Combination of interferometer and single-dish data

As we will discuss below, the VLA misses a large fraction of the CCS emission in this source. Thus, we tried to combine the interferometric data with single-dish observations in the region. For this, we used the CCS spectra obtained by Peng et al. (1998) with NASA's Goldstone 70m antenna, kindly provided by these authors.

For this combination, we followed the method described in Section 2.3.1, and that we applied in Manjarrez (2008). We applied different relative data weightings to the interferometer and single-dish data. This was a challenging endeavor, since it implied using both the combination and mosaicing technique explained in Chapter 2. However, despite our efforts, no useful results were obtained in this case. The only meaningful maps showed structures that were nearly identical to the already published single-dish maps. Our interpretation is that the interferometer missed too much flux ($\simeq 90\%$, Section 3.3.2), and the resulting emission that it did sample had a very low signal-to-noise ratio (section 3.3), in comparison with the single-dish emission. Therefore, the interferometric data could not give any additional information over the maps obtained with the Goldstone antenna, and the combined data set is largely dominated by the latter. That the VLA observations missed virtually all the CCS emission has some implications on the spatial scale of the emission that will be discussed in Section 3.4. Therefore, in the remaining of this chapter, we only present the results of our VLA observations, applying the mosaicing technique.

3.3 Results

3.3.1 Core B

The spectra of the NH_3 (1,1) and CCS transitions at the peak of each field of core B are shown in Fig. 3.3. The NH_3 (1,1) main component of the electric quadrupole hyperfine structure of the transition is located around $V_{LSR} = 6.0$ km s^{-1} with the inner satellite components near the band edges. The outer satellite lines are outside the observed bandwidth. In their turn, these lines appear to consist of more than one component, which represent the magnetic hyperfine structure of the NH_3 (1,1) transition (Ho & Townes 1983). As in other "quiescent" clouds (Rydbeck et al. 1977; Benson & Myers 1989;

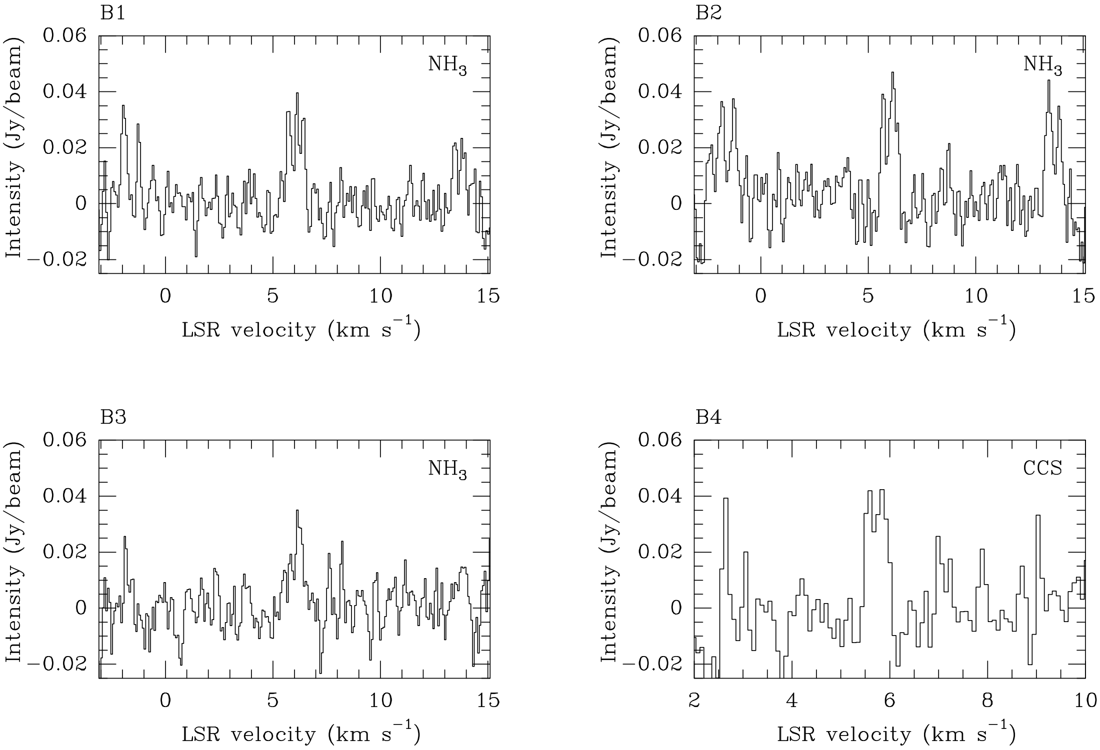

Figure 3.3: Spectra of the NH$_3$ (1,1) transition for fields B1, B2 and B3 and CCS transition (field B4) averaged over an area of about 10″ around the peak emission of each field.

Manjarrez 2008; Seo et al. 2015) the magnetic hyperfine structure can be resolved since the corresponding lines are narrow, due to the low temperature and turbulence in these regions. In sites of active star formation, the lines are wider, and the magnetic hyperfine components blend together, with the result that only the electric quadrupole hyperfine structure of NH$_3$ (with one main line and four satellite lines) can be distinguished.

The physical parameters of the spectra are shown in Table 3.2. The NH$_3$ parameters were obtained by adjusting the complete hyperfine structure of the transition with the method NH$_3$(1,1) of the CLASS software. The velocity of the lines are in agreement with the values found by other authors (Toelle et al. 1981; Olano et al. 1988), who found velocities around 6.1 km s^{-1} for the north-western area of TMC-1 with single dish NH$_3$ observations. The slightly redshifted velocity (shifted by $\sim$ 0.1 km s^{-1}) of the northern field B3 appears to be consistent the velocity gradient suggested by Toelle et al. (1981).

On the other hand, the CCS emission of core B4 is centered at 5.74 km s^{-1}, consistent with the CCS $J_N = 4_3 - 3_2$ single dish observations of Hirahara et al. (1992). Our spectrum consists of two components, located at 5.83 and 5.57 km s^{-1}.

The NH$_3$ integrated intensity maps (without correction of primary beam) of the fields observed in core B (B1, B2 and B3) are shown in Fig. 3.4. The NH$_3$ emission shows structures aligned in southeast-northwest direction in all fields. The presence of insufficiently

Table 3.2: Parameters of the NH_3 and CCS spectra at the peak of each field of core B.

Core B				
Field	Transition	V_{LSR}	Δv	τ main
		(km s^{-1})	(km s^{-1})	
B1	NH_3	5.97 ± 0.01	0.20 ± 0.02	13.3 ± 1.2
B2	NH_3	5.97 ± 0.01	0.25 ± 0.02	14.2 ± 1.0
B3	NH_3	6.06 ± 0.06	0.43 ± 0.13	2.5 ± 2.2
B4 a	CCS	5.83 ± 0.03	0.25 ± 0.08	
B4 b	CCS	5.57 ± 0.03	0.15 ± 0.07	

Table 3.3: Physical parameters of fields B1, B2 and B3 (NH_3) and B4 (CCS).

		Core B		
Field ID	Transition	N^1_{mol}	$N^2_{H_2}$	M^3
		(10^{13} cm^{-2})	($10^{23}cm^{-2}$)	($M_\odot$)
B1	NH_3	135	1.35	0.5
B2	NH_3	190	1.9	1.0
B3	NH_3	60	0.6	0.1
B4	CCS	1.5	1.6	0.2

1. Column density of NH_3 and CCS derived following the assumptions and formulas indicated in the appendix.

2. Hydrogen column density, obtained assuming a fractional abundance with respect to H_2 of 0.9×10^{-10} for CCS (Lai & Crutcher 2000) and 1×10^{-8} for NH_3 (Herbst & Klemperer 1973).

3. Mass of the structure with the peak emission of each field. We assumed $T_{ex} = 8$ K for NH_3 and $T_{ex} = 5$ K for CCS (Suzuki et al. 1992).

sampled extended emission is evident by the presence of areas with negative intensities (shown only in the greyscale of Fig. 3.4 for clarity). A mosaic of the fields (Fig. 3.5) shows that NH_3 emission is distributed as a filament in SE-NW direction, that extends over the whole mapped region. Contours trace the presence of several local maxima along the filament, where the integrated intensity shows a trend to increase towards the southeast of the filament. The NH_3 peak position of TMC-1 (Hirahara et al. 1992) is close ($\sim 25''$) to the peak of our field B1 located at R.A. (J2000) = $04^h41^m22\overset{s}{.}80$, Dec. (J2000) = $25°47'49\overset{''}{.}0$. The physical parameters of NH_3 and CCS derived from the region are shown in Table 3.3.

The first-order moment of the mosaic (velocity field, Fig. 3.6 left) does not show a clear velocity gradient along the ridge. However, we see that the most redshifted velocities of the mosaic are located in fields B2 and B3, which also exhibit local velocity gradients nearly perpendicular to the ridge, as found by Olano et al. (1988).

In our second order moment (velocity dispersion) map (Fig. 3.6, right), we see the

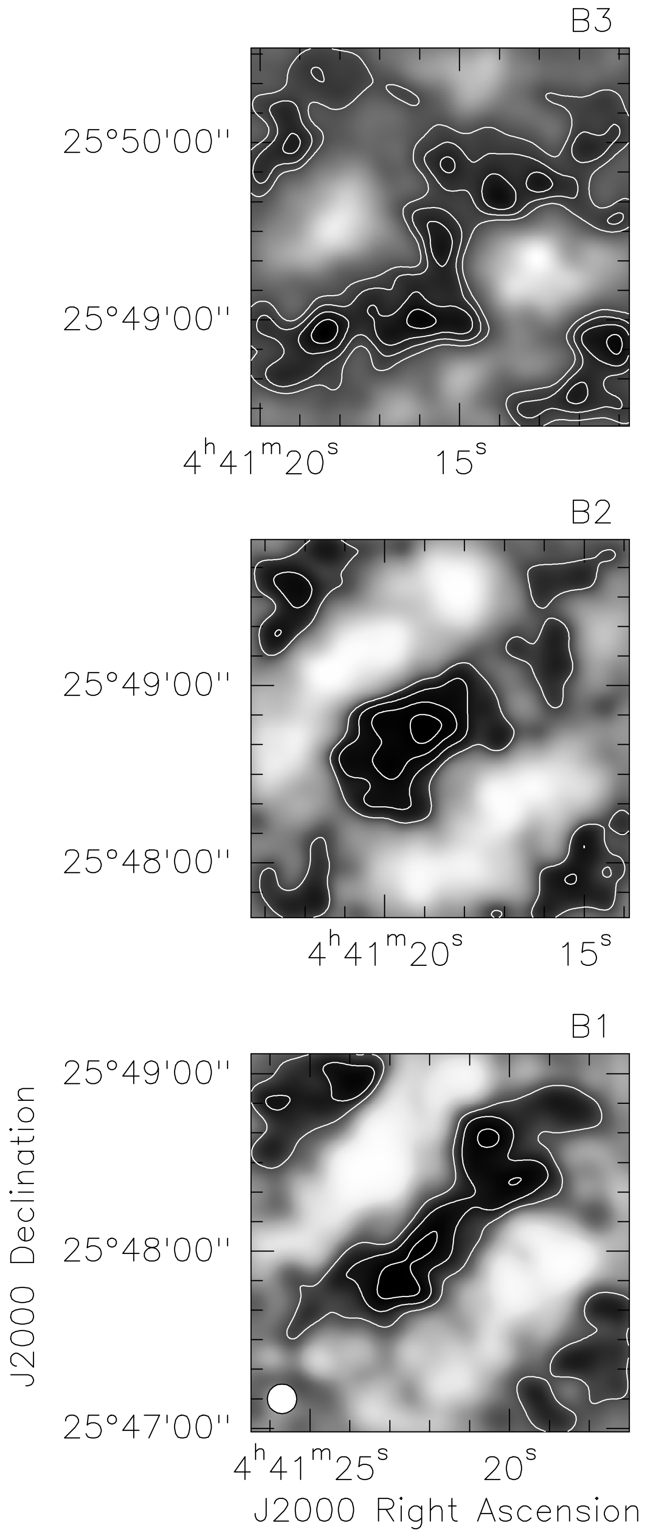

Figure 3.4: Overlay of the integrated intensity maps of the NH_3 (1,1) transition of the fields TMC-1 B1, B2 and B3, showed in color scale (black and white) and contours. The range of integration is from $5.5 - 6.5$ km s^{-1}. Contours are 3, 6, 9 and 12 times the r.m.s of each map (2.4, 2.2 and 2.1 mJy $beam^{-1}$ km s^{-1} for B1, B2 and B3 respectively). The color scale shows emission in black and negative values in white. The beam size is $10''$, shown at the bottom left corner of the B1 map.

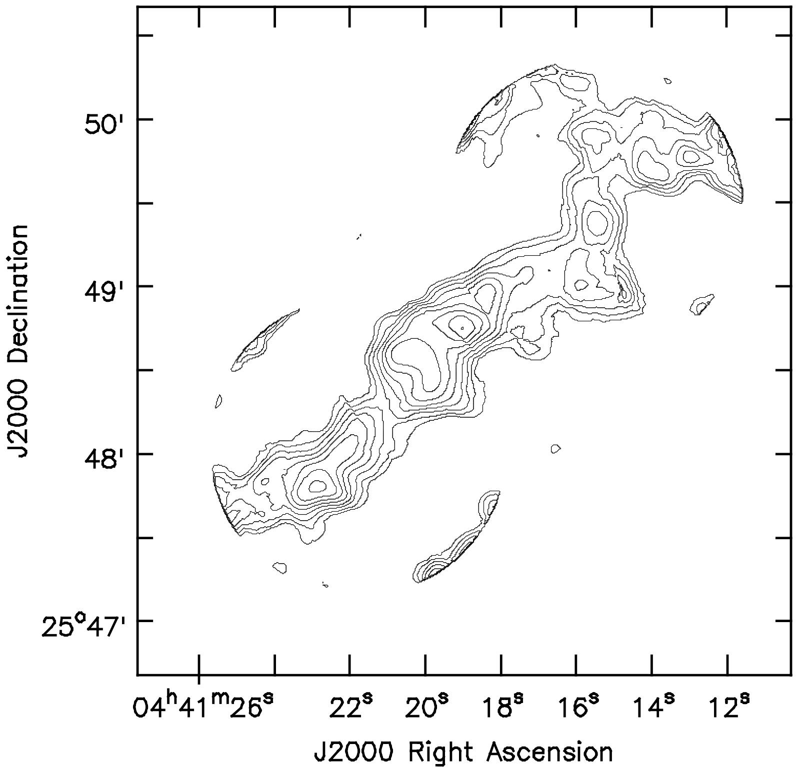

Figure 3.5: Mosaic of the NH_3 (1,1) zeroth-order moment maps of the core TMC-1 B. First contour is 20%, and contour step is 10% of the peak of the map (31 mJy beam^{-1} km s^{-1}). Range of integration is from 5.5 to 6.5 km s^{-1}.

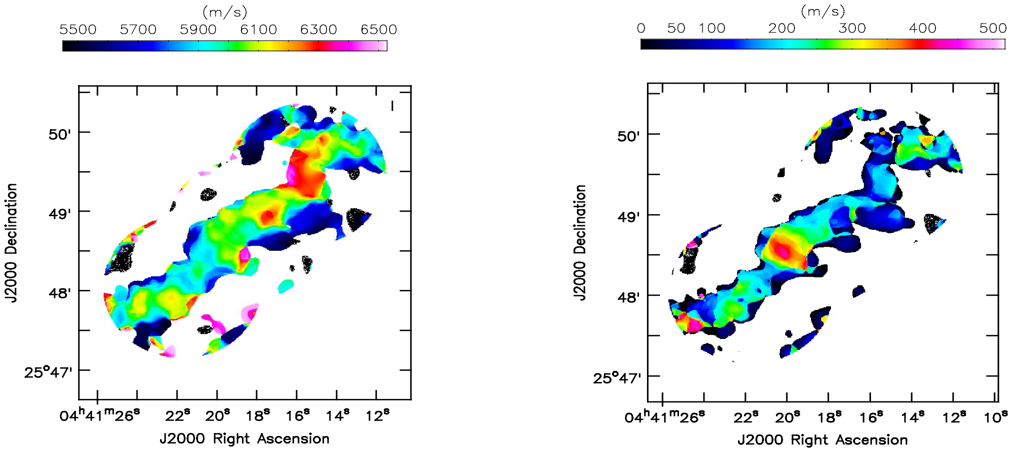

Figure 3.6: Moments 1 (left) and 2 (right) of the NH_3 mosaic of core B.

highest values of the velocity dispersion ($\simeq$ 430 m s^{-1}) are located in a region elongated along P.A.$\simeq$ 55° and peaking at R.A. (J2000)= $04^{\mathrm{h}}41^{\mathrm{m}}20\overset{\mathrm{s}}{.}06$, Dec. (J2000)= $25^\circ48'32\overset{''}{.}5$. The spectrum at that position (Fig. 3.7) shows two components, which explain the highest velocity dispersion, rather than being due to an intrinsically larger linewidth.

An overlay of our NH_3 mosaic and the single field of CCS (B4) observed in this region is shown in Fig. 3.8. The CCS emission seen in the map shows only some small and weak structures in the field, the strongest of them located at R.A. (J2000) = $04^{\mathrm{h}}41^{\mathrm{m}}22\overset{\mathrm{s}}{.}61$, Dec (J2000) = $25^\circ48'56\overset{''}{.}72$, about 30 – 40$''$ NE of the NH_3 filament axis. The weak CCS emission in the B4 field suggests that the CCS and NH_3 are spatially anticorrelated at the sampled angular scale ($\geq 3.5''$).

3.3.2 Core D

The spectra of CCS (fields D1 to D4) and ammonia (D5) are shown in Fig. 3.9 and 3.10 respectively. The CCS spectra consists of a main line, located at velocities close to 6 km s^{-1}, and appears to have more than one component in cores D1 and D3. The parameters obtained from the gaussian fittings of the CCS and ammonia spectra are given in Table 3.4.

Our integrated intensity maps of the CCS transition of core D (without primary beam correction) show that the CCS emission is weak, clumpy and extended over a large area (see Fig. 3.11). We estimate a flux loss of 90% in our interferometric map when compared to the single dish observations of Langer et al. (1995) and Peng et al. (1998). A mosaic of the four CCS fields is shown in Fig. 3.12. In this image we see 5 clumps of CCS along the axis of mosaic. We consider that these structures located along the axis of the mosaic are real, while the contours near the edges of each field could be artifacts due to the primary

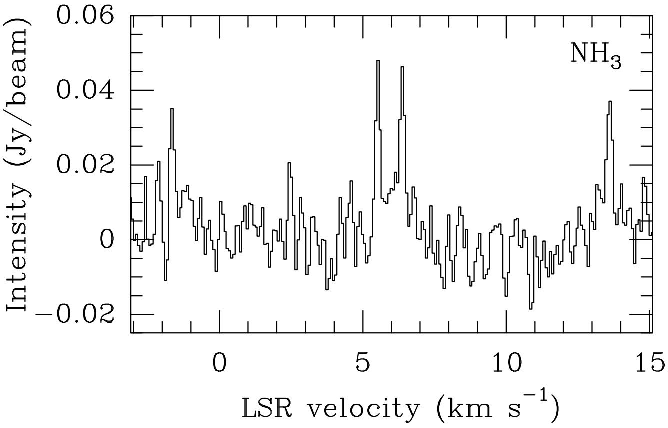

Figure 3.7: Spectrum at the position of the highest value of velocity dispersion.

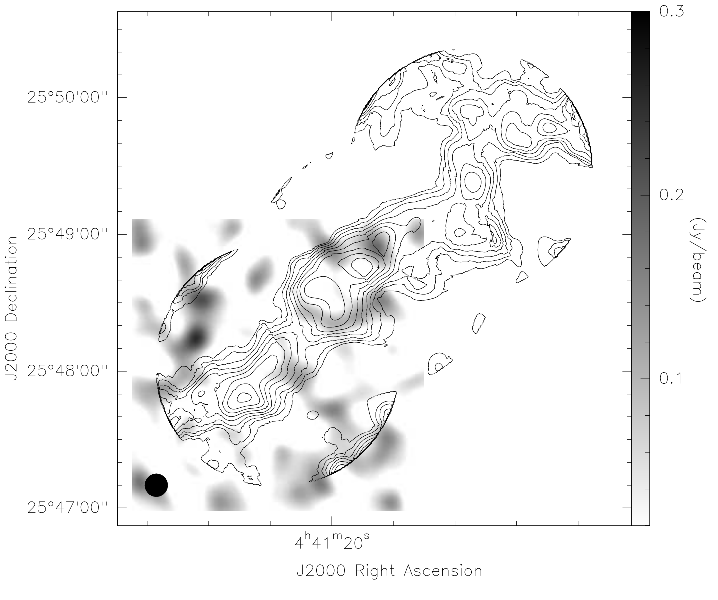

Figure 3.8: Overlay of our NH_3 (1,1) mosaic (contours) and CCS $J_N = 2_1 - 1_0$ map (greyscale) of TMC1 B. The greyscale is shown at the right side of the map.

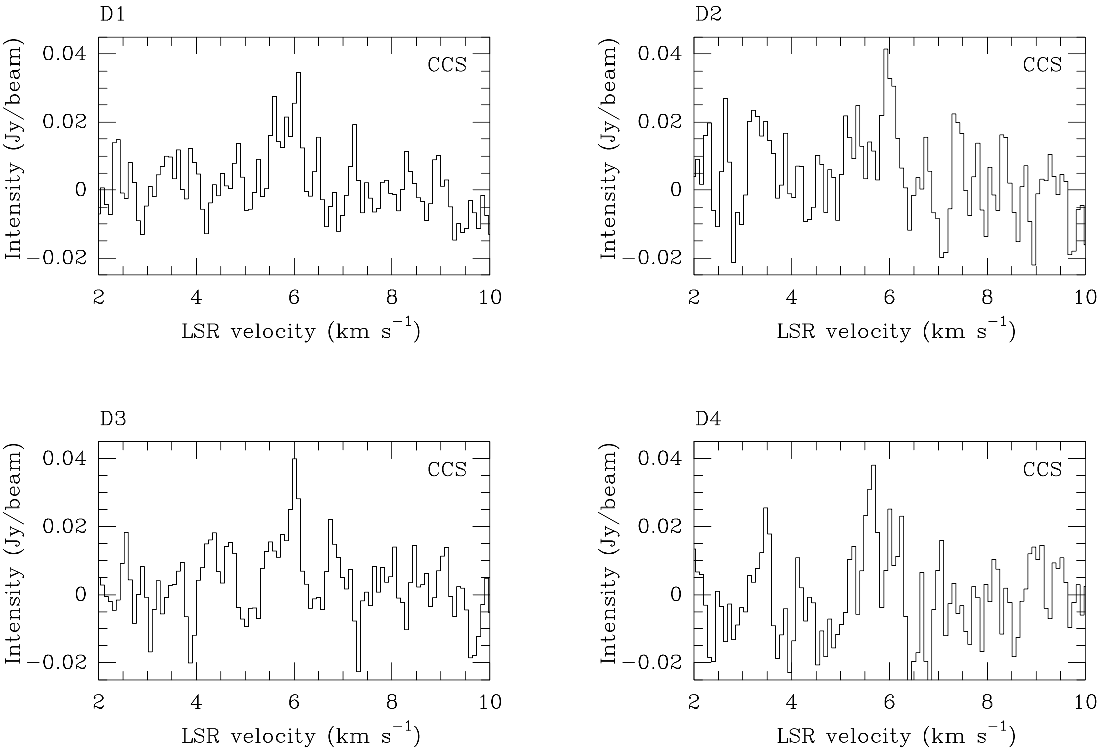

Figure 3.9: Spectra of the CCS $J_N = 2_1 - 1_0$ transition at the peak of fields D1 to D4.

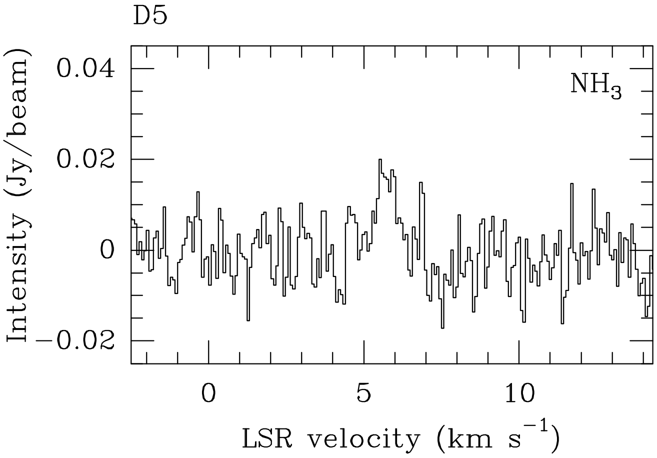

Figure 3.10: Spectrum of the NH$_3$ (1,1) transition at the peak of the field D5.

Core D				
Component	Transition	I_ν	$V_{\rm lsr}$	Δv
		(mJy beam^{-1})	(km s^{-1})	(km s^{-1})
D1 a	CCS	38.9 ± 7.0	6.07 ± 0.02	0.16 ± 0.04
D1 b	CCS	20.3 ± 6.6	5.90 ± 0.04	0.18 ± 0.01
D1 c	CCS	28.4 ± 6.6	5.60 ± 0.02	0.16 ± 0.05
D2	CCS	36.2 ± 6.8	5.98 ± 0.03	0.35 ± 0.07
D3 a	CCS	38.3 ± 9.0	6.01 ± 0.02	0.20 ± 0.06
D3 b	CCS	16.7 ± 5.5	5.63 ± 0.09	0.41 ± 0.25
D4	CCS	36.9 ± 13	5.63 ± 0.04	0.24 ± 0.10
D5 a	NH_3	17.6 ± 4.1	5.58 ± 0.10	0.41 ± 0.21
D5 b	NH_3	13.4 ± 6.8	5.97 ± 0.10	0.29 ± 0.19

Table 3.4: Parameters of the spectra of fields D1, D2, D3 and D4 (CCS) and D5 (NH_3). Lower case letters indicate the component of a line when more than a single gaussian was fitted.

beam correction, which generates non uniform noise, with it being higher at the edges. This image allows us to identify three regions with significant emission. The first one is located at the southern field of the mosaic (identified as clump 1), corresponding to the central structure of field D1 (Fig. 3.11). The second (formed by clumps 2 and 3) is an east-west arc-like structure located between fields D2 and D3, with the local peak close ($\sim 15''$) to the cyanopolyyne peak (Hirahara et al. 1992). The third region is located at the northernmost field and shows mainly two clumps (4 and 5) close to each other ($\sim 19''$ distance between peaks). The derived physical parameters of the main structures located on the axis of the TMC-1 mosaic are shown on table 3.5.

An overlay of the CCS mosaic map and the single field of NH_3 map is shown on Fig. 3.12. It shows that the NH_3 emission is weak in core D, with a peak at R.A. (J2000) = $04^{\rm h}41^{\rm m}47\overset{\rm s}{.}1$, Dec. (J2000) = $25^\circ40'16\overset{''}{.}86$ separated by $\sim 35''$ from the CCS peak of the D1 field (the closest CCS structure).

3.4 Discussion

Our observations show several significant facts that are relevant to understand the evolutionary status of TMC-1.

- The emission of NH_3 and CCS is anticorrelated, at several scales: from a clear chemical differentiation between cores B and D (ammonia being stronger in core B and vice versa) to anticorrelation down to scales of $\simeq 4''$ within each core.
- The CCS maps do not show much emission in either core, despite the rich structure

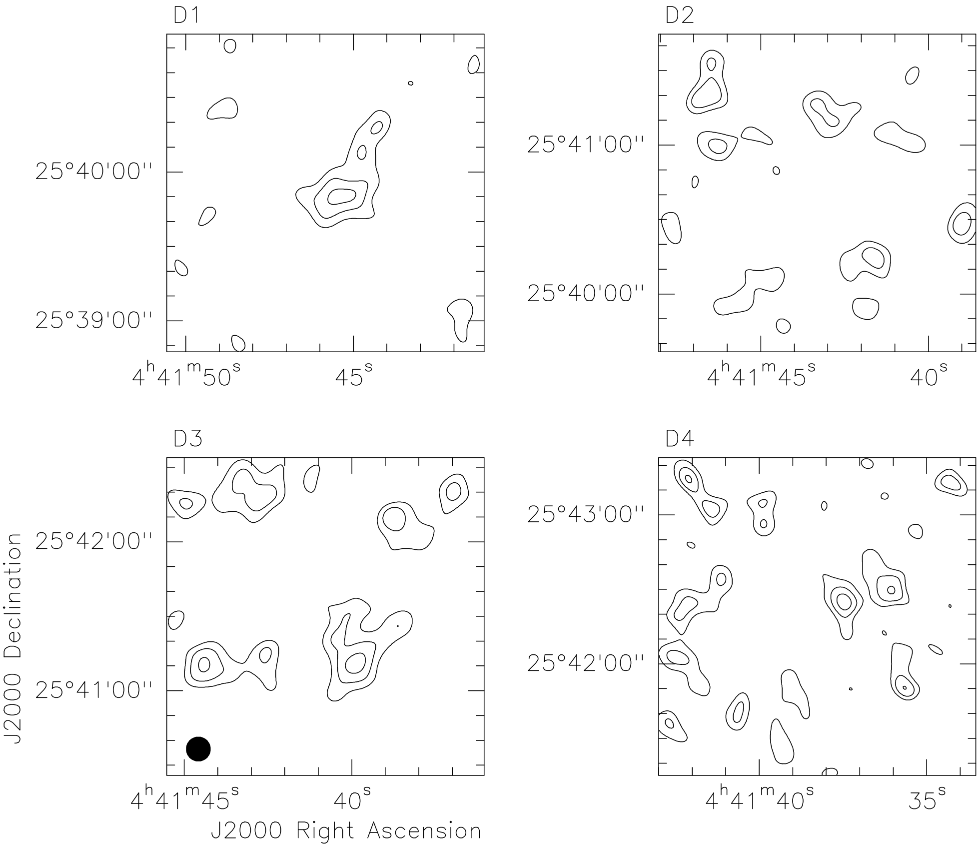

Figure 3.11: Integrated intensity maps of the CCS $J_N = 2_1 - 1_0$ transition in the fields of core D of TMC-1. Contours are 3, 5 and 7 times the r.m.s. of each map (2.1, 2.6, 2.0 and 2.0 mJy beam^{-1} km s^{-1} for D1, D2, D3 and D4 respectively). The velocity of integration is $5.5 - 6.3$ km s^{-1} for D1 and $5.5 - 6.2$ km s^{-1} for D2, D3 and D4. The beam size is $10''$, shown at the bottom left corner of D3 map.

Core D clumps				
Clump ID	Transition	N^1_{mol} (10^{13} cm^{-2})	$N^2_{\mathrm{H_2}}$ (10^{23}cm^{-2})	M^3 ($M_\odot$)
1	CCS	1.1	1.3	0.38
2	CCS	1.0	1.1	0.19
3	CCS	1.3	1.5	0.51
4	CCS	1.5	1.6	0.21
5	CCS	1.3	1.4	0.14
D5	NH_3	5.0	0.05	0.10

1. Column density of CCS or NH_3 derived as explained in the appendix. We assumed that the emission is optically thin.
2. Hydrogen column density, obtained assuming a fractional abundance with respect to H_2 of 0.9×10^{-10} for CCS (Lai & Crutcher 2000) and 1×10^{-8} for NH_3 (Herbst & Klemperer 1973).
3. Mass of the main structures along the axis. We assumed $T_{\mathrm{ex}} = 8$ K for NH_3 and $T_{\mathrm{ex}} = 5$ K for CCS.

Table 3.5: Physical parameters of the main structures along the axis of the mosaic of TMC-1 (CCS) and field D5 (NH_3).

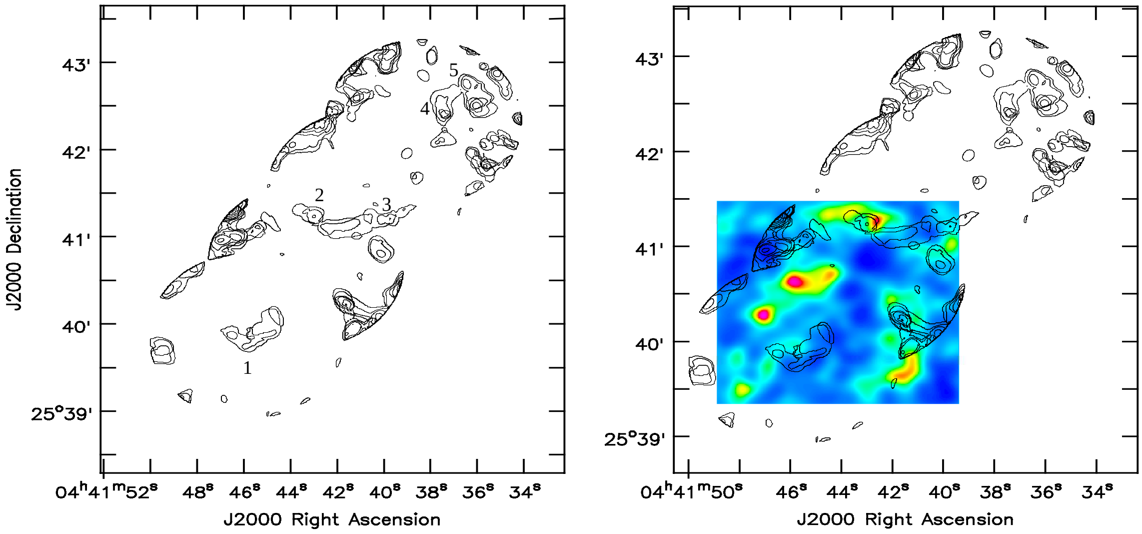

Figure 3.12: . Mosaic of CCS fields of core D (left) and overlay of the mosaic with the NH_3 field of core D (right). First contour and contour level are 10% of the peak (32.7 mJy beam^{-1} km s^{-1}).

of clumps observed in core D with single-dish telescopes. In fact most of the emission is missed by the interferometer, which may impose a lower limit to the typical size of the clumps.

It is generally accepted that the spatial anticorrelation between carbon-chains molecules and ammonia in the TMC-1 ridge indicates a large-scale chemical differentiation between the south-east and north-west regions of the cloud. To evolve to its current state, it is supposed that the cloud was initially in a diffuse state (Howe et al. 1996; Hirahara et al. 1992), a necessary condition to have a high abundance of carbon, in its turn needed to form carbon-chain molecules. At a later stage, the cloud should have had a sudden collapse, which caused its present chemical structure (Howe et al. 1996). According to chemical models, the different large-scale distribution of NH_3 and CCS indicates that core B appears to be more evolved than core D, which is consistent with the observations of several other molecular transitions (Suzuki et al. 1992; Hirahara et al. 1992; Howe et al. 1996; Pratap et al. 1997; Hartquist et al. 2001; Harju et al. 2000).

The anticorrelation between NH_3 and CCS is also seen at small scales ($\simeq 4''$) in our maps (Figs. 3.8 and 3.12). This has been seen in star-forming regions (B1-IRS, De Gregorio-Monsalvo et al. 2005), but it is also relevant that this small-scale anticorrelation stands in a starless cloud. In general, small scale anticorrelation in more evolved regions is characterized by ring-like structures traced by CCS, surrounding the dense core traced by NH_3 (e.g., L1498 or B335, Tafalla et al. 2006, Kuiper et al. 1996, Velusamy et al. 1995). This is an evolutionary effect, where CCS abundance decreases at the center of those sources, due to molecular depletion in the denser regions, leaving a surrounding CCS shell. However, neither our maps (Fig. 3.11 and 3.12) nor the ones in Hirahara et al. (1992) and Peng et al. (1998) show these characteristic ring-like structures. Only the ark-like structure located between our fields D2 and D3 is suggestive of a ring, but it is not clearly defined, and it may be the projected superposition of two or more clumps. We suggest that the detection of CCS emission but without the ring-like structures expected in relatively evolved star-forming regions further support the youth of core D.

The Taurus molecular cloud shows large scale filamentary structure (Panopoulou et al. 2014). At smaller scales ($\simeq 70''$) Hirahara et al. (1992) found that TMC-1 was a fragmented filamentary structure composed of aligned cores. More recently, the velocity structure of the region seen with several molecular tracers like NH_3 (Fehér et al. 2016), ^{13}CO (Panopoulou et al. 2014), HC_7N (Dickens et al. 2001) and CCS (Peng et al. 1998) also suggested that the TMC-1 filament could be composed by filamentary substructures observed at different velocities. Our CCS observations missed most of the structure observed with single-dish, although our NH_3 maps of core D do reflect a clumpy filamentary structure. The typical distance between structures, either clumps in single-dish CCS maps (Peng et al. (1998) or our NH_3 images (Fig. 3.5) is < 0.1 pc ($\simeq 0.08$ pc in our NH_3 maps). It is expected that filaments may form smaller structures like clumps and cores due to gravitational instabilities (Contreras et al. 2016; André et al. 2010). Models suggest that the structures derived from such fragmentation should be separated by a characteristic spacing, which depends on the wavelength of the fastest growing unstable mode (Contreras et al. 2016). This is referred to as “the sausage instability”. For this model, in the most simple case, the preferred spacing is given by $\lambda_{s,0} = 21.8 H_{\mathrm{eff},0}$, where $H_{\mathrm{eff},0} = \sigma(4\pi G\rho_c)^{-1/2}$ (Contreras et al. 2016). In this expression, σ is the the velocity dispersion of the gas in the filament and ρ_c is the central density of the filament, and G is the gravitational constant.

Considering average physical parameters of clumps in TMC-1 ($M \simeq 0.25$ M$_\odot$, $\Delta v \simeq 0.25$ km s^{-1}, radius$\simeq 0.015$ pc), assuming constant density, we found that the preferred spacing between clumps is ~ 0.1 pc, which is similar with the observed one. This spacing is similar to the median spacing (~ 0.08 pc) between prestellar cores observed in Aquila (André et al. 2014). This suggests that the formation of clumps in filaments can be a natural evolutionary process. As noted by André et al. (2014), the spacing is similar to the characteristic inner width (~ 0.1 pc) of filaments in molecular clouds.

Although the formation of clumps in filaments may be a natural process, clumps will dissipate with time. The clumpy structure of TMC-1 implies that either they are still too young to have dissipated or some additional mechanism confines the clumps. If not confined by external pressure, unbound clumps will disperse over a time scale of $\sim 2 \times 10^5$ years (Peng et al. 1998). With a interclump density of 2×10^3 cm^{-3}, this gas would need a high temperature ($\simeq 40$ K) to confine the CCS clumps (Peng et al. 1998). But that temperature is at least twice the value found from C^{18}O observations (Langer et al. 1995; Peng et al. 1998). This may imply that both thermal and turbulent pressure of the interclump gas is needed to confine the clumps, where turbulent pressure should be equivalent to the thermal pressure of a gas at a temperature of $75 - 100$ K (Peng et al. 1998).

It is obvious that there is significant extended molecular-line emission in TMC-1, as suggested by the negative contours around the detected clumps. In fact, we estimate that $\sim 90\%$ of the CCS emission seen with single dish (Peng et al. 1998) is lost in our interferometric observations. The largest angular scale visible to the VLA in the D configuration at 1.3 cm is $\sim 60''$. At a distance of 140 pc (Kenyon et al. 1994), this scale correspond to about 8400 AU (~ 0.04 pc). Typical CCS clumps have sizes between $0.02 - 0.04$ pc ($30'' - 60''$ at 140 pc, Peng et al. 1998), so we may be losing significant structure of them. On the other hand, our NH$_3$ mosaic of core B appears to be missing emission mainly perpendicularly to the filament, but not along it.

Given that our CCS and NH$_3$ observations have a similar set up, this difference is relevant. The lack of emission between clumps of our CCS mosaic may indicate a decrease of CCS abundance in the interclump medium. It may also suggest that the excitation conditions are insufficient to detect the CCS emission in our observations (for instance, that the density is below the critical density of the transition), or that this emission does not show much variation over scales < 0.04 pc and is thus missed by the interferometer. With our data, it is not possible to distinguish between these two alternatives (or a combination of the two). Given that the gas has a density of $\simeq 2 \times 10^3$ cm^{-3} as seen in C^{18}O (Langer et al. 1995; Peng et al. 1998) we consider that, in core D, the material between clumps might be composed of gas of significantly lower density, below the CCS critical density ($\sim 3 \times 10^4$ cm^{-3}, Kuiper et al. 1996). On the other hand material between cores is detected in our NH$_3$ maps of core B, as seen seen in Fig. 3.5. This implies that NH$_3$

is also formed between cores and that the excitation conditions for the detection of this emission are met.

As mentioned above, compared to the rest of cores in TMC-1, core B is generally considered to be in a more evolved stage of evolution. Our maps of this core showed strong emission of NH_3 tracing a large and narrow filament containing small cores, but with the negative contours at the sides indicative of extended emission. The width of filament varies along the map, between $0.02 - 0.04$ pc ($\sim 30'' - 60''$) as measured directly in the mosaic of integrated intensity. As the typical width of a filament is estimated to be $\sim$ 0.1 pc (André et al. 2014; Malinen et al. 2012), it seems that our ammonia map is tracing a fraction of the actual width of TMC-1B in NH_3, and wider structures are missed by the interferometer.

The NH_3 (1,1) first order moment of the mosaic confirmed the presence velocity gradients perpendicular to the axis, with redshifted velocities to the south-west and blue-shifted to the north-east. Moreover, the map does not show any clear trend along the ridge. These results are in agreement with the results of other works of TMC-1 (Fehér et al. 2016; Panopoulou et al. 2014; Olano et al. 1988) who also found similar kinematical trends. Filamentary structures in other regions show velocity gradients either along their length and across their axis (Uchida et al. 1990; Dobashi et al. 1992), which may suggest activity like flow of material along the filament or contraction (Kirk et al. 2013). Transversal velocity gradients like the ones we detect may also be a sign of filament formation within sheet-like structures (Fernández-López et al. 2014; Beuther et al. 2015).

On the other hand, the second order moment of NH_3 showed a region with the peak velocity dispersion located between our field B1 and B2 of the NH_3 mosaic, that could, in principle, be a zone of future star formation. However, the spectrum taken at that position shows two components with the highest separation in velocity, which may suggest the presence of two structures or filaments with different velocity in that region.

In summary, the evolution of the ridge in TMC-1 seems to have started in core B. The perturbation created by this core may have expanded towards the south-east of the core in a natural way. Some authors have suggested that TMC-1 experienced a physical and chemical evolution trough processes like magnetohydrodynamical waves (Markwick et al. 2000; Hartquist et al. 2001; Dickens et al. 2001) or the shock of an interstellar wind (Hartquist et al. 1996). It is expected that future star formation will start in some of the clumps of core B.

3.5 Conclusions

In this chapter we present mosaic images of the CCS and NH_3 emission toward the starless region TMC-1 We can summarize our main results as follows:

- We found the CCS and NH_3 emission is spatially anticorrelated in the cores B and D of TMC-1. At the scale of cores, NH_3 emission is stronger in core B while CCS emission is stronger in core D. At smaller scales ($\simeq 4''$), we found this anticorrelation within each core.

- In this filamentary dark cloud without ongoing active star formation, the chemical differentiation of cores B and D seems to be in agreement with the evolutive scheme of Suzuki et al. (1992). In this scheme, TMC-1 present the expected chemical evolution of a dark cloud in an early stage of evolution.
- In core D, we found CCS emission distributed in the form of clumps, without the ring-like structure observed in more evolved regions, which suggest that core D could be very young.
- Our NH_3 maps of core B show several cores tracing a filamentary structure. The typical spacing between cores (~ 0.1 pc) in both CCS (from single-dish observations) and our NH_3 images of TMC-1 is consistent with the spacing expected from a model of structure formation from fragmentation of a filament.
- The NH_3 velocity gradients perpendicular to the TMC-1 ridge may suggest activity like contraction or flow of material along core B. Alternatively, it could be a sign if filament formation within sheet-like structures.
- Our results suggest that the evolution of TMC-1 began in core B, which may be the future site hosting the first stars along the ridge.

Chapter 4

Chemistry and infalling motions in the GF9-2 low-mass star-forming region

4.1 Introduction

As previously discussed in Chapter 1, understanding the life cycle of molecular species during the star formation process is important in order to use them as probes of star forming environments. Current models of chemical evolution of star forming regions and molecular clouds allow us to estimate the timescales for creation and destruction of molecules in those environments, which may be used to constrain the age of clouds. In the CCS-NH_3 scenario, early works found CCS to be more abundant in starless cores (CCS) while NH_3 was mainly found in active star forming regions (NH_3), which suggested that the relative abundance of these molecules is related to cloud evolution (Suzuki et al. 1992; Hirahara et al. 1992; Benson et al. 1998).

To continue our study of the CCS-NH_3 anticorrelation, we will analyze a star-forming region in a very early stage of evolution, the dense cloud GF9-2 (also known as L1082C), one of the star-forming regions with CCS emission detected by de Gregorio-Monsalvo et al. (2006) using the Robledo 70m antenna. This cloud is part of the east-west filamentary dark cloud GF9, located at an estimated distance of 200 pc (Wiesemeyer et al. 1998), which contains several YSOs (Wiesemeyer et al. 1999). The core GF9-2 has a mass of $\simeq 3$ $M_\odot$ (Furuya et al. 2006) and contains a very young stellar source (that we will refer to as GF9-2 mm), identified as a class 0 source by Wiesemeyer (1997) and Wiesemeyer et al. (1999). The age estimated for GF9-2 mm is $\simeq 500$ years, which indicates this is a very young low-mass protostar (Furuya et al. 2014b). This source has an estimated bolometric temperature of less than 20 K and bolometric luminosity of $\simeq 0.3$ $L_\odot$. The circumstellar material around GF9-2 mm is probably traced by the infrared source IRAS F20503+606 (Ciardi et al. 1998; Furuya et al. 2014a).

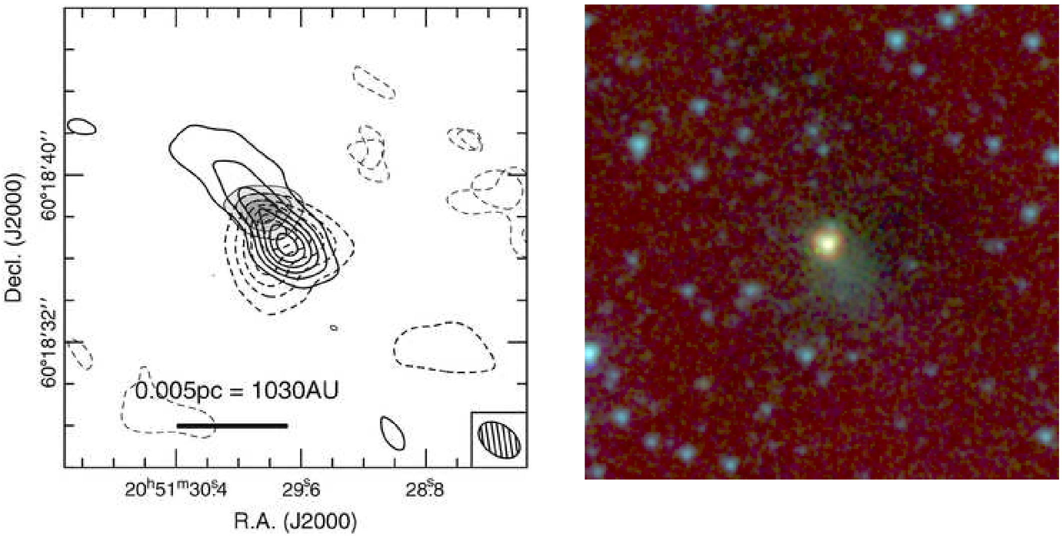

Figure 4.1: (Left) An overlay of the ^{13}CO$(3-2)$ wing emission on the 840 μm continuum emission map of Furuya et al. (2014b). The solid and dashed contours are the blue and redshifted wing emission integrated from -5.6 to -4.4 km s^{-1} and from -0.4 to $+7.2$ km s^{-1} respectively. Thin contours with greyscale are the continuum emission map. (Right) False color Spitzer image (blue: 3.6 micron, green: 4.5 micron, red: 8.0 micron) toward GF9-2. The size of the image is 2×2 arcminutes.

Early studies considered that GF9-2 mm did not have an extensive molecular outflow, although some weak low-velocity gas was found toward this source (Bontemps et al. 1996; Furuya et al. 2006). Weak H_2O maser emission was also detected by Furuya et al. (2003), using the Nobeyama antenna. Radio continuum emission from ionized gas was not detected in GF9-2 (Furuya et al. 2006), indicating that the mass-loss processes in the region are not powerful enough to significantly ionize gas via shocks (Anglada et al. 2018). More recent observations of the ^{13}CO$(3-2)$ transition (Furuya et al. 2014b) showed a compact outflow in GF9-2 (see Fig. 4.1, left), with an extent of $\sim 4.5''$ (900 AU at a distance of 200 pc, Wiesemeyer et al. 1998). The presence of this outflow is also suggested in the Spitzer image of Fig. 4.1 (right) which we retrieved from the publicly available Spitzer images. In this image, a weak blue nebulosity (probably reflected light) emerges from the central source towards the south-east ($\sim 26''$ long), in approximately the same direction of the blue lobe of the outflow, and could be tracing a cavity opened in the envelope by it.

In the context of our CCS-NH_3 comparative study, GF9-2 is one of the best candidates to study the relative distribution between these molecules in a region of recent star formation, because of the youth of GF9-2 mm and the lack of strong disturbances by the outflow activity on the cloud. In principle, we may expect that the CCS emission could be present around GF9-2 mm, forming a ring-like structure as previously found on other YSOs observed with interferometers (Kuiper et al. 1996). However, the single dish observations of Furuya et al. (2006) in GF9-2 found extended emission in transitions like

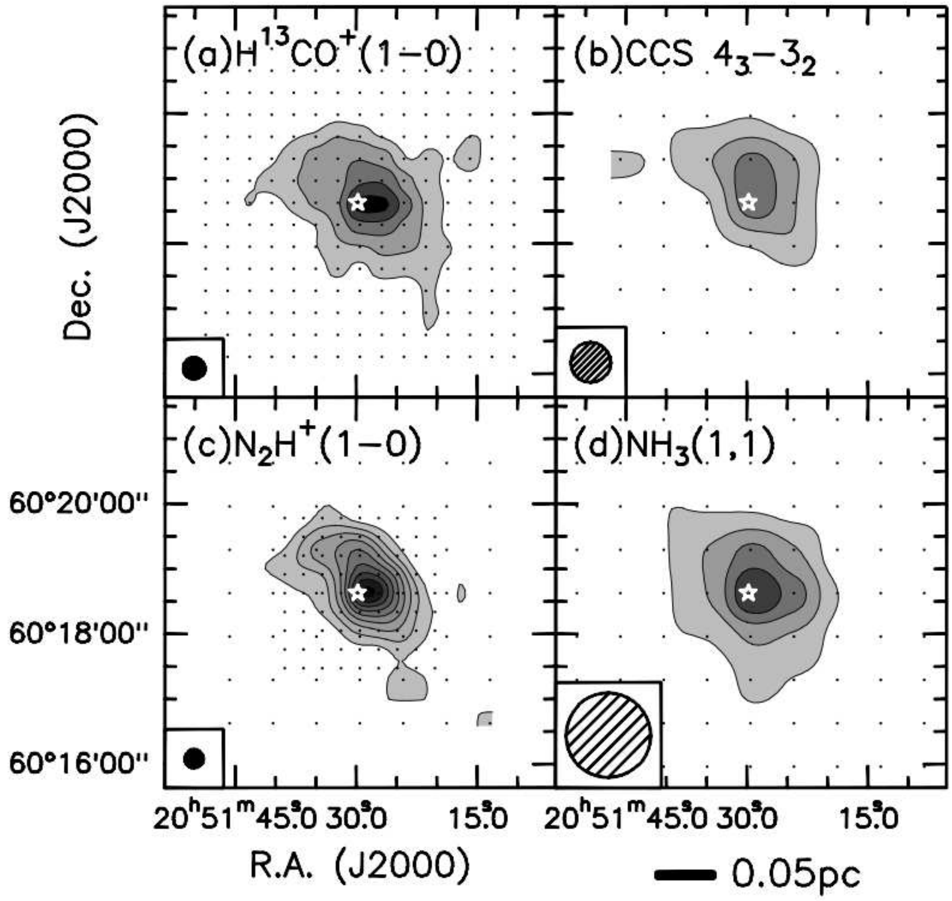

Figure 4.2: Integrated intensity maps of molecular transitions observed in GF9-2 (Furuya et al. 2006). The central star marks the position of the 3 mm source. Dots represent the observed grid points. The FWHM of the beams are shown at the bottom left corner of each map.

NH_3 (1,1) and CCS ($4_3 - 3_2$) (see Fig. 4.2), but the relatively low resolution of those observations (HPBW 78″ and 40″ respectively) did not allow them to resolve the small scale structure.

On the other hand, in previous works GF9-2 mm showed it could be a good candidate to study core collapse, given that it showed a blueskewed profile in optically thick lines (see Fig. 4.3) like HCO^+ and HCN (Furuya et al. 2009), with stronger emission at blueshifted velocities with respect to the central cloud velocity, thus suggesting the presence of infall motions (Anglada et al. 1987). To study infall in molecular clouds, molecular lines like NH_3 and CCS could provide relevant information about it, given that these molecules selectively trace dense gas and thus, they can probe the motions in the innermost regions of the infalling gas.

Here we will present interferometric observations of the GF9-2 cloud, in transitions

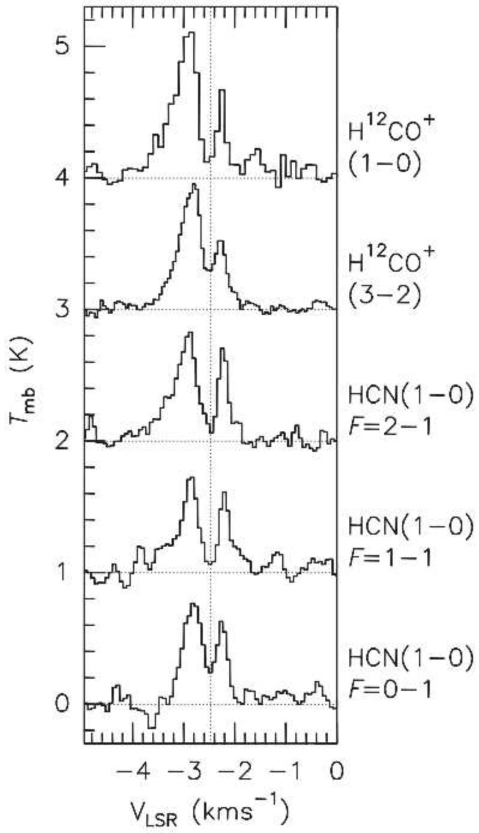

Figure 4.3: Single-dish spectra of the molecular line emission toward the center of the GF9-2 core. The scale is in main-beam brightness temperature (T_{mb}). Taken from Furuya et al. (2009).

of NH_3 and CCS, with the goal of studying the relationship between these molecules in this young star-forming region and, in particular, to search if the CCS/NH_3 spatial anticorrelation is also present in this object at small scales.

4.2 Observations

We carried out observations of the (1,1) and (2,2) transitions of NH_3 (rest frequencies 23694.495 and 23722.633 MHz respectively), the $J_N = 2_1 - 1_0$ transition of CCS and H_2O ($6_{16} - 5_{23}$) maser transition (rest frequency 22344.033 and 22235.079 MHz respectively) towards the source GF9-2, using the VLA in its D configuration (project AD584). The phase center of the field was situated on coordinates R.A. (J2000) = $20^{\mathrm{h}}51^{\mathrm{m}}30\overset{\mathrm{s}}{.}0$, Dec. (J2000) = $60°18'39''$. We observed in 4 IF spectral line mode, which allowed us to cover two lines simultaneously and in dual circular polarization. We used two different tuning setups: one covering both the H_2O and CCS lines on August 12 2008, and the other for both NH_3 transitions on August 24 2008. For CCS and NH_3, the bandwidth was 1.56 MHz, sampled over 127 channels, which provided a spectral resolution of 12.2 kHz (0.16 km s^{-1}). The water maser observations had a bandwidth of 3.12 MHz sampled over 64 channels, giving a spectral resolution of 48.4 kHz (0.66 km s^{-1}). All bandwidths were centered at $V_{\mathrm{lsr}} = -2.7$ km s^{-1}. The total integration time was $\simeq$ 7 hours per tuning setup.

We used the source J0137+331 as the primary flux calibrator, with adopted flux densities of 1.28, 1.24, and 1.18 Jy at 22.2, 22.3, and 23.7 GHz, respectively. Our complex gain calibrator (phase calibrator) was J2022+616 with bootstrapped flux values of 1.8, 1.7 and 1.7 Jy respectively. The source J0319+415 was used as a bandpass calibrator. Data reduction was performed with AIPS, using the recommended procedures for high-frequency data processing. We obtained CCS, NH_3 (1,1) and NH_3 (2,2) maps using Briggs weighting, with a robust parameter of 3 (as defined in task IMAGR of AIPS) to improve the signal to noise ratio. The resulting synthesized beam sizes were $3.5'' \times 3.5''$ P.A. $= -54$ for CCS, $3'' \times 2.8''$ P.A. $= -29$ for NH_3 (1,1) and $3.1'' \times 2.8''$ P.A. $= -40$ for NH_3 (2,2).

4.3 Results

4.3.1 NH_3

The main hyperfine component of the spectrum of the NH_3 (1,1) transition (Fig. 4.4) present two components, one blueshifted and one redshifted relative to the central velocity of the cloud (-2.5 km s^{-1}, Furuya et al. 2006). The two inner satellite lines of the (1,1) transition are also visible in the spectrum, while the external ones are outside our observed bandwidth. The parameters of the main hyperfine lines, obtained with gaussian fits to each component are shown in table 4.1.

Those components are not part of the magnetic hyperfine structure of the transition that is resolved in quiescent cores (Myers & Benson 1983; Benson & Myers 1989). This is

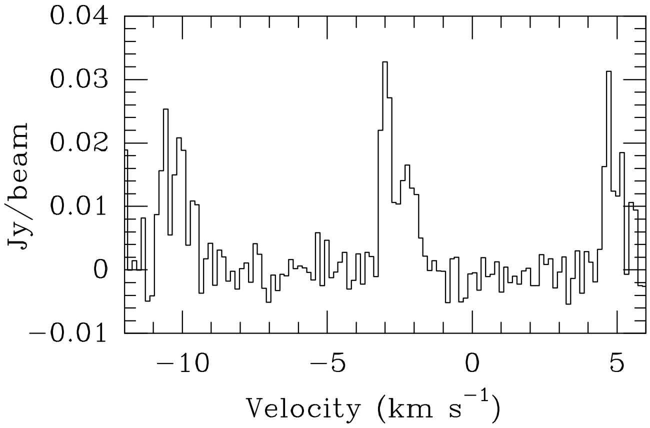

Figure 4.4: Spectrum at the peak of the NH_3 (1,1) map of GF9-2.

Line	Peak (mJy beam $^{-1}$)	V_{LSR} (km s^{-1})	FWHM (km s^{-1})
NH_3 (1,1) blueshifted	33.7	−2.98	0.37
NH_3 (1,1) redshifted	15.5	−2.23	0.75
NH_3 (2,2)	24.1	−2.84	0.29

Table 4.1: Parameters of ammonia lines (main hyperfine components).

because the separation of the two most significant components (lines 8 and 10, see Rydbeck et al. 1977) of the central group of lines of the NH_3 (1,1) transition is 25 kHz ($\sim$ 0.3 km s^{-1}), while the separation between the components of our spectrum is $\sim$0.75 km s^{-1}. We note that the central velocity of the cloud (−2.5 km s^{-1}) is located between the velocity of the two components of our spectrum, which suggests that they are two components separated in velocity or they indicate self-absorption at the central velocities.

The integrated intensity map of the main component of the NH_3 (1,1) transition is shown in Fig. 4.5. The NH_3 emission is mostly distributed west of GF9-2 mm. The peak is located at R.A. (J2000) = $20^\circ 51' 29\overset{''}{.}2$, Dec. (J2000) = $60^{\mathrm{h}}18^{\mathrm{m}}38\overset{\mathrm{s}}{.}00$, close to ($\sim$ 5″) but not coincident with the position of GF9-2 mm (Furuya et al. 2006). The central and stronger emission shows an elongated morphology in east-west direction (a similar trend observed in the N_2H^+ maps of Furuya et al. 2006) while the more extended emission is distributed in the northeast-southwest direction. The negative contours around the ammonia emission suggest the presence of very extended emission, and it may affect the apparent morphology of the lowest ammonia contours. However, an overlay of the 1.2 mm continuum map of Kauffmann et al. (2008) with our NH_3 (1,1) integrated intensity map (Fig. 4.6, left) shows that the ammonia emission is similar to that of dust emission in the region. This is also suggested by the overlay of the Spitzer 8 μm image and our NH_3 (1,1) map (Fig. 4.6, right), with the Spitzer image showing a darker region with similar morphology to the NH_3 (1,1) map. All this is strong evidence that the morphology traced

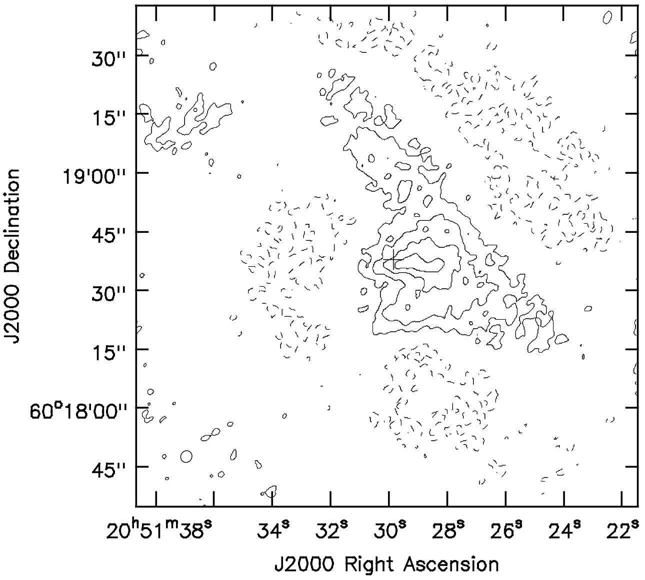

Figure 4.5: Integrated intensity map of the main line of the NH_3 (1,1) transition in the GF9-2 region. Contours are -4, 4, 8, 13, and 17.5 times 1.3 mJy beam^{-1} km s^{-1} (the r.m.s. of our map). The cross marks the position of GF9-2 mm.

by the NH_3 (1,1) emission is real.

The velocity channels of the NH_3 (1,1) transition (Fig. 4.7) show emission distributed on 9 channels around the cloud velocity (-2.5 km s^{-1}). The blueshifted channels show a flat structure in east-west direction, best defined between -3.2 and -2.9 km s^{-1}, which seems to be compact and with no significant extended emission. The redshifted channels show a weaker and more extended structure in the northwest-southeast direction.

In the map of the mean velocity (moment 1, Fig. 4.8) we see that the flat central structure and a filament south of it are blueshifted, while the rest of the map has more redshifted velocities. The flat structure also shows a gradient in east-west direction, being more blueshifted around the position of GF9-2 mm. The map of the velocity dispersion (moment 2, Fig. 4.9) shows significant velocity dispersion (up to $\simeq$ 490 m s^{-1}) towards the center of the map, at $\simeq 10''$ west from GF9-2 mm.

The spectrum of the NH_3 (2,2) transition (Fig. 4.10) shows that the main component is located at $V_{LSR} \sim -2.84$ km s^{-1}, and has a FWHM of 0.29 km s^{-1}, with a peak value of 24.1 mJy beam^{-1}. None of the satellite lines of this transition is visible in our spectrum, because they are outside our bandwidth. The velocity channels of NH_3 (2,2) (Fig. 4.11) show weak emission distributed in five channels around the cloud velocity.

In the integrated intensity map of this transition (Fig. 4.12), the central emission

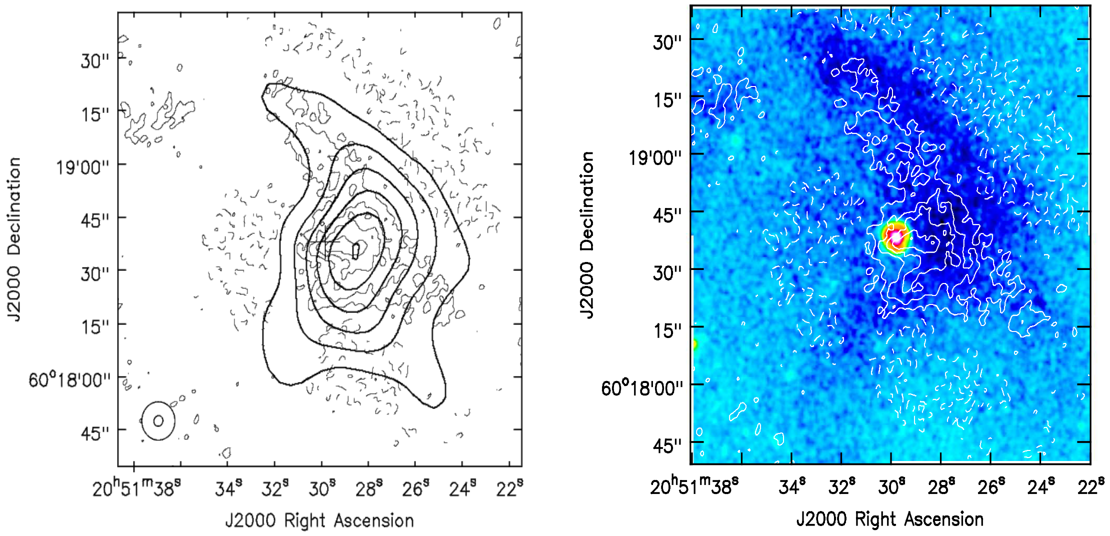

Figure 4.6: (Left) Overlay of the 1.2 mm map of Kauffmann et al. (2008) and our NH_3 (1,1) map. For the 1.2 mm map, first contour is 15 mJy beam^{-1}, and contour step is 5 mJy beam^{-1} (r.m.s is 1.5 mJy beam^{-1}). The NH_3 (1,1) map is the same as in Fig. 4.5. Beam sizes are shown at the bottom left corner of the map (11″ for the 1.2 mm map). The cross indicates the position of GF9-2 mm (Furuya et al. 2006). (Right) Overlay of the Spitzer image at 8 μm and the NH_3 (1,1) map.

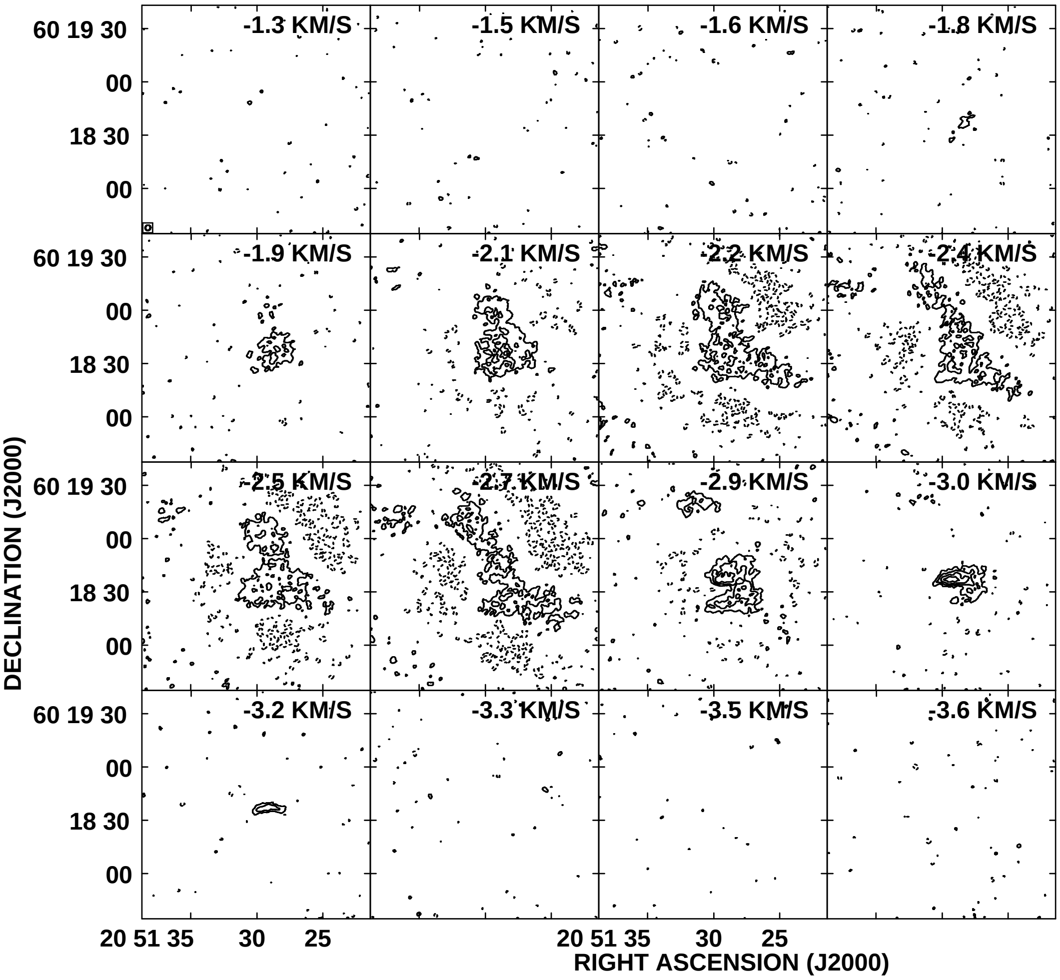

Figure 4.7: Velocity channels of the NH_3 (1,1) transition. Contours are -3, 3, 6, 9 and 12 times 2.6 mJy $beam^{-1}$ (the r.m.s. of our map).

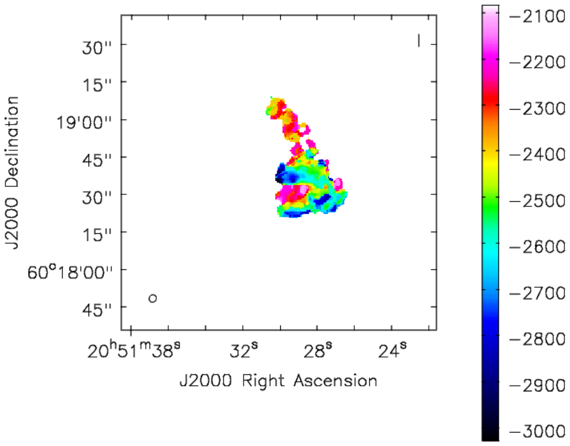

Figure 4.8: Map of the first order moment of the NH_3 (1,1) transition. The color scale is the LSR velocity in m s^{-1}.

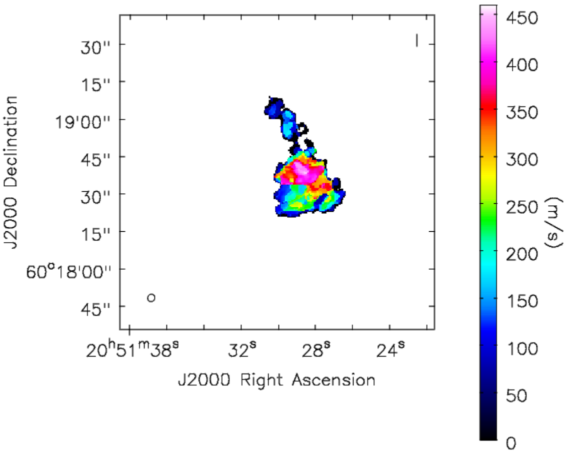

Figure 4.9: Map of the second order moment of the NH_3 (1,1) transition. The color scale is velocity in m s^{-1}.

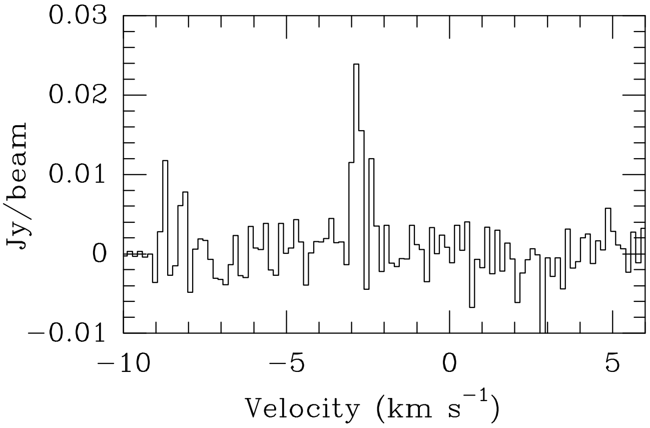

Figure 4.10:
NH_3 (2,2) spectrum at the peak of the map.

shows an elongated morphology in east-west direction, which appears to trace the inner part of the flat structure of the NH_3 (1,1) map. The peak value of the transition is located at R.A. (J2000) = $20^h51^m29\overset{s}{.}0$, Dec. (J2000) = $60°18'36.50''$. The NH_3 (2,2) peak is located $\sim 2''$ from the NH_3 (1,1) peak, and $\sim 6''$ from the GF9-2 mm (a similar distance from peak value of N_2H^+ found by Furuya et al. 2006 with OVRO observations). On the other hand, the first and second-order moments of the transition do not show any clear trend, since the emission is weak and it is detected over very few channels over the S/N threshold used to produce these moments.

The map of the ratio of the integrated intensities of the main components of NH_3 (2,2) and NH_3 (1,1) transitions (Fig. 4.13), which is a tracer of rotational temperature (equation 2 in the Appendix) show higher values at the center of the flat structure. The peak of the ratio seems to be near the peak of N_2H^+ (Furuya et al. 2006). Given that the NH_3 (2,2) and the 1.2 mm maps show their peaks at the same position, it indicates a higher temperature and density at that location. This may indicate the presence of a protostar, or a pre-protostellar condensation of material (as suggested by Furuya et al. 2006).

Using the assumptions and formulas given in the Appendix, we estimated peak rotational and excitation temperatures of $T_{\rm rot}$ = 14 K and $T_{\rm ex}$ = 12 K for ammonia. These are close to one another, suggesting that the emission is close to full thermalization and these derived temperatures are close to the actual kinetic temperature. Using the software CLASS we found an opacity of $\tau = 6.7$ for the NH_3 (1,1) transition. Other physical parameters (molecular and total hydrogen column densities, as well as masses) are given in Table 4.2.

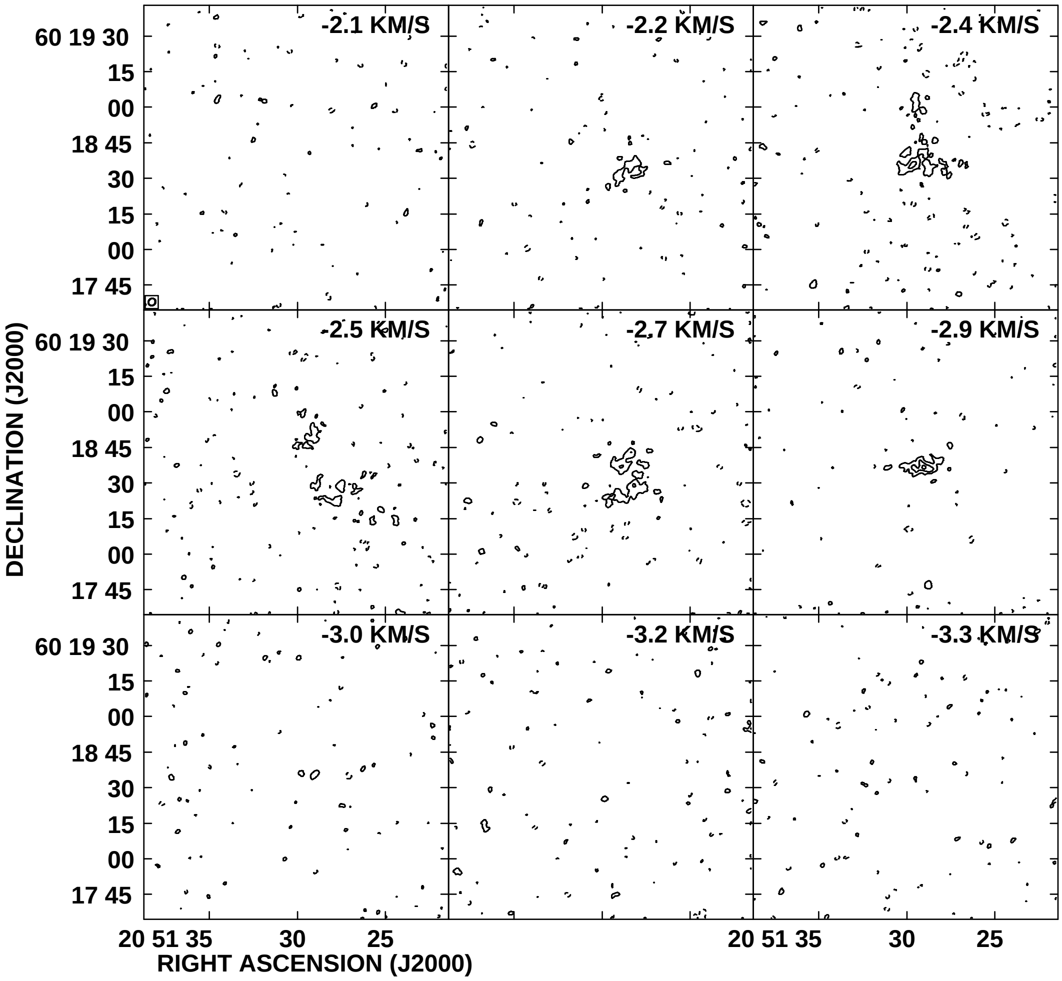

Figure 4.11: Velocity channels for the NH_3 (2,2) transition in the GF9-2 region. The beam is shown at the bottom left corner of the first panel. Contours are -3, 3, 6 and 9 times 2.5 mJy beam^{-1} (the r.m.s. of our map).

Molecule	N_{Mol} (10^{13} cm^{-2})	N_{H_2} (10^{23} cm^{-2})	M_T ($M_\odot$)
CCS	2.5	2.8	1.8
NH_3	80	0.8	2.0

Table 4.2: Physical parameters of of GF9-2 obtained from CCS and NH_3 spectra.

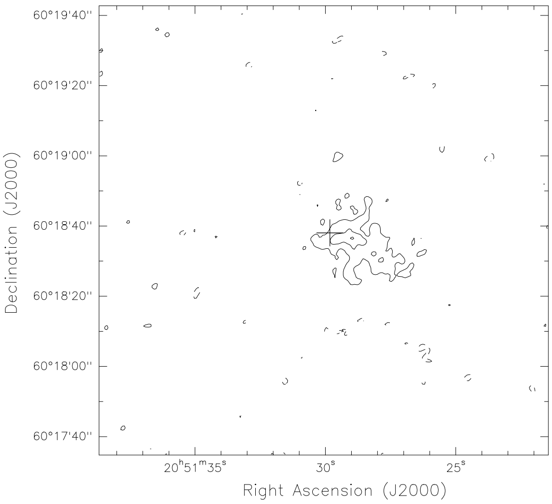

Figure 4.12: Integrated velocity map for the NH_3 (2,2) transitions in the GF9-2 region. Contours are -3, 3, 6 and 9 times 1.0 mJy beam^{-1} km s^{-1} (the r.m.s. of our map). The cross marks the position of GF9-2 mm.

4.3.2 CCS

The spectrum of the CCS ($J_N = 2_1 - 1_0$) transition (Fig. 4.14) shows a narrow component centered at -2.4 km s^{-1} (almost coinciding with the estimated velocity of the GF9-2 cloud) with a width of $\Delta v = 0.17$ km s^{-1} and a peak intensity of 23.1 mJy beam^{-1}. The narrow linewidth suggests a quiescent medium, which is is also evident in the velocity channels (Fig. 4.16) that show emission in only two channels.

The integrated intensity map of the CCS transition (Fig. 4.15) shows emission located north-east of GF9-2 mm, peaking $\sim 10''$ of this source. The emission appears distributed as a relatively compact core with internal clumpy substructure and extended emission, evidenced by the negative contours in the map. The overlay of our integrated intensity maps of the NH_3 (1,1) and CCS (Fig. 4.17) shows emission of the two molecules distributed in the form of cores located close to each other but spatially distinct. The peaks of the two transitions are separated by $\simeq 15''$.

As the CCS line is very narrow compared to our spectral resolution, moments 1 and 2 do not give us any useful information. We estimated physical parameters of this transition using the methods indicated in the Appendix, and the results are given in table 4.2. The total mass derived from the CCS transition is 1.8 $M_\odot$ (Table 4.2).

4.3.3 H_2O maser

Previous single dish observations of Furuya et al. (2003) found weak H_2O maser emission, at $V_{LSR} = 8.4$ km s^{-1} (i.e., redshifted with respect to the cloud velocity), with a flux density of 377 mJy, in spectra with an rms noise of 47 mJy. They assume that the

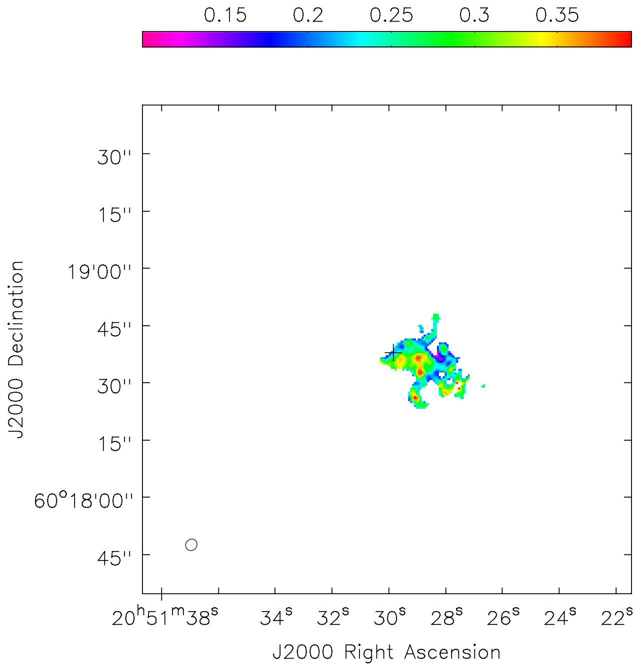

Figure 4.13: Map of the ratio between the integrated intensities of the NH_3 (2,2) and NH_3 (1,1) main lines in GF9-2. The cross indicates the position of GF9-2 mm.

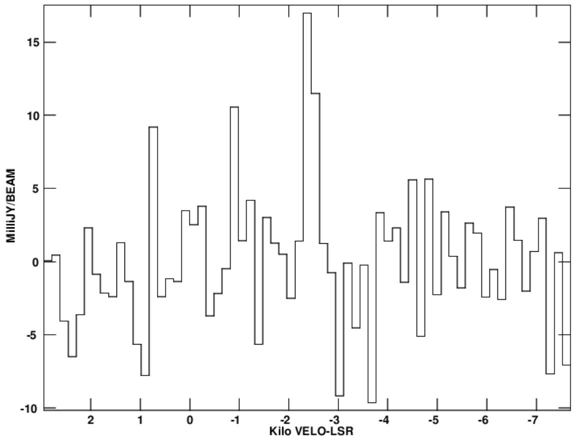

Figure 4.14: Spectrum taken at the peak of the CCS emission from of our GF9-2 map.

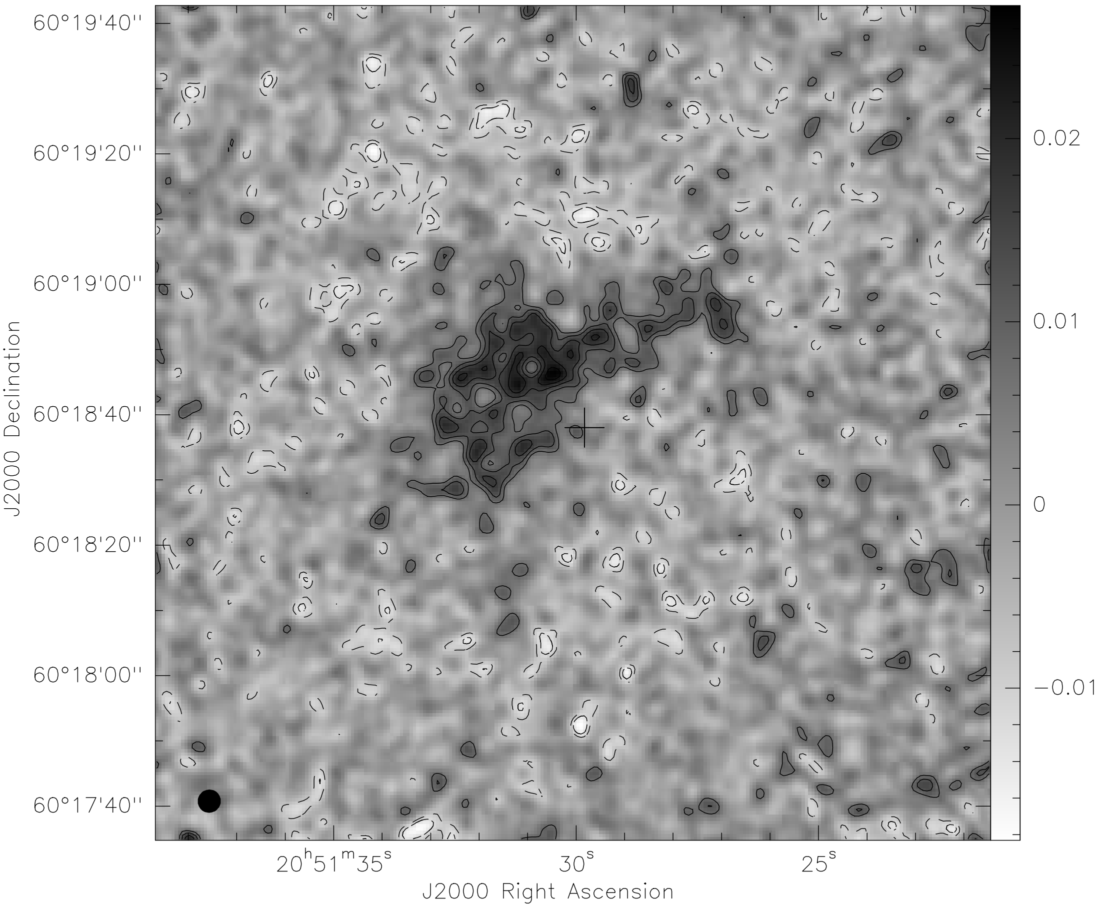

Figure 4.15: Integrated velocity map of the CCS ($J_N = 2_1 - 1_0$) transition in the GF9-2 region, from -2.5 to -2.4 km s^{-1}. Contours are -3, -2, 2, 3, 4, 5, and 6 times 0.7 mJy beam^{-1} km s^{-1} (the r.m.s. of our map). The beam size is $3.6'' \times 3.5''$, shown at the bottom left corner of the map. The cross indicates the position of the protostar GF9-2 mm (Furuya et al. 2006).

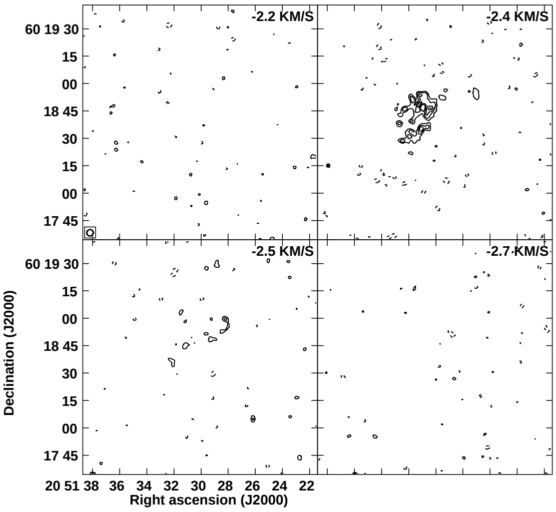

Figure 4.16: Velocity channels for the CCS ($J_N = 2_1 - 1_0$) in GF9-2 region. The beam is shown at the bottom left corner of the first panel. Contours are -3, 3, 4, 5 and 6 times 2.9 mJy beam^{-1} (the r.m.s. of our map).

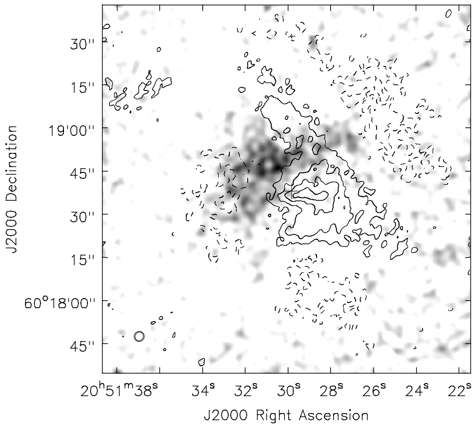

Figure 4.17: Overlay of the integrated velocity map for the CCS ($J_N = 2_1 - 1_0$) transition (greyscale) and the NH_3 (1,1) transition (contours) in the GF9-2 region.

maser emission arises from GF9-2 mm, which would represent the lowest-luminosity YSO in which this type of emission had been found. However, we did not detect any maser emission in our sensitive interferometric observations (rms= 1.7 mJy beam^{-1}). Our observations were designed to simultaneously observe the CCS thermal line and the H_2O maser, to self-calibrate the latter and apply the phase and amplitude correction to the (supposedly weaker) CCS lines. Of course, this self-calibration was not possible in GF9-2 due the maser non-detection.

Without questioning the validity of the data presented by Furuya et al. (2003), we note, however, that theirs were single-dish observations with a beam size of $75''$. Thus, there is no guarantee that the detected emission actually arises from GF9-2 mm, given our non-detection in observations with a much better astrometric accuracy. The possible implications of this non-detection are discussed in detail in Chapter 5.

4.4 Discussion

4.4.1 CCS-NH_3 anticorrelation

We consider we found small scale ($\sim 4''$) spatial anticorrelation between CCS and NH_3 in GF9-2. Our maps (Figs. 4.15 and 4.17) showed that the CCS emission is almost absent at the position of GF9-2 mm and it is concentrated at locations where little or no NH_3 emission is present. The location of GF9-2 mm is outside the area enclosed by the lowest CCS contour, by at least $\sim$ 900 AU, but this is shorter than the typical distance at which CCS emission can be found around young stellar sources (a few thousand AU, Aikawa et. al 2001). We did not find the CCS ring-like structure seen in sources in early stage of evolution like the dark cloud L1498 (Kuiper et al. 1996; Tafalla et al. 2006), probably because the CCS molecules are fully depleted in the area occupied by the ammonia core.

Our CCS spectrum showed that the linewidth of the transition (0.17 km s^{-1}) is within the typical value that can be found in molecular clouds with CCS lines (total linewidth $\leq$ 0.25 km s^{-1}, Lai & Crutcher 2000). This narrow linewidth suggests the area of the GF9-2 cloud traced by CCS has not been affected by the activity of the region (e.g., outflowing/infalling motions, turbulence or temperature enhancements).

Moreover, the CCS line (centered at -2.4 km s^{-1}) is located between the blueshifted and the redshifted components of the NH_3 (1,1) transition (located at -3 and -2.2 km s^{-1} respectively, see Fig. 4.4), and thus, CCS is tracing the ambient velocity more accurately. Given that the CCS is optically thinner that the NH_3 line, we consider that the NH_3 (1,1) spectrum may be affected by self-absorption, which was also suggested by Furuya et al. (2006) with observations of CCS ($4_3 - 3_2$) and ^{12}CO(3-2).

The presence of the relatively strong and quiescent CCS clump in the maps seems to indicate the early stage of the region, which along with its anticorrelation with the NH_3 emission appears to agree with the time-dependent chemistry scenario suggested by Suzuki et al. (1992). The relative distribution of these molecules suggests that we may be observing a chemical transition of the dense gas in GF9-2, where the ammonia emission is becoming more significant in the denser regions (traced by NH_3 and dust), while simultaneously CCS molecules are depleted. The region with CCS emission appear to be quiescent because they are still not affected by the activity of the outflow, but it is expected that the CCS emission will decrease with time as the region continues to evolve.

However, regarding the spatial distribution of CCS, we note a discrepancy between our map of the CCS $(2_1 - 1_0)$ transition (Fig. 4.15) and the CCS $(4_3 - 3_2)$ map of Furuya et al. (2006, Figs. 4.2), and in fact, if we compare our NH_3 map with the CCS one of Furuya et al. (2006), the anticorrelation between these molecules is not too evident. The different aspect of the two CCS maps may be due to a number of reasons, such the filtering of large-scale emission in our interferometric map, the different angular resolutions, or the different excitation conditions of the two CCS transitions involved.

We see that, in the Furuya et al. (2006) map, the strongest CCS emission covers an area of about 30×60 arcsec, while our $(2_1 - 1_0)$ map shows emission distributed in a smaller area with the peak position at $10''$ north-east of GF9-2 mm. The whole CCS map of Furuya et al. (2006) covers an area of $\sim 5' \times 5'$, with a beam size and gridding spacing of $40''$, while our CCS map covers $2' \times 2'$ with a beam size of $3.5''$. Considering these characteristics, the difference in appearance might be due to different spatial resolution of the observations, if weak extended structures dominate the emission seen in the single-dish images.

Additionally, we know that our CCS $(2_1 - 1_0)$ map presents extended emission (indicated by the negative contours of our CCS map), which implies that part of the CCS emission may be missing in our images. Our interferometric observations filter out structures with the largest spatial scales ($\gtrsim 60''$). On the other hand, the larger structures not seen by the interferometer could be observed in the single dish maps, which could explain the different morphology.

However, an interesting possibility to explain this distribution discrepancy is that the two CCS transitions are excited in different way. For example, in the dark cloud L1498, Wolkovitch et al. (1997) found that the transition $(4_3 - 3_2)$ is typically stronger than the $(2_1 - 1_0)$ for most densities, by using a large velocity gradient (LVG) code (see Fig. 4.18 left). Under these conditions, in the outer regions of the cloud (where gas density is lower than in the innermost regions) the $(4_3 - 3_2)$ emission may be stronger than the $(2_1 - 1_0)$ transition, being comparable only for densities $\sim 10^{3.5}$ cm^{-3}. However, there are abundance and density conditions under which the $(2_1 - 1_0)$ transition can be stronger (Fig. 4.18 right). In particular, for high CCS abundance and/or low hydrogen density. These could be the conditions of the areas traced by our CCS maps, which may explain in part its different distribution as compared with the maps shown by Furuya et al. (2006). To disentangle all these possible explanations, we would need observations of different CCS transitions with a similar angular resolution. These observations could provide us with valuable information on the variation of CCS abundance across the core (Fig. 4.18).

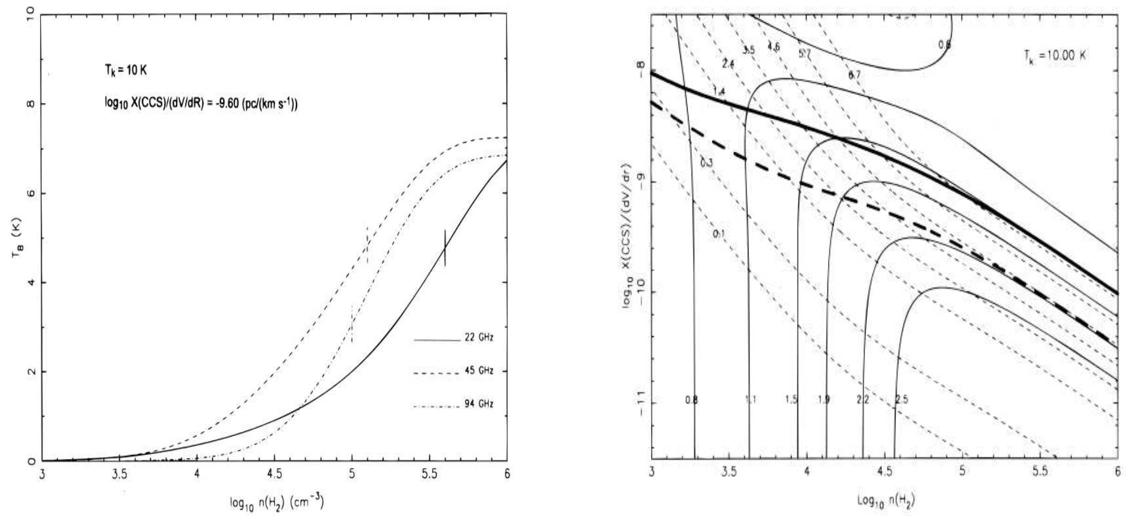

Figure 4.18: (left) Excitation calculation for the CCS $(2_1 - 1_0), (4_3 - 3_2,)$ and $(8_7 - 7_6)$ transitions at 22, 45 and 94 GHz respectively for a particular CCS abundance with respect to H_2, where T_B is brightness temperature and n(H_2) is hydrogen density. (right) Contours of T_B(45 GHz)/T_B(22 GHz) (thin solid line) and T_B(45 GHz) (thin dashed lines). The ratios are indicated by the values that accompany each curve. The thick solid and dashed lines indicate the conditions where the optical depths of the 22 and 45 GHz transitions reach unity. From Wolkovitch et al. (1997).

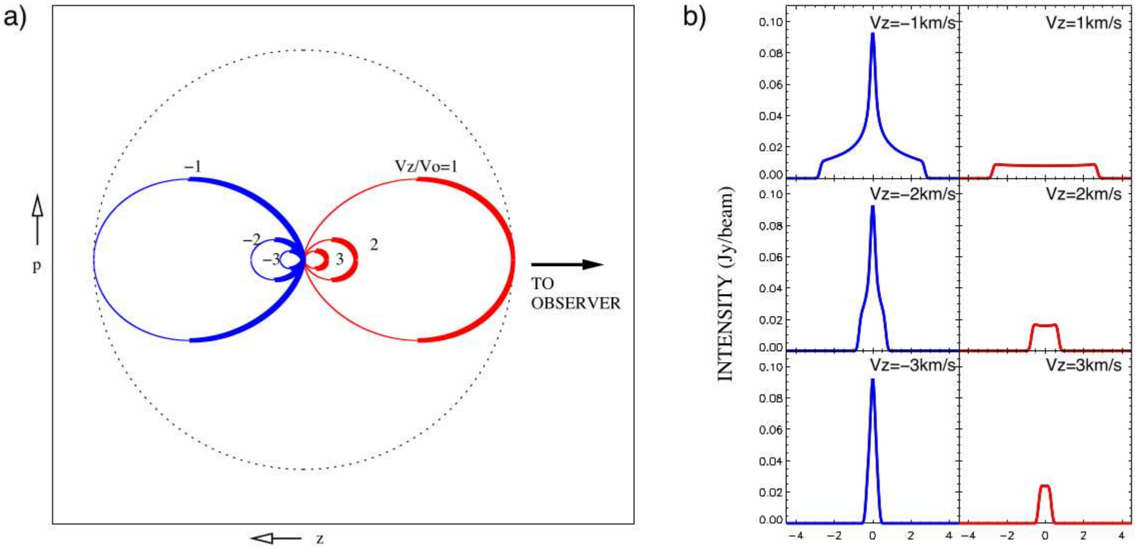

Figure 4.19: (a) Surfaces of equal l.o.s. velocity for collapsing protostellar envelope. The blue and red lines represent an isovelocity surface (b) Intensity as a function of angular offset taken from the source center for channel maps of different velocities (Mayén-Gijón et al. 2014).

4.4.2 Infalling motions in GF9-2

The NH_3 (1,1) spectrum in Fig 4.4 shows the characteristic blue-red asymmetry, with a more intense blueshifted emission, expected in optically thick lines in the presence of infall motions (Anglada et al. 1987). This asymmetry is also seen in the spectra of other molecules in the region (Furuya et al. 2009, Fig. 4.3) but we are observing it at smaller scales, of $\sim 3''$ ($\sim$ 600 AU at a distance of 200 pc).

Further evidence for infalling motions is also seen in our maps. As described in section 4.3.1, our NH_3 maps show weaker and extended emission in the redshifted channels and a stronger and flat structure of the blueshifted gas (Fig. 4.7). This flat structure is also present in other transitions, like $H^{13}CO^+(1-0)$ (Furuya et al. 2006), although it is more clearly defined in our maps. Our NH_3 moment 1 map (Fig. 4.8) showed a gradient in east-west direction along the flat structure, with more blueshifted emission close to the peak of the integrated intensity map, which reminds us of the blue-spot signature defined by Mayén-Gijón et al. (2014). This signature can be used to identify regions that present infall motions, mainly in high-mass star forming regions. This is the first time this effect is seen in a low-mass star-forming region.

To understand the infall scenario of Mayén-Gijón et al. (2014), in Fig. 4.19 we present their schematic view of a cloud experiencing infall, which show equal line of sight (l.o.s.) velocity surfaces for a collapsing protostellar envelope. This scenario assumes that the velocity increases at distances closer to the central object, as expected in an inside-out collapse.

This scheme is based on a study of infall signatures for spherically symmetric protostellar core, for the case of optically thick line emission. In this scenario, gravitational motions due to infall dominate the kinematics of the cloud over turbulent and thermal motions (Anglada et al. 1987; Mayén-Gijón et al. 2014). Even though the cloud GF9-2 does not show spherical symmetry, we can use the results of those works to study the presence of infall in this cloud.

In Fig. 4.19a we see that a given l.o.s. intersects each isovelocity surface at two points. If the line is optically thick, the emission facing the observer (indicated by the thick line) is visible, but the emission from the rear part (thin line) is absorbed by the former. If we compare red- and blueshifted isovelocity contours with the same absolute velocity, we see that the whole emitting region of the redshifted one is farther away from the center of the core. The images of these channels (Fig. 4.19b) would show weak emission, which is nearly constant, with a slight decrease around the projected center of the image (corresponding to areas farther away from the center of the core).

On the other hand, the blueshifted channels would show emission from a region closer to the core center (thus, being hotter). The emitting regions close to the projected center of the images are significantly hotter, and the observed intensity strongly peaks at the image center (Fig. 4.19b). We can also see in Fig. 4.19b that both red- and blueshifted images show intensity profiles whose width decreases as the velocity increases. As a result of this velocity structure, the integrated intensity (zero-order) maps will peak towards the central position, mainly due to the stronger blueshifted emission.

However, the main signature to identify infall, the blue spot, is found in the first-order maps (intensity-weighted mean velocity). This signature is a compact spot of blueshifted emission located at the position of the zero-order moment peak. The blue spot is originated by the differences in intensity and the spatial distribution of the emission in the red- and blueshifted channels of a region experiencing infall.

Applying this scenario to GF9-2, we may interpret that the emission of the blueshifted channels of our NH_3 (1,1) maps (see Fig. 4.7) indicates that the flat structure is probably being formed in the inner and hotter regions of GF9-2. On the other hand, the redshifted channels appear to show emission originated in colder and external regions of the cloud, because they present weak and more extended emission. These trends suggest that GF9-2 may be experiencing infall, according to the model of Mayen-Gijon et al.

Moreover, the spot of blueshifted emission inside the velocity gradient seen in Fig. 4.8 appears to be the blue spot defined by Mayén-Gijón et al. (2014). We note that the velocity gradient is only seen in the flat structure, but not in the rest of the map, where no clear gradient is evident. This is in contrast with the maps observed in high mass regions, where the gradient and blue spot are usually well defined (see for example Fig. 2 of Mayén-Gijón et al. 2014). However, most of those maps correspond to higher excitation transitions of NH_3. The non-uniformity of the gradient in our map may be explained by considering that the lower transitions like the NH_3 (1,1), and (2,2), have more contribution of relatively colder gas than the gas traced by the high transitions observed in high mass

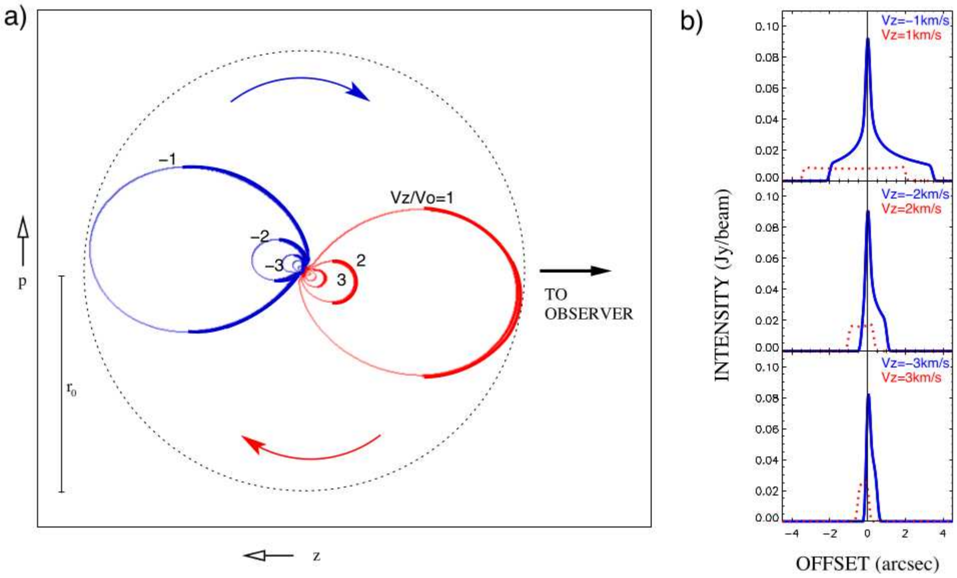

Figure 4.20: (a) Contours of equal l.o.s. velocity for a collapsing and rotating protostellar envelope in a plane close to the equator. (b) Intensity as a function of angular offset from the source center, in equatorial direction, for channel maps of different l.o.s. velocity. Taken from Mayén-Gijón et al. (2014).

star forming regions. Therefore, a transition like the NH_3 (1,1) may show a well defined velocity gradient in the most dense and hot region of the collapsing cloud, and a less uniform gradient in colder outer areas.

We also note that the velocity structure of our NH_3 maps is more tangled than the mere presence of a blue spot in the moment 1 map, suggesting that a more complex scenario than simple infall may be at work in this source. This is discussed in the following section.

4.4.3 Infall and rotation

In the case of both infalling and rotating motions, the analysis of Mayen-Gijon et al. (2014) considers a system with similar properties like the one used in the infall system of Anglada et al. (1991), with a velocity field pattern given by Terebey et al. (1984). In this case (see Fig. 4.20a), the isovelocity surfaces are misaligned relative to the l.o.s. due to rotation.

This results in images with a noticeable difference with respect to the infall case, since the intensity distribution would be asymmetric with respect to the rotation axis. This can be explained by noting that, in the side where infall and rotation have the same sign, their velocity components will add together to produce isovelocity surfaces with points located farther away from the center (more extended surface) with respect to case of pure radial infall. On the other hand on the side where the velocity components of infall and

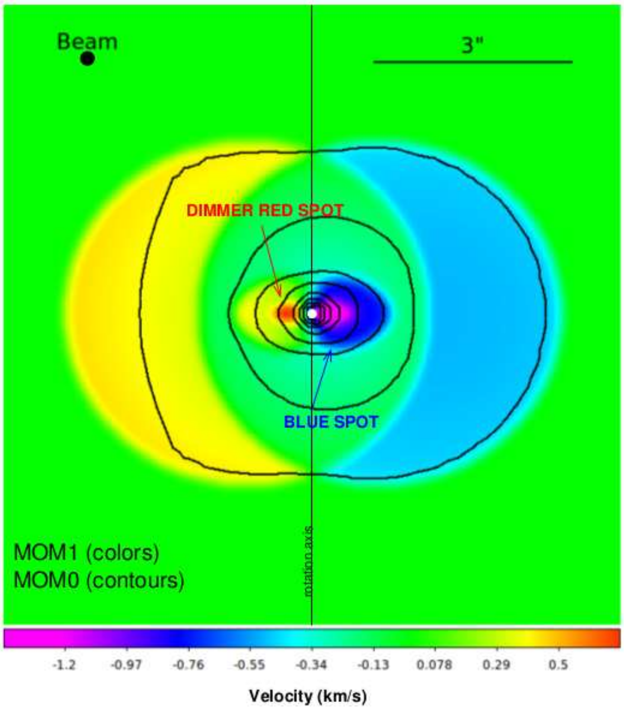

Figure 4.21: Overlay of an intensity-weighted mean velocity map (first-order moment, color scale) and the integrated intensity map (zeroth-order moment, contours) of an infalling rotating envelope (Mayén-Gijón 2015).

rotation have different sign the isovelocity surface will contain points located closer to the center (more compact surfaces) than the case of pure infall. Thus, emission will be more extended in the side where the velocity components of rotation and infall have the same sign and will be more compact in the opposite side (see Fig. 4.20b).

In the zeroth-order moment (Fig. 4.21), the integrated emission will not be symmetric respect to the center of the core, but it will be stronger on the blueshifted rotating side. The consequence is that the peak of the zeroth-order moment would not coincide with the actual center of the core.

In the moment 1 maps, the main difference is that the blue spot is even more blueshifted than the blue spot observed in the case of infall only, and it is located toward the blueshifted rotating side of the cloud. Another especial characteristic is the occurrence of a red spot, which is located on the opposite side of the rotating gas, and close to the rotation axis.

In our case, the emission of the blueshifted channels is more compact and stronger than the emission of the redshifted channels (Fig. 4.7), and this emission is located west of GF9-2 mm. Therefore, we suggest that our data can be interpreted as tracing rotation and infall, following the models of Mayen-Gijon et al. (2014).

Considering that the flat structure is oriented in the east-west direction, we may assume that the rotation axis is probably oriented in the north-south direction. Regarding this, we know that the peak of the integrated emission of NH_3 (1,1) is separated of GF9-2 mm by $\sim 6''$, and this separation could be related to the effect mentioned in zeroth-order moment map discussed above. In this scenario, GF9-2 mm could be the central source of the infall and rotation motions, but these motions would produce an asymmetry of the NH_3 (1,1) emission with respect of the rotation axis, producing the separation of the NH_3 (1,1) peak with respect to GF9-2 mm.

The non-detection of the expected red spot and of the velocity gradient of the redshifted channels along the flat structure may be explained by noting that the emission of those channels is extended, weak and may correspond to the external (and colder) material. Moreover, the low signal-to-noise ratio of the emission east of GF9-2 mm may preclude the detection of these particular characteristics. More sensitive observations would be then necessary to search for these signatures.

4.5 Conclusions

In this chapter, we present VLA observations of NH_3 and CCS toward the low-mass star-forming region GF9-2. We can summarize our main results as follows:

- CCS and NH_3 emissions are clearly anticorrelated spatially, each tracing a distinct region. The CCS clump traces gas that do not seem to be perturbed by the activity of the region, and may be a remnant of the initial core. The NH_3 emission shows a richer kinematical and temperature structure, with higher densities and temperature close to the source GF9-2 mm, a low-luminosity YSOs powering a compact molecular outflow.
- This anticorrelation is present up to very small scales ($\sim 4''$). But we did not identified CCS enhancement in this region.
- We note a discrepancy between the spatial distribution in our CCS maps, and that seen in previous works using a different CCS transition. This could be an instrumental effect, but we suggest that it could be due to the different excitation conditions of the transitions.
- We suggest that the evolutionary stage of the cloud GF9-2 is in agreement with the scheme proposed by Suzuki et al. (1992) for CCS and NH_3. GF9-2 shows the chemical evolution that corresponds to a young active star forming region, where weak outflows still do not have significant interactions with the ambient cloud.
- Our NH_3 velocity channel maps show very differentiated emission. While the redshifted emission is weak and extended, the blueshifted emission is stronger and compact. The asymmetrical NH_3 spectra and the kinematical pattern in the maps suggest that GF9-2 presents collapse and rotation, in accordance to the model of Mayén-Gijón et al. (2014). In particular we emphasize the presence of compact

blueshifted emission, which could represent the blue spot defined by these authors. This is the first time such a blue spot is identified in a low-mass star-forming region.

Chapter 5

Water maser emission in brown dwarfs and low-luminosity young stellar objects

5.1 Introduction

Water maser emission is present in different astrophysical environments, such as young stellar objects (YSOs), evolved stars, and active galactic nuclei (Elitzur 1992; Lo 2005). The most widely studied water maser transition is the one at 22 GHz, which has proved to be a very powerful tool to study these environments, since interferometric observations (in particular using Very Long Baseline Interferometry, VLBI) allow us to reach angular resolutions better than 1 milliarcsec (e.g., Torrelles et al. 2001, 2014; Yung et al. 2011). Thus, we can study processes and structures in these sources with a level of detail unsurpassed by any other technique in Astronomy.

Focusing on the case of water maser emission toward YSOs, we know that it is intense and widespread over a wide range of stellar masses (e.g., Claussen et al. 1996; Forster & Caswell 1999; Furuya et al. 2003; Breen et al. 2010). Interferometric observations reveal a dichotomy in the distribution of water masers in YSOs: while in some sources this type of emission traces collimated jets, in others it traces protoplanetary disks (e.g., Torrelles et al. 1997, 1998). This is important, since the presence of disks and collimated outflows are key ingredients in the formation of stars via accretion. In low-mass ($\lesssim 4$ M$_\odot$) YSOs, water maser emission is consistently found associated with sources in the earliest evolutionary stages. Among objects in the classical evolutionary classes defined by Lada (1987) and André et al. (1993), Furuya et al. (2001) estimated detection rates of $\sim$ 40% in Class 0 objects, 4% in Class I, and 0% in Class II ones. This is understandable, because water masers are thought to be collisionally pumped in post-shock regions (Elitzur et al. 1989; Yates et al. 1997). The youngest YSOs seem to be the ones with more powerful collimated mass outflows (Bontemps et al. 1996; Dionatos et al. 2010; Podio et al. 2012; Watson et al. 2016), which can create shocked regions as they move through the ambient molecular cloud. They also undergo intense accretion (Henriksen et al. 1997), which could pump maser emission in disks.

Collimated outflows and accretion processes are present in YSOs with extremely low mass, and even in substellar objects. Spitzer data revealed the presence of a new class of objects (Young et al. 2004; Kauffmann et al. 2005) named “Very Low Luminosity Objects” (VeLLO). These are objects embedded in dense cores, with internal luminosities < 0.1 $L_\odot$. Some of these objects show Herbig-Haro (HH) emission (Stecklum et al. 2007b; Comerón & Reipurth 2006) and bipolar molecular outflows (André et al. 1999; Bussmann et al. 2007), which are classical signposts of mass-loss processes in higher-mass YSOs. Moreover, even for brown dwarfs (BDs) there is mounting evidence of the presence of accretion (e.g., Muzerolle et al. 2000; Comerón et al. 2000; Fernández & Comerón 2001; Barrado y Navascués & Martín 2003; Luhman et al. 2003; Alcalá et al. 2014), outflows (Whelan et al. 2005, 2007; Palau et al. 2014; Morata et al. 2015), and disks (Natta & Testi 2001; Barrado y Navascués et al. 2007; Scholz & Jayawardhana 2008; Downes et al. 2015; Testi et al. 2016). This evidence suggests that the formation of VeLLOs and BDs takes place in a similar way to solar-type stellar objects. Then, we see that the structures and processes that give rise to water maser emission (accretion/outflows) are also present in these very low mass objects, so it is possible that they also harbor water masers. The difference may be that the water maser emission could be weaker, as it happens when we compare low- and high-mass YSOs (Claussen et al. 1996; Furuya et al. 2001). The energy output in mass-loss processes decreases with stellar luminosity (Anglada 1995), so there may be a mass limit below which maser emission cannot be produced. So far, the lowest-luminosity YSOs reported to possibly harbor a water maser is GF 9-2 ($\simeq 0.3$ $L_\odot$; Furuya et al. 2003). Extending this to lower luminosity objects would allow us to study mass-loss processes and accretion disks at the low luminosity end of the mass spectrum.

Another important category of low-luminosity objects are first hydrostatic cores (FHCs; Larson 1969). These represent the first stage of the evolution of protostars, immediately before dissociation of molecular hydrogen and the subsequent formation of a Class 0 protostar. Some of these FHCs show evidence for collimated outflows (e.g., Chen et al. 2010), and therefore, they might also harbor water masers. Given that a large fraction of Class 0 protostars are water-maser emitters, a search toward the earlier FHC phase would establish the starting point of maser emission in low-mass YSOs.

In this chapter we present a search for water maser emission toward a sample of low luminosity YSOs and substellar objects, to investigate whether their mass-loss processes are energetic enough to power water maser emission. As a longer term goal, the identification of water-maser emitters among these objects would allow us to design VLBI observations to study mass-loss processes in very low luminosity objects at the smallest possible spatial scales.

5.2 Source sample

We compiled 44 sources with declination $\geq -20°$, reported in the literature with $L_{\rm bol} <$ 0.4 $L_\odot$, and/or $M_* <$ 0.15 $M_\odot$, with the main requirement that they show evidence of outflow/accretion and/or signs of youth (e.g., excess emission at millimeter wavelengths).

The sample of 44 sources comprises four groups: i) 20 young BDs; ii) 6 VeLLOs; iii) 7 FHCs; iv) 11 low luminosity objects (LLOs) with $0.1 < L_{\rm bol}/L_\odot < 0.4$ and/or $0.075 < M_*/M_\odot < 0.15$, not included in any of the groups above.

BDs with signs of youth were taken from different samples: young BDs (most of them Class II objects) detected at 1.3 mm by Klein et al. (2003) and Scholz & Jayawardhana (2006); the three young substellar objects classified by White & Hillenbrand (2004) in a spectroscopic optical study of Class I young stellar objects in Taurus-Auriga; Class I BD candidates proposed by Palau et al. (2012) and Morata et al. (2015) using submillimeter and centimeter observations; and Class 0 proto-BD presented in Palau et al. (2014). Regarding VeLLOs and FHCs, we took sources from the compilation of Palau et al. (2014), as well as the globule CB 130, which host several FHC candidates (Kim et al. 2011).

The rest of LLOs were selected from the sources in the Muzerolle et al. (2003) sample with stellar masses < 0.15 $M_\odot$, and estimated ages < 1 Myr, with the exception of CIDA 14, which is reported to have ~ 0.17 $M_\odot$ by Briceño et al. (1999). It is interesting to note that three out of the five selected sources from Muzerolle et al. (2003) present signs of outflow activity from [OI] lines. We also included individual targets which were confirmed to be deeply embedded and of very low mass, such as the detections by Klein et al. (2003), L1415-IRS, a highly variable source (FU Ori-like object) with only 0.13 $L_\odot$, which is also driving HH emission (Stecklum et al. 2007a, 2007b), the triple system IRAS 04325+2402AB/C, first reported by Hartmann et al. (1999), where one of the components could be substellar and driving an outflow (Scholz & Jayawardhana 2008; Scholz et al. 2010), and IRAS 04166+2706, a 0.4 $L_\odot$ source driving an extremely high-velocity and highly collimated outflow (e.g., Tafalla et al. 2004; Santiago-García et al. 2009; Wang et al. 2014). We also included two low-mass dense cores reported by Codella et al. (1997), associated with infrared (IRAS) or submillimeter sources (Di Francesco et al. 2008).

5.3 Observations

5.3.1 Effelsberg

Single-dish observations were carried out with the 100-m Effelsberg radio telescope of the Max-Planck-Institut für Radioastronomie, between 2015 September 29 and 2015 October 3 (observational project 14-14). We used the S14mm receiver, and tuned it to observe the $6_{16}-5_{25}$ transition of the H_2O molecule (rest frequency 22235.08 MHz). The full width at half maximum (FWHM) of the telescope beam at this frequency is $39''$. The backend was the Fast Fourier Transform Spectrometer (XFFT), with a bandwidth of 100 MHz (total velocity coverage of 1348 km s^{-1}) sampled over 32768 channels, providing an effective spectral resolution of 3.5 kHz (0.047 km s^{-1}). For all sources, the spectral bandpass was centered at a velocity with respect to the local standard of rest (kinematical definition, $V_{\rm LSRK}$) of zero. We checked the pointing accuracy of the telescope at least once every hour using nearby calibrators. The rms pointing accuracy was better than $2''$. We observed in position switching mode, alternating on- and off-source scans of 60 seconds each. Each source was typically observed for a total time (on+off) of 30 minutes, although integrations were longer in some cases (e.g., for targets at low elevation). Data were processed with the Continuum and Line Analysis Single-dish Software (CLASS), which is part of the GILDAS[1] package of the Institut de Radioastronomie Milimétrique. The spectra were corrected by the elevation-dependent gain of the telescope and by atmospheric opacity, and were Hanning-smoothed to obtain a final spectral resolution of 0.33 km s^{-1}. Table 5.1 lists the observed positions and the resulting rms of the spectra, which is of the order of 20 mJy in all cases. Note that some sources were observed in different epochs. Given the usually high variability of water masers, we did not average the data of different days, but present the results of the observations of each day individually. Moreover, although our target list comprised 44 sources, only 42 positions were observed, since in the B1 and CB130 fields, the Effelsberg beam included two sources.

5.3.2 Very Large Array

Prompted by a detection in our single-dish observations, we observed a field centered at source L1448 IRS 2E with the Karl G. Jansky Very Large Array (VLA) of the National Radio Astronomy Observatory on 2015 October 14 (project 15B-366). The array was in its D configuration. A baseband centered at 22 GHz was observed with an 8-bit sampler (for a high spectral resolution). Within this baseband, a subband of 8 MHz was used to observe the $6_{16} - 5_{25}$ water maser line and Doppler tracking was applied, centering the subband at a frequency corresponding to $V_{\rm LSRK} = 0$ km s^{-1}. This subband was sampled over 2048 channels, thus providing a velocity coverage and resolution of 108 and 0.052 km s^{-1}, respectively. Seven subbands of 128 MHz each were also observed in this 8-bit baseband, covering a total of 896 MHz for radio continuum. In addition, two basebands, centered at 23.45 and 25.45 were also observed with 3-bit samplers. Each of these basebands was covered by 16 subbands of 128 MHz. Therefore, the combined coverage for radio continuum data provided by the three observed basebands was 3.67 GHz, centered at 23.98 GHz.

Sources J0319+4130 (3C 84), J0137+331 (3C 48), and J0336+3218 (4C 32.14) were used to calibrate the spectral bandpass response, the absolute flux scale, and the complex gain (phase and amplitude), respectively. Calibration, imaging, and further processing was carried out with the Common Astronomy Software Applications (CASA) package. All maps were obtained with a Briggs weighting of visibilities (with robust=0.5 in task CLEAN of CASA), and deconvolved with the CLEAN algorithm. In the case of radio continuum emission, multifrequency synthesis was used to obtain the maps. The resulting FWHM of the synthesized beams were $3.4'' \times 3.1''$ (p.a. = 90°) for the water maser images, and $3.1'' \times 2.7''$ (p.a. = 79°) for the continuum images. The final images have been

---

[1] http://www.iram.fr/IRAMFR/GILDAS

Table 5.1: Observed positions.

Target name	R.A. (J2000)	Dec. (J2000)	rms (mJy)	Date	Type[a]	$L_{\rm bol}$ ($L_\odot$)	References
L1451-mm	03:25:10.25	+30:23:55.0	21	2015-SEP-29	FHC	0.05	1
L1448 IRS 2E	03:25:25.52	+30:45:02.5	16	2015-SEP-29	FHC	< 0.1	2
			14	2015-OCT-03			
Per-Bolo 58	03:29:25.40	+31:28:15.0	18	2015-OCT-01	FHC	0.18	3,4
B1-b field[b]	03:33:21.25	+31:07:35.0	19	2015-SEP-30	FHC	0.15–0.31	5,6,7
IC 348-SMM2E	03:43:57.73	+32:03:10.1	18	2015-SEP-30	BD-0	0.10	8
			20	2015-OCT-03			
IC 348-173	03:44:09.98	+32:04:05.4	18	2015-OCT-01	LL0-I	0.11	9
IC 348-613	03:44:26.90	+32:09:25.0	19	2015-SEP-30	BD-I	0.002	10,11,12
IC 348-205	03:44:29.54	+32:00:53.2	18	2015-OCT-02	LLO-I	0.08	9,13
IC 348-382	03:44:30.78	+32:02:42.9	27	2015-OCT-03	LLO-I	0.012	9,13
IC 348-165	03:44:35.43	+32:08:54.4	26	2015-OCT-03	LLO-I	0.10	9,13
SSTB213 J041726.38+273920.0	04:17:26.38	+27:39:20.0	18	2015-OCT-01	BD-I	< 0.002	14,15
SSTB213 J041740.32+282415.5	04:17:40.32	+28:24:15.5	17	2015-OCT-01	BD-I	< 0.003	14,15
SSTB213 J041757.77+274105.5	04:17:57.77	+27:41:05.0	17	2015-OCT-01	BD-I	< 0.004	14,15,16
SSTB213 J041828.08+274910.9	04:18:28.08	+27:49:10.9	18	2015-OCT-01	BD-I	< 0.001	14,15
SSTB213 J041836.33+271442.2	04:18:36.33	+27:14:42.2	18	2015-OCT-01	BD-I	< 0.003	14,15
SSTB213 J041847.84+274055.3	04:18:47.84	+27:40:55.3	17	2015-OCT-01	BD-I	< 0.004	14,15
KPNO-Tau 2	04:18:51.16	+28:14:33.2	17	2015-OCT-01	BD-II	–	13,17,18
IRAS 04158+2805	04:18:58.14	+28:12:23.5	21	2015-SEP-30	BD-I	0.4	19,20,21
SSTB213 J041913.10+274726.0	04:19:13.10	+27:47:26.0	16	2015-OCT-01	BD-I	< 0.002	14,15
SSTB213 J041938.77+282340.7	04:19:38.77	+28:23:40.7	19	2015-OCT-02	BD-I	< 0.006	14,15
IRAS 04166+2706	04:19:42.50	+27:13:40.0	27	2015-OCT-02	LLO-0	< 0.39	22,23,24,25
L1521D	04:21:03.55	+27:02:48.4	28	2015-OCT-03	LLO	0.3	26
SSTB213 J042019.20+280610.3	04:20:19.20	+28:06:10.3	18	2015-OCT-02	BD-I	< 0.002	14,15
SSTB213 J042118.43+280640.8	04:21:18.43	+28:06:40.8	18	2015-OCT-02	BD-I	< 0.002	14,15
IRAM 04191+1522	04:21:56.91	+15:29:45.9	20	2015-SEP-30	VeLLO-0	0.15	27,28,29,30
IRAS 04248+2612	04:27:57.33	+26:19:18.1	19	2015-SEP-30	BD-I	0.4	20
L1521F-IRS	04:28:38.95	+26:51:35.1	19	2015-OCT-02	VeLLO-0/I	< 0.07	30,31
MHO 5	04:32:16.00	+18:12:46.0	18	2015-SEP-30	LLO-I	0.066	9,13,32
IRAS 04325+2402 A/B	04:35:35.37	+24:08:19.5	18	2015-OCT-02	LLO-I	0.7	33,34,35,36,37
2MASS J04381486+2611399	04:38:14.86	+26:11:39.9	17	2015-SEP-30	BD-II	–	17,18,38
2MASS J04390396+2544264	04:39:03.96	+25:44:26.4	19	2015-SEP-30	BD-II	0.019	17,18,32
CFHT-BD-Tau 4	04:39:47.30	+26:01:39.0	19	2015-OCT-02	LLO-II	–	12,13,18,39,40
L1415-IRS	04:41:35.87	+54:19:11.7	18	2015-OCT-01	LLO-I	0.13	41,42
2MASS J04414825+2534304	04:41:48.25	+25:34:30.5	19	2015-SEP-30	BD-II	0.009	17,18,32
L1507A	04:42:38.59	+29:43:55.3	18	2015-OCT-02	LLO	< 0.3	26
2MASS J04442713+2512164	04:44:27.13	+25:12:16.4	19	2015-SEP-30	BD-II	0.028	18,43
IRAS 04489+3042	04:52:06.68	+30:47:17.5	17	2015-OCT-01	BD-I	0.3	19,20
CB130-1 field[c]	18:16:16.90	−02:32:38.0	25	2015-SEP-30	FHC	0.071-0.23	44
			24	2015-OCT-01			
L328-IRS	18:17:00.40	−18:01:52.0	24	2015-SEP-30	VeLLO-0	0.14	45,46
			19	2015-OCT-01			
L673-7-IRS	19:21:34.80	+11:21:23.0	15	2015-SEP-29	VeLLO-0	0.18	47,48,49
L1148-IRS	20:40:56.59	+67:23:05.3	14	2015-SEP-30	VeLLO-0	0.12	50
L1014-IRS	21:24:07.55	+49:59:09.0	21	2015-SEP-30	VeLLO-I/II	0.15	51,52
			17	2015-OCT-01			

Notes:
(a) Type of object. BD: (proto-)brown dwarf. FHC: First hydrostatic core. VeLLO: Very low luminosity object. LLO: Other low-luminosity YSO. The evolutionary class of the object is indicated by 0, I, II (for Class 0, I, and II objects, respectively).
(b) The B1-b field includes two candidate FHCs within the telescope beam: [HKM99] B1-bS and [HKM99] B1-bN (see Hirano et al. 1999).
(c) The CB130-1 field includes two candidate FHCs within the telescope beam: [KED2011] CB130-1-IRS1 and [KED2011] CB130-1-IRS2.
References.(1) Pineda et al. (2011); (2) Chen et al. (2010); (3) Enoch et al. (2010); (4) Dunham et al. (2011); (5) Pezzuto et al. (2012); (6) Huang & Hirano (2013); (7) Hirano & Liu (2014); (8) Palau et al. (2014); (9) Muzerolle et al. (2003); (10) Luhman (1999); (11) Preibisch & Zinnecker (2001); (12) Klein et al. (2003); (13) Mohanty et al. (2005); (14) Palau et al. (2012); (15) Morata et al. (2015); (16) Barrado et al. (2009); (17) Muzerolle et al. (2005); (18) Scholz & Jayawardhana (2006); (19) Motte & André (2001); (20) White & Hillenbrand (2004); (21) Andrews et al. (2008); (22) Shirley et al. (2000); (23) Young et al. (2003); (24) Tafalla et al. (2004); (25) Froebrich (2005); (26) Codella et al. (1997); (27) André et al. (1999); (28) Belloche et al. (2002); (29) Dunham et al. (2006); (30) Young et al. (2006); (31) Bourke et al. (2006); (32) Phan-Bao et al. (2011); (33) Ungerechts et al. (1982); (34) Hartmann et al. (1999); (35) Wang et al. (2001); (36) Güdel et al. (2007); (37) Scholz et al. (2010); (38) Luhman et al. (2007); (39) Martín et al. (2001); (40) Pascucci et al. (2003); (41) Stecklum et al. (2007a); (42) Stecklum et al. (2007b); (43) Bouy et al. (2008); (44) Kim et al. (2011); (45) Lee et al. (2009); (46) Lee et al. (2013b); (47) Kauffmann et al. (2008); (48) Dunham et al. (2010); (49) Schwarz et al. (2012); (50) Kauffmann et al. (2011); (51) Bourke et al. (2005); (52) Maheswar et al. (2011).

corrected by the primary beam response of the VLA. The absolute positional accuracy of our interferometric observations was $\simeq 0.3''$.

5.4 Results

In our single-dish observations, we only detected maser emission toward the position of L1448 IRS 2E (Fig. 5.1) on 2015 September 29. It only shows one clear spectral component of flux density 80 ± 30 mJy at $V_{\rm LSRK} = -2.3 \pm 0.3$ km s^{-1}. This source has been classified as a FHC by Chen et al. (2010).

However, our follow-up VLA observations shows that the maser emission is located at RA(J2000) = $03^h25^m22.348^s$, Dec(J2000) = $+30^\circ 45' 13.11''$. This position is $42''$ away from L1448 IRS 2E and is coincident with L1448 IRS 2 instead. The VLA spectrum is presented in Fig. 5.2. It shows a spectral component of flux density 460 ± 30 mJy at -1.19 ± 0.05 km s^{-1}. The peak velocity of the emission is redshifted by $\simeq 1.1$ km s^{-1} with respect to the peak measured in our single-dish spectrum. We think that the most likely situation is that the emission detected both with Effelsberg and the VLA arises from L1448 IRS 2. Assuming this is the case, we estimated the expected flux density in our single-dish observations, taking into account the FWHM of the Effelsberg beam ($39''$), and the distance between L1448 IRS 2 and our observed position ($42''$). For a source flux density of 460 mJy (Fig. 5.2), the flux density in the Effelsberg spectrum should have been $\simeq 18$ mJy. This is consistent with the non-detection on our second single-dish spectrum, taken on 2015-10-03 (Fig. 5.1). Our spectrum on 2015-09-29 is a factor of 4 brighter than our expectation, and it would indicate a decrease in the water maser emission over the time span of 15 days covered by our data. However, although unlikely, we cannot discard that L1448 IRS 2E (or other nearby source) was the emitting source of the spectrum in Fig. 5.1 and it faded over the following days. In any case, what is relevant for our work is that there is no confirmation that the FHC L1448 IRS 2E is a water-maser emitter. In these VLA observations, the 3σ upper limit for water maser emission toward L1448 IRS 2E is 14 mJy, after Hanning-smoothing the VLA data up to a velocity resolution of 0.21 km s^{-1}.

On the other hand L1448 IRS 2 is a Class 0 protostar with a luminosity $\simeq 3.6 - 5.2\ L_\odot$ (O'Linger et al. 1999; Tobin et al. 2015). Ours is the first reported detection of a water maser in this object. Furuya et al. (2003) and Sunada et al. (2007) reported non-detections toward this source, with 1σ rms levels of 80 and 170 mJy, respectively.

We detected two unresolved radio continuum sources with the VLA (Fig. 5.3), which correspond to sources VLA 3 and VLA 4 detected by Anglada & Rodríguez (2002) at 3.6 cm. We detected source VLA 3 (the northern one in the image) at RA(J2000) = $03^h25^m22.084^s$, Dec(J2000) = $+30^\circ 46' 05.46''$ with a flux density $S(23.98\mathrm{GHz}) = 0.43 \pm 0.05$ mJy. Its flux density is higher at lower frequencies (e.g., 0.89 ± 0.03 mJy at 3.6 cm, Anglada & Rodríguez 2002), confirming the presence of non-thermal emission, which suggests that this is a background source (Anglada & Rodríguez 2002), unrelated with this star-forming region.

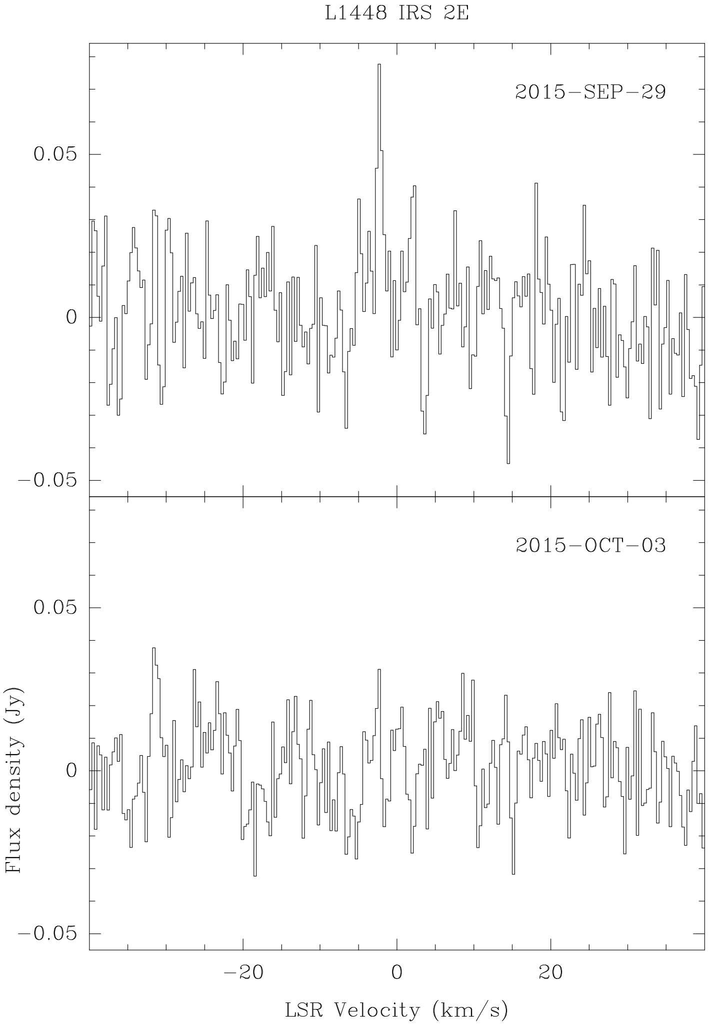

Figure 5.1: Water maser spectra towards the L1448 IRS 2E field obtained at the Effelsberg Radio Telescope.

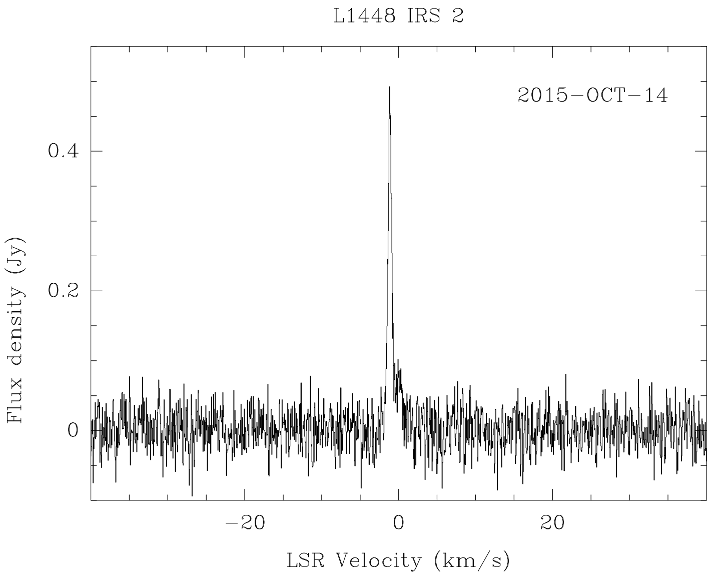

Figure 5.2: Water maser spectrum toward L1448 IRS 2, obtained with the VLA.

The southern source is located at RA(J2000) = $03^h25^m22.400^s$, Dec(J2000) = $+30°45'13.22''$ and it has a flux density S(23.98GHz) = 0.499 ± 0.018 mJy. This is source VLA 4 (0.34 ± 0.03 at 3.6 cm, Anglada & Rodríguez 2002), which is the radio counterpart of the infrared source L1448 IRS 2. Fig. 5.3 clearly shows that the water maser emission is associated with this radio source. Tobin et al. (2015) resolved the radio emission from L1448 IRS 2 into a binary, with a separation between components of $\simeq 0.751 \pm 0.004$ arcsec. We cannot resolve this binary in our radio continuum maps, but we note that the position of the maser emission is closer to component B. This is the weaker radio source of the two components, but it has a steeper radio spectral index, which would indicate that its free-free emission is optically thicker. It could be the younger of the two components and its association with water maser emission indicates that it is undergoing energetic mass-loss.

5.5 Discussion

We did not detect any water maser emission in our sample of low luminosity objects. This is in contrast with the high detection rates (∼ 40% in Class 0 YSOs, Furuya et al. 2001) in objects with higher masses. An important question is whether shocks related to mass-loss processes in these extremely low luminosity objects are energetic enough to produce water maser emission. The observations presented here are sensitive enough to impose significant constraints on our sample, to determine whether there is a lower limit on the stellar luminosity of sources capable to excite this type of emission.

Previous water maser surveys established an empirical relationship between the stellar

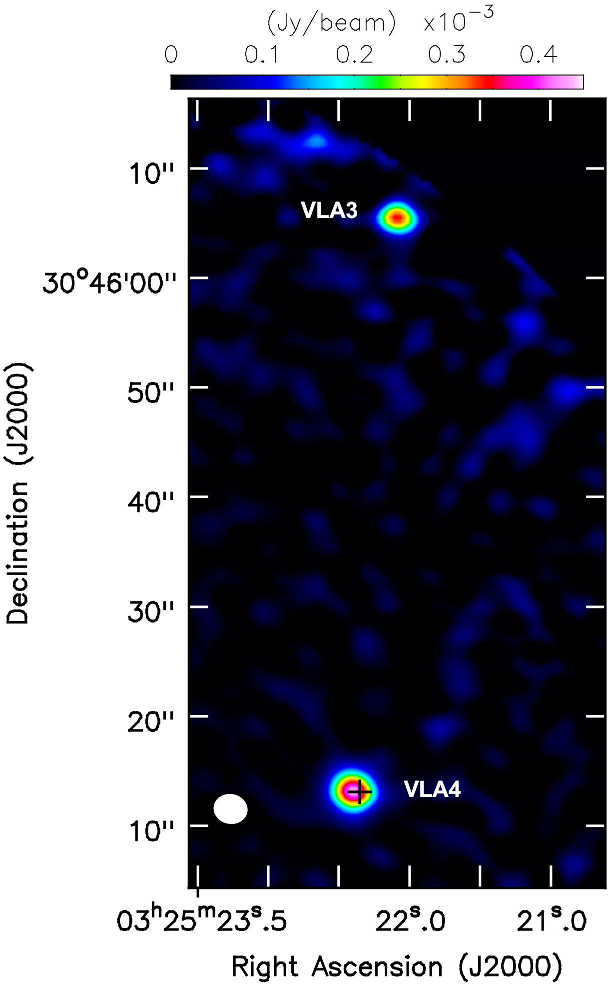

Figure 5.3: Image of the radio continuum sources at 1.25 cm in the L1448 IRS 2E field. The black cross near the southern source marks the position of the detected water maser. The white ellipse at the bottom left corner represents the FWHM of the synthesized beam of the continuum image. The detected sources are labeled following the nomenclature of Anglada & Rodríguez (2002).

luminosity and the water maser luminosity (e.g., Brand et al. 2003; Shirley et al. 2007). For instance, Shirley et al. (2007) give $L_{\mathrm{H_2O}} = 3 \times 10^{-9} L_{\mathrm{bol}}^{0.94}$. A correlation between the maximum velocity spread of the spectral components of the maser emission and the maser luminosity has also been found (Brand et al. 2003). Assuming a 3-σ upper limit to the flux density of the water maser emission in our sample of $\simeq 60$ mJy (since the rms was typically $\simeq 20$ mJy, Table 5.1), and an upper limit to the velocity spread of masers of $\simeq 1$ km s^{-1} (similar to that found in source GF9-2, with 0.3 $L_{\odot}$, Furuya et al. 2003), we obtain upper limits for the maser luminosity of our sample of 7×10^{-11} $L_{\odot}$ for sources in Perseus (assuming a distance of 232 pc, Hirota et al. 2011) and 3×10^{-11} $L_{\odot}$ for those in Taurus (distance 137 pc, Torres et al. 2007). Most of our sources are in those two complexes (those with right ascension between 3 and 5 hours).

If the empirical relationship by Shirley et al. (2007) stands for the sources in our sample, our observations should have enough sensitivity to detect water masers from sources with $L_{\mathrm{bol}} \gtrsim 10^{-2}$ $L_{\odot}$ in Perseus and Taurus. This is illustrated in Fig. 5.4, where we show the upper limits obtained in our observations for the water maser luminosity in FHC and Class-0 YSOs and BDs, together with the extrapolation to low luminosities of the empirical correlation by Shirley et al. (2007). We also show in this figure the upper limits to maser luminosity for other two sources with $L_{\mathrm{bol}} < 1$ L$_{\odot}$ (L1014-IRS and GF9-2; Shirley et al. 2007, Chapter 4.3.3 in this thesis). Although this empirical relationship has a large scatter, the upper limits in luminosity for all sources fall systematically below the empirical prediction by around one order of magnitude. The same happens with Class I and II sources in our sample, but we did not plot them in this figure because these more evolved objects have a much lower probability of pumping maser emission (Furuya et al. 2001).

If the empirical relationship between stellar and maser luminosities is still valid at $L_{\mathrm{bol}} < 1$ L$_{\odot}$ and the detection rates were similar to the ones found in other low-mass Class 0 protostars ($\simeq 40\%$), we should have detected some water masers. So either premise is not correct. The first possibility (that the empirical relationship between stellar and maser luminosities does not hold at the lowest end of the mass spectrum) would mean that the relationship is steeper for the lowest-luminosity objects, and the maser luminosities in objects < 1 L$_{\odot}$ are lower than predicted by the empirical relationship (see Fig. 5.4 in this chapter and Fig. 3 in Shirley et al. 2007). It is even possible that there is a strict threshold in luminosity below which, we cannot detect masers. The second possibility is that the relationship does stand at low luminosities, but the detection rates of masers are significantly lower than the values obtained in higher-luminosity Class 0 protostars, and even though the maser emission from these sources may eventually be above our detection threshold, it is excited during very short periods of time and we missed them. With our data it is not possible to discern between these possibilities. A further monitoring of these sources in our sample would help us to determine whether our failing to detect maser emission is due to a significant decrease of detection rates.

If a luminosity threshold exists, its value is still uncertain. As mentioned above, the lowest-luminosity object that has been reported to harbor a water maser is GF9-2 (L$_{\mathrm{bol}} \simeq 0.3$ L$_{\odot}$ Furuya et al. 2003). However, this detection was obtained with the

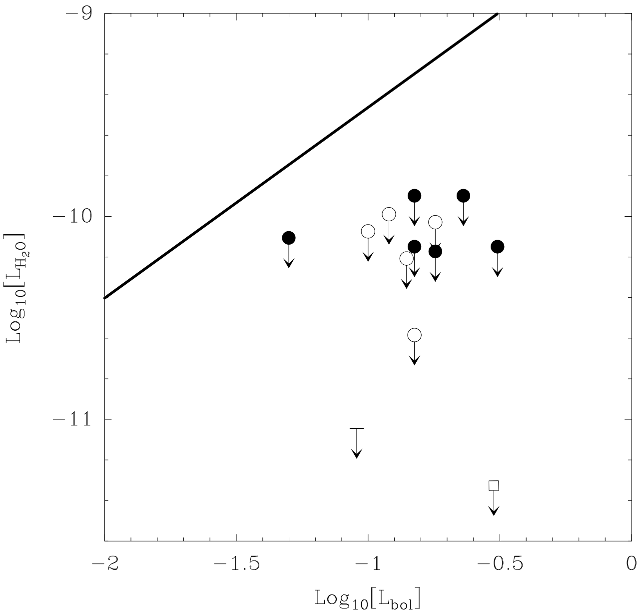

Figure 5.4: Upper limits of the logarithm of water maser luminosity in FHC and Class-0 objects in our sample, versus the logarithm of bolometric luminosities. The luminosities in both axes are measured in units of solar luminosities. Filled circles represent FHCs, and open circles represent Class-0 objects (both YSOs and BDs). We also plotted the upper limits for other two objects with $L_{\rm bol} < 1$ $L_\odot$: GF9-2 (open square; Chapter 4.3.3) and L1014-IRS (horizontal bar; Shirley et al. 2007), assuming a distance of 200 pc in both cases. The solid line represents the expected maser luminosities from the empirical relationship by Shirley et al. (2007). Sources with only upper limits to their bolometric luminosities in Table 5.1 are not included, since they would not constrain the luminosity relationship.

Nobeyama single-dish radio telescope in 2000 April, and has never been confirmed with interferometric observations. Our VLA observations (Chapter 4.3.3) failed to detect any water maser emission within $\simeq 1'$ of GF9-2, with a 3σ upper limit of 5 mJy, a factor ~ 75 lower than the flux density of reported by Furuya et al. (2003). Since the beam size of the Nobeyama telescope at 22 GHz ($75''$) is smaller than the VLA primary beam ($\simeq 2'$), we can be certain the emission detected in 2000 faded away by 2008. While it is certainly possible that GF9-2 was the water-maser emitting source in 2000, we cannot discard that the emission arose from another nearby source, as in the case of L1448 IRS 2E in this chapter. To our knowledge, the lowest luminosity YSO in which water maser emission has been confirmed with interferometric observations is VLA 1623 (Furuya et al. 2003), with a bolometric luminosity of $\simeq 1$ $L_\odot$.

5.6 Conclusions

We have carried out a sensitive single-dish survey (using the Effelsberg Radio Telescope) for water maser emission toward a sample of low-luminosity objects, comprising 20 young BDs, 7 FHCs, 6 VeLLOs, and 11 additional YSOs with $L_{\rm bol} < 0.4$ $L_\odot$ and/or $M < 0.15$ $M_\odot$. We only detected water maser emission when pointing towards L1448 IRS 2E, a FHC. However, follow-up interferometric observations with the VLA did not confirm the presence of water maser emission associated with this source. Instead, we found water maser emission associated with the Class-0 YSO L1448 IRS 2. This is the first reported detection of water maser emission toward this source.

If we extrapolate to low luminosities the known correlation between bolometric luminosity and water maser luminosities, established for sources with $L_{\rm bol} \geq 1$ $L_\odot$, we found that the expected water maser luminosities are one order of magnitude higher than the upper limits obtained in our survey for FHC and Class-0 objects. Possible explanations are that the $L_{\rm H_2O}$ vs $L_{\rm bol}$ relationship does not extend to the lower-end of the sub(stellar) mass spectrum (either its slope is steeper at low luminosities or there is a luminosity threshold below which water maser cannot be excited), or that the detection rates of water maser emission is lower than the values obtained for higher-luminosity Class 0 YSOs ($\simeq$40%).

Chapter 6

CCS emission in the active star forming region L1448

6.1 Introduction

The first stages of stellar evolution are characterized by energetic mass-loss phenomena. Specially in the case of low-mass YSOs, these phenomena manifest themselves as collimated jets and molecular outflows, while the object is still embedded in its parental molecular cloud (Bachiller 1996; van Dishoeck & Blake 1998). The energy injected by those jets and outflows affects the physical processes of the star forming regions, and produces changes in the chemistry of the molecular clouds (Bachiller & Perez Gutierrez 1997; Garay et al. 1998; Tafalla et al. 2010), also creating phenomena like maser emission (Seth et al. 2002).

The CCS molecule is classified as an early-type molecule, present in starless cores in gas phase, but its abundance quickly decreases in later phases, being very low in star forming regions. However, CCS has also been found in active star forming regions, such as B335 and L483 (Velusamy et al. 1995; Hirota et al. 2010). To study other regions in this stage of evolution, de Gregorio-Monsalvo et al. (2006) observed a sample of active star forming regions with single dish, and found some CCS-emitting regions containing class 0 YSOs. Follow-up interferometric observations towards the Class 0 source B1-IRS (De Gregorio-Monsalvo et al. 2005) showed for the first time that the CCS-NH_3 spatial anticorrelation stands at small scales ($\sim 5''$). These observations revealed a velocity pattern around a single YSO that suggested that CCS might be locally enhanced via shock-induced chemistry. These results would imply that the CCS production could be triggered not only during the first stages of molecular cloud evolution, but also at later stages, after the onset of the star formation.

L1448 is another active low-mass star forming region with CCS emission detected by de Gregorio-Monsalvo et al. (2006). L1448 is a dark cloud located at a distance of $\simeq 232$ pc in the Perseus cloud complex (e.g. Hirota et al. 2011). The total mass of the L1448 region was found to be $50-60$ $M_\odot$, from NH_3 (1,1) (Bachiller & Cernicharo 1986; Anglada et al. 1989) and CO data (Drabek-Maunder et al. 2016). The region has several centers of star formation activity. Here, we will focus on the region near the infrared source IRS3, which in its turn has two main centers of activity.

The first one, which we will refer to as the "L1448C" region, contains a well-known highly collimated outflow (shown in Fig. 6.1), powered by the source historically identified as L1448C or L1448C-mm (Curiel et al. 1990; Bachiller et al. 1990), a Class 0 YSO (Barsony et al. 1998) with a luminosity of 7.5 $L_\odot$ (Tobin et al. 2007). A second source, L144C(S) (possibly a Class 1 source), was identified $\simeq 8''$ south of L1448C (Jørgensen et al. 2006; Hirano et al. 2010; Lee et al. 2013a). Early observations found H_2O maser emission associated with L1448C (Chernin 1995; Claussen et al. 1996), with the maser spots aligned with the molecular outflow in this region (Chernin 1995; Hirota et al. 2011). The highly collimated CO outflow of the region (see Fig. 6.1) is centered on L1448C, and extends over $\sim 4.5'$, with the northern lobe blueshifted and the southern one redshifted. A narrow, extremely high-velocity jet-like component was found along the axes of the molecular outflow from L1448C, composed of a chain of emission knots that may be internal bow shocks identified in CO and SiO (Bachiller et al. 1995; Guilloteau et al. 1992; Dutrey et al. 1997; Girart & Acord 2001; Hirano et al. 2010). Some of the SiO knots are partially resolved along the transversal direction as seen in Fig. 6.2, where the component RII-a shows a morphology commonly found in bow shocks (Hirano et al. 2010). The momentum rate of the molecular jet is $\sim 5 \times 10^{-4}$ $\mathrm{M}_\odot$ km s^{-1} yr^{-1}, and it extends up to $\sim 20''$ from the central source (Hirano et al. 2010).

A less energetic CO(2-1) outflow is present in the region (Hirano et al. 2010), which is associated to the source L1448C(S) (Fig. 6.3), with momentum rate of $\sim 10^{-6}$ $\mathrm{M}_\odot$ km s^{-1} yr^{-1}. The outflow is compact, with the blueshifted lobe extending northeast, and the redshifted one southwest of L1448C(S). Given its position and proximity to the more energetic outflow, Hirano et al. suggest that the evolution of this second molecular outflow is affected by the high velocity outflow from L1448C.

Observations of high density tracers like ammonia (Anglada et al. 1989; Curiel et al. 1990) suggested interaction between the highly collimated wind and the ambient gas. Indeed, the spatio-kinematic distribution of ammonia in the L1448C region was interpreted as a disk-like structure, apparently rotating and contracting (Curiel et al. 1990). Moreover, the presence of a possible disk structure around L1448C has been suggested elsewhere (Yen et al. 2015; Tobin et al. 2015). Images of H_2 emission in the region showed knots in the northern side of the outflow (Davis et al. 1994; Eislöffel 2000; Curiel et al. 1999), but not in the southern side where NH_3 was detected, probably due to the inclination of the outflow's axis relative to the plane of the sky. In this scenario, the near-IR emission from the southern lobe, which would be in the background, would suffer a higher extinction by the dense envelope of molecular gas.

The second main activity center is more associated with the infrared source IRS 3. This region is sometimes referred to as L1448N. There are at least three sources in he region, that we will refer as IRS 3A, 3B and 3C[1], which are suggested to be class 0 sources (Barsony et al. 1998; Shirley et al. 2000; Kwon et al. 2006) and each seem to be associated

---

[1] An alternative nomenclature for these sources is L1448N A, L1448N B and L1448 NW respectively.

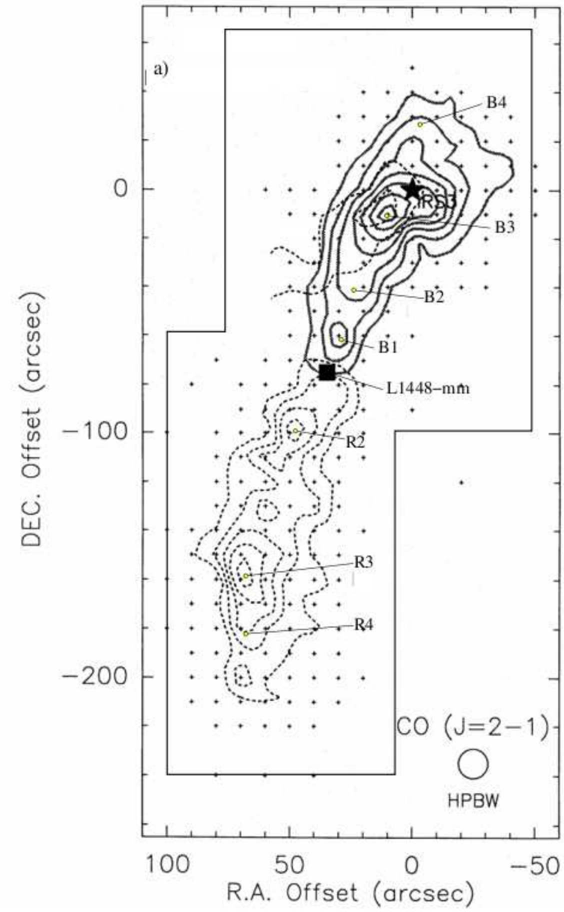

Figure 6.1: Integrated intensity map of CO $(2-1)$ high velocity outflow in L1448. (Map taken from Bachiller et al. 1990). Solid contours indicate blueshifted emission and dashed contours redshifted emission.

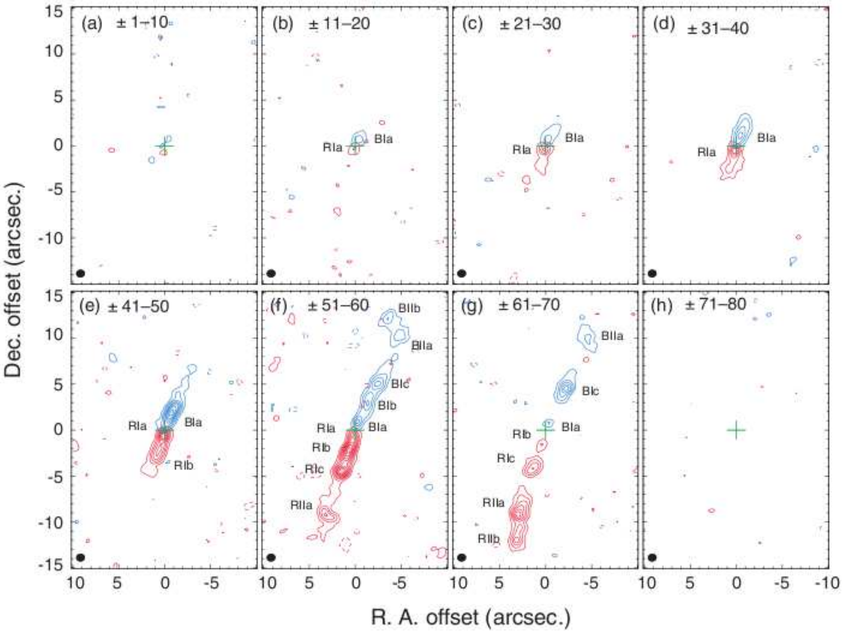

Figure 6.2: Maps of the SiO $J = 8 - 7$ emission of L1448C (Hirano et al. 2010), averaged over 10 km s^{-1} wide interval. The cross indicate the position of L1448C(N).

to molecular outflows (Fig. 6.4). These sources are near a peak of NH$_3$ emission, (Bachiller & Cernicharo 1986; Anglada et al. 1989), where maser water emission was also detected (Anglada et al. 1989). L1448 IRS 3B possibly have a disk of 100 AU radius, still embedded in an envelope (Yen et al. 2015). Indeed, (Tobin et al. 2015) suggested this source may have a massive, fragmenting inner envelope or disk. More recent observations showed that IRS3 B is composed by three sources and IRS 3C of two, making the whole IRS 3 system to be composed of a total of at least six sources (Tobin et al. 2016).

De Gregorio-Monsalvo et al. (2005) detected CCS toward both the L1448C and IRS 3 activity centers. Here we present interferometric observations of the CCS emission at 1.3 cm of these two regions.

6.2 Observations

We carried out observations of the $J_N = 2_1 - 1_0$ transition of the CCS line and the H$_2$O ($6_{16} \rightarrow 5_{23}$) maser transition (rest frequency 22344.033 MHz and 22235.08 MHz respectively) towards the L1448C and L1448 IRS3 regions, using VLA in its D configuration (project AG703). The region L1448C was observed in November 15 and 20, 2005 and the region L1448 IRS 3 in November 21 and December 14, 2005. We observed two fields, with phase centers located at R.A.(J2000) = $03^{\rm h}25^{\rm m}38.923^{\rm s}$ Dec (J2000)= $30^\circ44'05.26''$ for L1448C field and R.A. (J2000) = $03^{\rm h}25^{\rm m}36.48^{\rm s}$ Dec (J2000) = $30^\circ45'21.4''$ for the

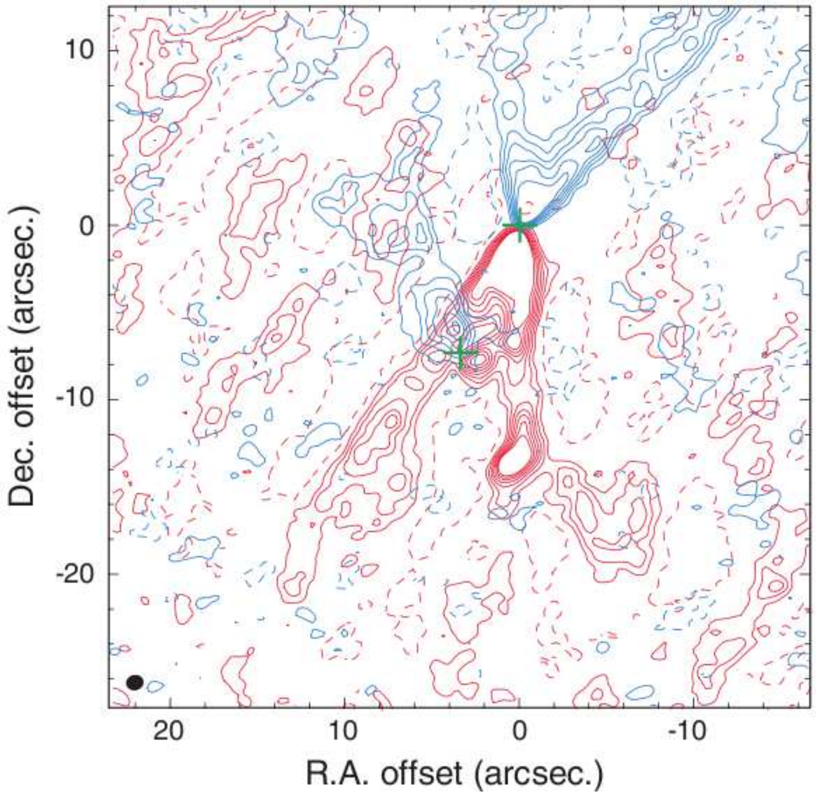

Figure 6.3: Map of CO $J = 3{-}2$ emission centered on L1448C(S), with coordinates relative to the source L1448C. The crosses indicate the positions of the two sources. Taken from Hirano et al. (2010).

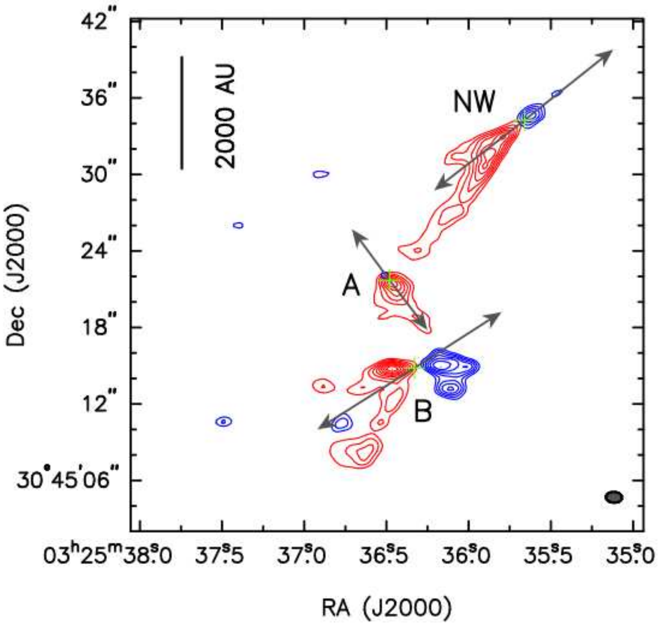

Figure 6.4: Integrated intensity maps of the outflows in the IRS 3 region from ^{12}CO$(2-1)$ data (Lee et al. 2015). The crosses indicate the positions of the sources IRS 3A, 3B and 3C.

L1448 IRS3 field. We observed in 4 IF spectral line mode, with 2 IF for each transition, allowing the simultaneous observations of the two spectral lines. For CCS we observed with a bandwidth of 0.78 MHz ($\simeq$ 10 km s^{-1}) centered at V_{LSR} = 4.5 km s^{-1} sampled over 127 channels which provide a spectral resolution of 6.1 kHz (0.08 km s^{-1}). For H_2O the bandwidth was 3.12 MHz sampled over 64 channels with channel width of 48.8 kHz (0.66 km s^{-1}) centered at 4.5 km s^{-1}.

We used the sources J0137+331, J0336+323 and J0319+415 as flux, phase and bandpass calibrators respectively. Calibration and data reduction were performed using AIPS.

One of the advantages of this spectral setup was the possibility of simultaneously observing the CCS thermal line and the H_2O maser emission. Since both lines are close in frequency (separation $\sim$ 109 MHz) the variations in phase and amplitude induced by the atmosphere are similar. Therefore, the H_2O maser data were self-calibrated, and the corrections found were applied to the CCS data. This cross-calibration using water maser emission to track atmospheric and instrumental errors has been successfully applied in the past to calibrate radio continuum data taken with the VLA (Reid & Menten 1990; Torrelles et al. 1996; Reid & Menten 1997), but, to our knowledge, this is one of the first times that cross-calibration is applied using a maser line to correct the data from a thermal line. It was attempted by De Gregorio-Monsalvo et al. (2005) in B1-IRS, but was unsuccessful due to the weakness of the maser line.

We obtained images of the continuum of the two regions, and performed continuum subtraction using AIPS task UVLIN. We made maps of CCS emission in each individual field, using robust weighting 5 (L1448C) and 3 (IRS 3), with a taper of 35 kλ in both cases. The resulting synthesized beams have sizes of $5.7'' \times 5.0''$ P.A. = 81.6 and $5.9'' \times 5.1''$ P.A.= 76.9 for L1448C and L1448-IRS3 fields. Since the primary beams of both fields overlap, we also generated a mosaic combining them, using the AIPS task FLATN, with a taper of 20 kλ with robust weighting 3, yielding a synthesized beam size of $8.4'' \times 7.5''$ P.A. = 72.3.

6.3 Results

6.3.1 Spatial distribution of CCS

The CCS emission shows a clumpy distribution in both observed regions of L1448. In the map of CCS integrated intensity in the IRS 3 region (Fig. 6.5) there is a chain of clumps tracing a stream morphology, located south of the IRS 3 central sources ($\sim 30''$ on the outflow axis), which extends along the NE-SW direction. A relatively strong clump (FWHM $\simeq 27'' \times 10''$) is located $\sim 30''$ west of IRS 3 sources, accompanied by other clumps of smaller size located elsewhere in the field. In the L1448C region, the integrated intensity map (Fig. 6.5, bottom) also shows part of the stream mentioned above, $\sim 45''$ north of L1448C, and it seems to bend to the south in the westernmost part. There is relatively strong emission south of L1448C, the brightest being a structure located $\simeq 35''$ of this source, which have two extensions towards the north. In addition, there is weak CCS emission (within $\sim 10''$) close to L1448C. The parameters of each of the identified clumps are shown in table 6.1.

In Fig. 6.6 we show the mosaic of the two fields of CCS integrated emission, overlaid on the NH_3 (1,1) map of Curiel et al. (1990) and a 3.6 μm IRAC Spitzer image (Tobin et al. 2007) that delineates the main bipolar outflow in the region. In this figure it is evident that the CCS and NH_3 emission are spatially anticorrelated, particularly in the L1448C region. Most remarkably, the NH_3 data shows extended emission associated with the source L1448C, while the CCS emission is distributed around it. The mosaic map of CCS clearly shows the stream of emission mentioned above, extending in the NE-SW direction, and located almost equidistant between the L1448C and IRS 3 sources. Its direction is nearly perpendicular to the molecular outflow from L1448C. Additional NH_3 emission is found in a wedge-like structure beyond the half-power primary beam (Curiel et al. 1990), so its exact morphology is difficult to ascertain.

We note that none of the CCS structure seen in these maps are located at the position of the IRS 3 sources. When comparing with other observations, we find that the main CCS structures of the IRS 3 region appear to be anticorrelated with those from tracers like $H^{13}CO$ and N^2H^+ (see Figs. 2 and 3 from Volgenau et al. 2006). While there is NH_3 emission in the IRS 3 region (Anglada et al. 1989; Bachiller et al. 1990), there is, however, no published interferometric data of that molecule that could provide high-resolution images of this area, to compare with our CCS map.

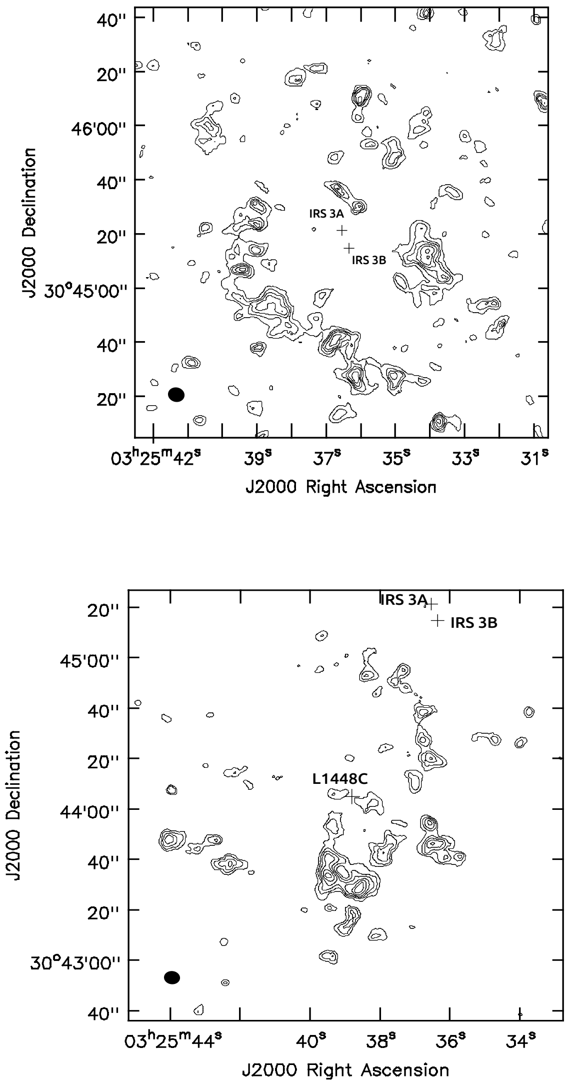

Figure 6.5: Integrated intensity map (zeroth-order moment) of the CCS ($J_N = 2_1 - 1_0$) transition in the regions L1448 IRS3 (top) and L1448C (bottom). In the IRS3 map, contours are 35, 50, 60, 70, 80 and 90% of the peak (2.0 mJy beam^{-1} km s^{-1}). In the L1448C map, first contour represents 40% of the peak, and the increment step is 10% (peak is 3.9 mJy beam^{-1} km s^{-1}). Crosses mark the position of sources IRS 3A, IRS 3B and L1448C. The beam is shown at the bottom left corner of each map.

Table 6.1: Physical parameters of CCS clumps in L1448.

Clump	I_ν mJy beam^{-1}	$\int I_\nu dv$ mJy beam^{-1} km s^{-1}	$N_{CCS}{}^{a}$ (10^{13} cm^{-2})	$N_{H_2}{}^{b}$ (10^{23} cm^{-2})	Size (AU × AU)	M ^{c} ($M_\odot$)
L1448C						
1	50.0	4.0	0.95	1.06	3016 × 2320	0.22
2	50.8	4.2	0.98	1.09	2635 × 1624	0.14
3	30.4	2.5	0.59	0.65	2552 × 1114	0.05
4	30.5	2.5	0.59	0.66	1462 × 1206	0.03
6	38.5	3.2	0.75	0.83	1578 × 858	0.03
7	41.6	3.4	0.80	0.90	2582 × 1600	0.10
8	37.5	3.1	0.72	0.81	2691 × 2134	0.14
9	37.0	3.0	0.72	0.80	1902 × 1663	0.07
11	28.5	2.3	0.55	0.61	1670 × 1183	0.04
12	32.2	2.6	0.62	0.70	1856 × 1508	0.06
13	32.2	2.6	0.62	0.70	1995 × 1021	0.04
14	34.4	2.8	0.70	0.74	1763 × 1090	0.04
15	28.5	2.3	0.55	0.61	1740 × 1067	0.03
L1448 IRS3						
1	21.5	1.80	0.42	0.46	2946 × 1610	0.06
2	17.7	1.45	0.34	0.38	2775 × 1956	0.06
3	22.2	1.82	0.43	0.48	2434 × 1833	0.06
4	20.9	1.71	0.40	0.45	2158 × 1675	0.05
5	22.1	1.81	0.43	0.48	1508 × 1334	0.03
6	22.8	1.87	0.44	0.50	1387 × 1220	0.02
7	22.9	1.88	0.45	0.50	1206 × 1012	0.02
8	18.4	1.50	0.36	0.40	2415 × 1090	0.03

[a] Column density obtained from $N_{CCS} = \frac{8\pi\nu^3}{c^3 A_{ji} g_j} \frac{Q(T_{rot}) \int I_\nu dv}{B_\nu(T_{ex}) - B_\nu(T_{bg})} \frac{e^{E_j/kT_{rot}}}{(e^{h\nu/kT_{ex}} - 1)}$ (considering the optically thin approximation) ν is the frequency of the transition, Q is the partition function, $\int I_\nu dv$ is the integrated intensity, E_j is the energy of the upper state (1.61 K; Wolkovitch et al. 1997), T_{rot} is the rotational temperature, g_j is the statistical weight of the upper rotational level, A_{ji} is the Einstein coefficient for the overall transition (4.33×10^{-7} S^{-1}). We assumed $T_{rot} = T_{ex} = 5$ K, $T_{bg} = 2.725$ K and $Q_{rot} = 23.8017$.

[b] Hydrogen column density, obtained assuming a fractional abundance with respect to H_2 of 0.9×10^{-10} for CCS (Lai & Crutcher 2000).

[c] We obtained the mass of each clump by integrating the N_{H_2} column density over the area given by its FWHM, assuming a distance of 232 pc (Hirota et al. 2011).

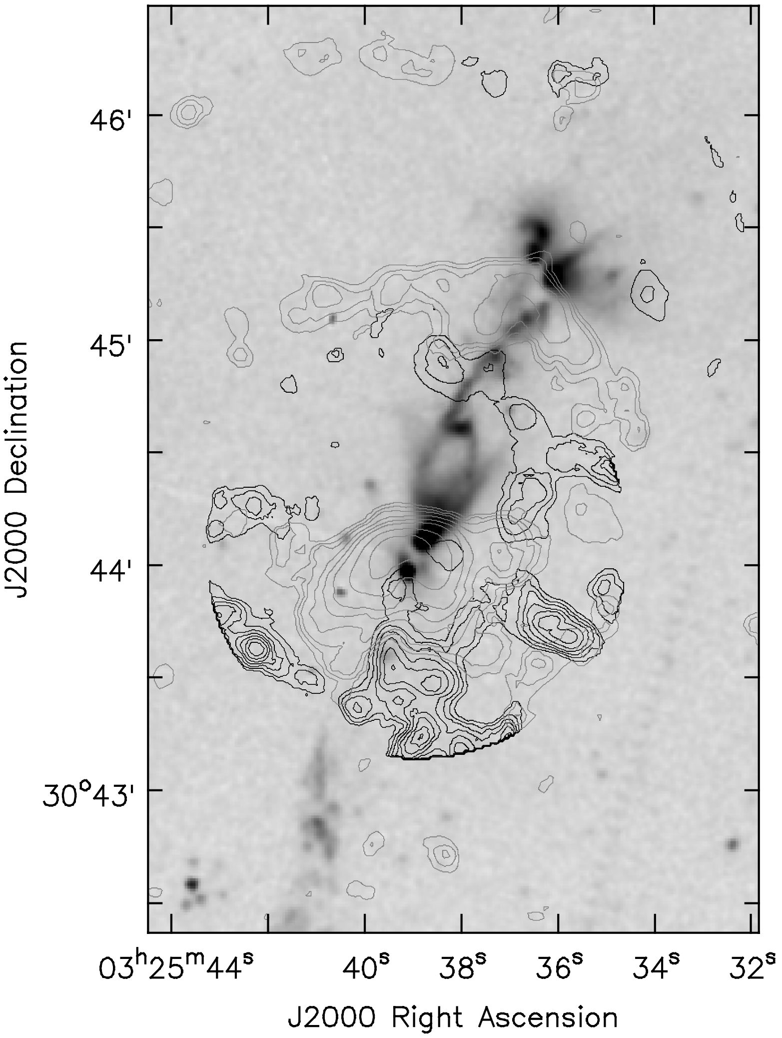

Figure 6.6: Overlay of the integrated emission of CCS (dark contours), NH_3 (1,1) (light contours; Curiel et al. 1990) and a Spitzer image of the L1448 region (black and white image, Tobin et al. 2007). The CCS first contour represents 28% of the peak emission (10.8 mJy beam^{-1} km s^{-1}), and the increment step is 10%. The NH_3 contours are 21, 28, 35, 49, 63, 77, 105 and 140 mJy beam^{-1} km s^{-1}.

6.3.2 Kinematics

In Figs. 6.7 and 6.8 we present our CCS integrated emission maps over four velocity intervals in each of the two fields. The maps of the IRS 3 region (Fig. 6.7) show that the most significant CCS structures of these maps are located at distances > 3000 UA ($> 10''$ in the maps) of the IRS 3 sources. The strongest structure found in the interval $4.3 - 3.9$ km s^{-1}, blueshifted with respect to the cloud velocity (4.5 km s^{-1}). The peak position of this clump is $\sim 25''$ from the IRS 3 B source, which is located almost in the direction of the blueshifted lobe of its outflow (as seen in Fig. 6.4). Having the same velocity shift, it is possible this clump could be interacting with the blue lobe of the outflow associated to source IRS 3 B.

For the L1448C region (Fig. 6.8), most of the strongest emission appears redshifted with respect to the cloud velocity. In the maps with the less redshifted velocities ($4.6 - 5.0$ km s^{-1} and $4.1 - 4.5$ km s^{-1}) there is CCS emission near L1448C, although none of the local peaks coincide in the position with either L1448C or L1448C(S).

In Fig. 6.9 (left) we present an overlay of the integrated intensity (moment 0, contours) and mean velocity (moment 1, colors) of the CCS emission. We note that for positions around the L1448C source, the velocity is close to that of the cloud. Towards the south of this source there is a velocity gradient, with velocities increasingly blueshifted from north to south. To compare with the ammonia data, Fig. 6.9 (right) shows the moment 1 of the ammonia emission (Curiel et al. 1990) together with our map of CCS moment 0. Note that, as mentioned by Curiel et al., the ammonia velocity systematically increases south of L1448C (more redshifted relative to the cloud velocity), which is the opposite trend as that traced by CCS (less redshifted). However, these gradients are in different spatial locations of the cloud.

This is clearly seen in Fig. 6.10, and 6.11 where we show position velocity diagrams taken along two directions passing through the position of L1448C field. The diagram along the N-S direction (Fig. 6.10), shows two different components: at positions closer than $20''$ from the source L1448C, the emission shows velocities close to the cloud velocity. However, farther to the south, there is a separate redshifted velocity component, with an internal velocity gradient (~ 25 km s^{-1} pc^{-1}), showing less redshifted velocities as we move away from the central source. The straight line in the figure shows the trend seen in the NH_3 position-velocity diagrams of Curiel et al. (1999), with a gradient of opposite sign. On the other hand, the Fig. 6.11, show that in the cut perpendicular to the jet axis there is a velocity gradient (~ 16 km s^{-1} pc^{-1}) with more redshifted gas as we move to the west. Along this direction, the kinematic trend is similar to the observed with NH_3, which was associated with rotation and contraction (Curiel et al. 1999).

In the CCS stream located between L1448C and IRS 3, we observe that the velocities oscillate around 5.0 km s^{-1} (Fig. 6.9, left), but the north-south extension at the south-west end of the stream is clearly more blueshifted. This extension may be showing interaction with the outflow of L1448C, given that is parallel to the blueshifted northern lobe of the latter. In the IRS 3 region, our map shows that the main structure located west of the IRS 3 sources is also blueshifted, as mentioned before.

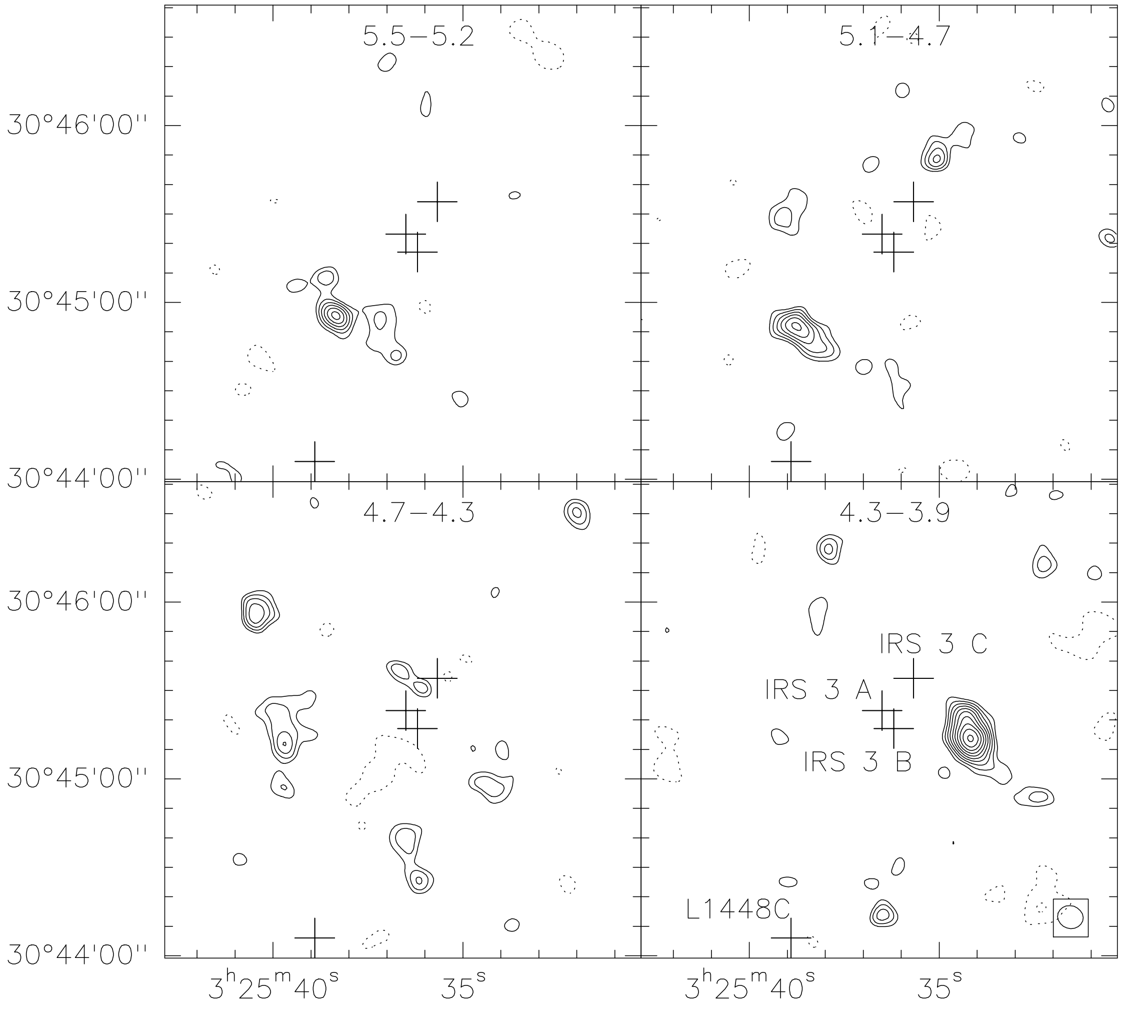

Figure 6.7: Integrated intensity of CCS emission in the IRS 3 region over different velocity ranges (shown at the top of each panel in km s^{-1}). Contours are -6, -3, 3, 4, 5, 6, 7, 8, 9 and 10 times 0.3 mJy $beam^{-1}$ km s^{-1} (the r.m.s. of our maps). The ellipse in the bottom right panel is the full width at half maximum of the synthesized beam. Crosses mark the position of sources IRS 3A, 3B, 3C and L1448C.

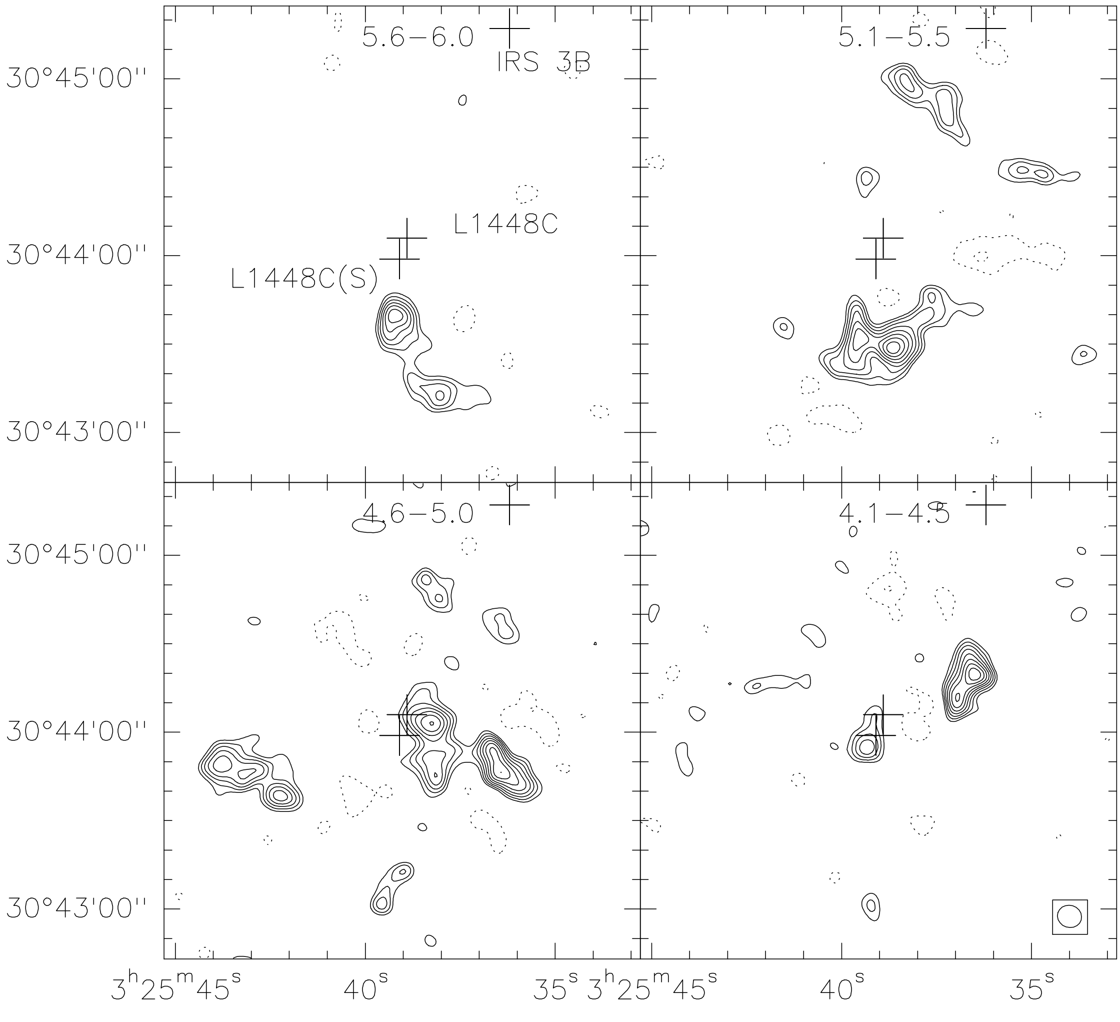

Figure 6.8: Integrated velocity channels for the CCS ($J_N = 2_1 - 1_0$) transition in the L1448C region. Each panel shows the integration velocity interval used (in km s^{-1}). The beam size is shown at the bottom right panel. Contours are -6, -3, 3, 4, 5, 6, 7, and 8 times 0.4 mJy beam^{-1} km s^{-1} (the r.m.s. of our maps). Crosses mark the position of sources IRS 3B, L1448C and L1448C(S).

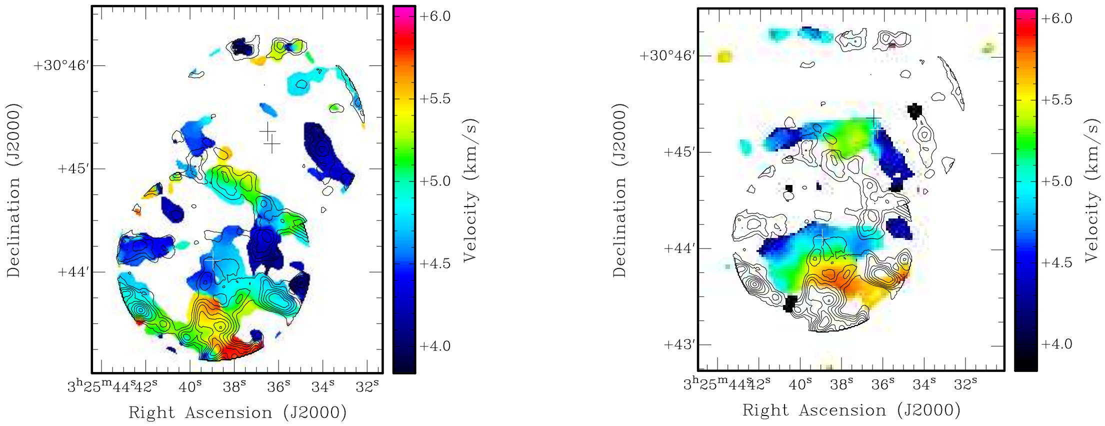

Figure 6.9: Left: overlay of moment 0 (contours) and moment 1 (color scale) of our CCS data. Right: moment 0 (contours) of CCS and moment 1 of the NH_3 (1,1) data of Curiel et al. (1990). Crosses mark the position of sources IRS 3A, IRS 3B and L1448C.

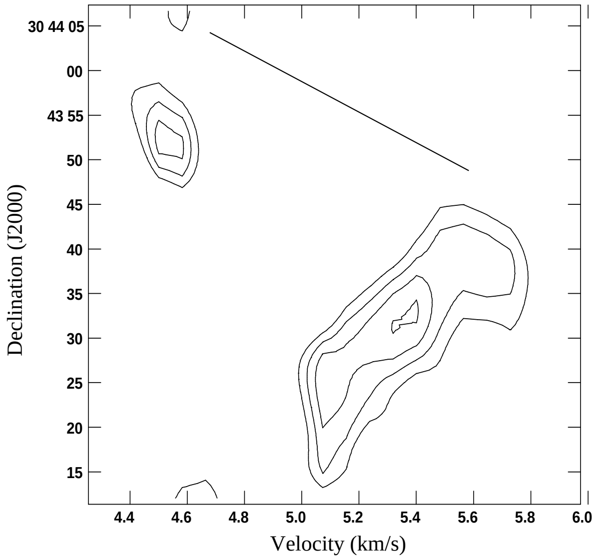

Figure 6.10: CCS position-velocity map for the L1448C field. The cut start on the L1448C position, towards the south. Axis are velocity and declination (J2000). The velocity of the cloud is 4.5 km s^{-1}. The line shows the velocity trend seen in the NH_3 position-velocity diagrams of Curiel et al. (1990).

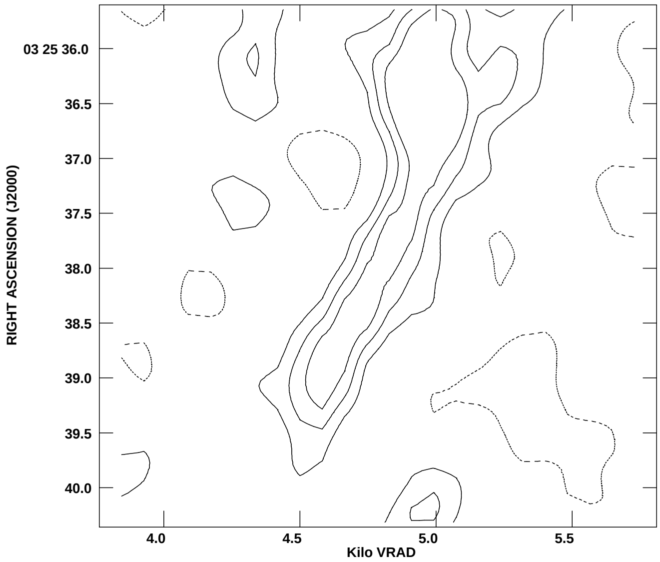

Figure 6.11: CCS position-velocity map of L1448C, cut perpendicular to outflow trajectory. Axis LSR velocity in km s^{-1}, and right ascension.

6.3.3 Physical parameters

We derived the physical parameters of the CCS clumps (see Table 6.1) in the two regions, considering the most intense structures present in our maps without primary beam correction. With our CCS data, we found that a total mass of $\sim$ 1 $M_{\odot}$ and $\sim$ 0.3 $M_{\odot}$ for the L1448C and IRS 3 regions, respectively.

The total mass obtained for L1448C by Curiel et al. (1999) from their ammonia data is 1.5 $M_{\odot}$ which is also similar to the result found by Motte & André (2001) (1.5 $M_{\odot}$) derived from dust emission. Taking into account that the CCS and NH_3 emission is mostly spatially anticorrelated, and thus traces different areas, we estimate a total mass content in the L1448C region as the sum of the estimates from both molecules, yielding $\simeq$ 2.5 $M_{\odot}$.

To estimate the missing flux in our interferometric maps, we measured the integrated flux of our map in an area of the same size as the single dish beam of the Robledo 70m antenna used in the observations of De Gregorio-Monsalvo et al. (2005). We found that $\simeq$ 50% of the CCS flux is missed by the VLA in L1448C. If we consider the missing flux in the observations of CCS and NH_3, we may argue that the the total mass of L1448C may represent $5 - 10$% of the total mass in L1448, estimated to be $\simeq 50 - 60$ $M_{\odot}$ (Bachiller & Cernicharo 1986; Anglada et al. 1989).

6.4 Discussion

6.4.1 Anticorrelation and complementarity of molecular species

L1448 is a star-forming region comprising multiple current activity centers. As mentioned before in this thesis, the CCS molecule is believed to be a tracer of early-time chemistry, while ammonia is prominent in more evolved stages of cloud evolution (Hirahara et al. 1992; Velusamy et al. 1995). In this framework, CCS abundance (and thus, its molecular line emission) would decrease with time, while that of ammonia would increase. However, single-dish observations by our group show that this molecule is abundant abundant in the active regions L1448C and L1448 IRS3 (de Gregorio-Monsalvo et al. 2006), suggesting that the molecule could be regenerated, as in the case of B1-IRS (De Gregorio-Monsalvo et al. 2005).

In our maps, the CCS clumps appear spatially anticorrelated with NH_3 at scales of $\simeq 5''$. This is most clearly seen in the L1448C region, where CCS clumps surround the NH_3 structure. This indicate that the CCS molecules are highly depleted up to distances of $\simeq$ 5000 UA ($\simeq 20''$) from the central source, which is the approximate size of the region traced by NH_3. Some of the CCS clumps found in our maps appears might be residual emission from the original CCS content in the cloud where the stars were born. Nonetheless, other areas, most remarkably the strong CCS emission south of L1448C, may have a different chemical behavior, with CCS abundance being re-enhanced by the mass-loss processes in the region. In fact, CCS emission in L1448C seems to be stronger in dense gas whose kinematics can be associated with the molecular outflow.

For instance, the main clump of CCS emission (located south of L1448C) has a location and velocity sign that are consistent with the redshifted lobe of the collimated CO and SiO outflows associated with this source (Bachiller et al. 1990; Guilloteau et al. 1992), which extend south of the central source. Furthermore, an extension of redshifted CCS emission and another relatively intense clump southeast of L1448C may be related to the second molecular outflow of the region (Hirano et al. 2010), which is probably excited by source L1448C(S). Indeed, while the NH_3 (1,1) emission detected by Curiel et al. (1990) shows a general north-south velocity gradient, with more redshifted velocities as one moves to at the south, it also shows a NE-SW gradient. The latter was also found in the gas within $15''$ L1448C (Yen et al. 2015), using $C^{18}O$ $(2-1)$ observations. The direction of these gradients are similar to the direction of the CO outflow of L1448C(S) (Hirano et al. 2010), which suggests interaction of this outflow with the ambient gas.

Moreover, the position-velocity diagram of Fig. 6.10 shows that at distances $20''-1'$ south of L1448C, the redshifted dense gas shows a velocity gradient in CCS, with less redshifted at increasing distance from L1448C, indicative of deceleration, which is also seen in the CO outflow at large scales (Bachiller et al. 1990). Interestingly, the NH_3 emission shows also redshifted emission in the inner regions ($< 20''$) of L1448C. but with an opposite gradient, showing acceleration (~ 8 km s^{-1} pc^{-1}), as illustrated by the straight line on Fig. 6.10. This acceleration pattern is consistent with the acceleration observed in the compact SiO outflow in the region (Curiel et al. 1999; Guilloteau et al. 1992).

Given the spatial anticorrelation between NH_3 and CCS, each line is tracing gas that is invisible for the other, which clearly shows the importance of multiple molecular tracers to completely trace the gas content and kinematics of a star-forming region, since using one of them necessarily imposes a bias.

This gradient turnover may be explained due to interaction of the outflow with the ambient gas, given that deceleration begins approximately where the collimated jet ends and the outflow axis appears to change direction. The stronger clumps south of L1448C region are located in the area where the red lobe show a change of its trajectory (see for example Wolf-Chase et al. 2000). All these results suggest that the CCS abundance may be enhanced in the region L1448C by the interaction of the outflow with the ambient gas.

Regarding the IRS 3 region, its CCS emission does not seem to be significantly enhanced, despite the presence of multiple protostar and outflows in the region. In fact, the column density in the CCS clumps around L1448C is higher than that of the IRS3 region, which already was suggested in the single dish spectra of de Gregorio-Monsalvo et al. (2006). This may indicate that the regeneration of the gas-phase CCS molecule could be more efficient around L1448C, probably because its outflow is more energetic than the ones in the IRS3 region. Only the blueshifted clump ($\sim 25''$ west of the source), in the direction of the blue lobe of the outflow from source IRS 3B (see Fig. 6.4) shows signs of interaction with a mass-loss process.

Finally, we suggest that the weak stream of CCS emission between the L1448C and L1448 IRS 3 sources could be the remnant of the original CCS emission from the pre-stellar phase, which tends to disappear from the areas closer to the sources (See section 4.2). Alternatively, it is possible that this structure is the result of an abundance enhancement due to the interaction between the blueshifted lobe of the outflow from L1448C and the ambient molecular gas. Interaction between this lobe and the ambient gas was suggested as the origin of the NH_3 arc-like structure found by Curiel et al. (1999) near the IRS 3 sources (Fig. 6.6), which is nearly parallel to the CCS stream. However, we did not find any significant kinematic evidence to support this interaction, except for the westernmost area, where the stream bend to the south in a direction parallel to the blueshifted lobe of the CO outflow, and it is also blueshifted.

6.4.2 Regeneration of CCS in active star forming regions

Our results suggest that CCS abundance may be enhanced in the active star forming region L1448C, due to interaction of the outflow with the ambient gas. A possible mechanism to increase the CCS abundance (after the period of efficient CCS production in prestellar clouds ended) is the desorption of the molecule from grain mantles, which is due to heating and shocks produced by mass-loss processes once star-formation begins. An example of this mechanism was found in the active star forming region L1157, where carbon-chain molecules like CCS and CCH have been detected in a shocked area (Yamaguchi et al. 2012), which suggests that these molecules go to gas phase by grain-mantle evaporation. In L1448C this mechanism may take place to form the CCS clumps in the region of interaction south of L1448C (where the bending of the outflow trajectory takes place), in the most blueshifted segment of the stream, and also in the weak CCS structures around the L1448C sources.

Other mechanisms can create the CCS molecule in gas phase, for example the desorption of molecules from grains and dissociation of different molecules that, once in gas phase, could react to produce CCS molecules again. This possible mechanism for regeneration of carbon-chain molecules due to the star formation processes is known as the "warm carbon-chain chemistry" (WCCC). This would take place in the warm ($\sim$ 25 K) and dense region near the protostar. Carbon-chain species could be generated in the protostellar core by combination of gas-phase and grain-surface reactions (Sakai et al. 2008). As we found that the CCS emission is also present in areas relatively close to L1448C ($\sim$ 5000 AU), this may imply that the WCCC processes could be significant in those inner areas.

In this scenario, CCS may remain deficient if sulfur is still depleted on dust grains (Sakai et al. 2008). Interestingly, the main sulfur species in dense regions of interstellar medium are still unknown (Bilalbegović & Baranović 2015). While molecules like OCS and SO_2 have been detected on ice mantles (Boogert et al. 1997), their estimated abundances are only a few percent of the cosmic S abundance. The detection of molecules like CCS in active star forming regions may suggest that this molecule could be part of the sulfur reserves.

6.5 Conclusions

We have carried out interferometric CCS observations of two active star-forming regions in the L1448 cloud, where previous single-dish spectra showed significant emission of this molecule. Our main results are summarized as follows:

- We confirmed the spatial anticorrelation between CCS and NH_3 in the regions L1448C and L1448 IRS3.
- In the case of the L1448C, besides tracing different areas, the velocity gradients are different south of the protostar, with an accelerating pattern close to the source (traced by NH_3) and deceleration in the outer areas (traced by CCS). This shows the importance of using different molecular tracers to obtain a complete picture of the gas content and kinematic in a molecular cloud. Either individual molecule may provide an insufficient picture.
- Some of the CCS clumps appear to be remnant of the original CCS cloud. However, other clumps are located at positions where interaction between the outflow and the ambient gas may be occurring. This suggests that the gas-phase CCS molecules can be produced at a relative advanced stage of the star formation process, and not only during the prestellar phase.
- The CCS emission does not seem to be significantly enhanced in the L1448 IRS3 region, probably because its outflows are less energetic than that from L1448C.

- To regenerate CCS molecules in this region, we consider as possible processes like warm carbon-chain chemistry or desorption of the molecules from dust grains.

Chapter 7

A dust jet and a Keplerian disk around the Class-0 protostar L1448C

7.1 Introduction

Circumstellar (protoplanetary) disks and collimated jets in young stellar objects (YSOs) are intimately related structures, and key ingredients in the process of star formation. The gravitational collapse of a clump within a molecular cloud naturally gives rise to a protostar surrounded by a protoplanetary disk, with the latter holding most of the residual angular momentum of the original clump. Releasing angular momentum is a necessary step in order to the disk material to fall onto the protostar, so that it can continue growing its mass. Collimated jets, ubiquitously found associated to YSOs, are believed to be a key agent in this angular momentum release from the disk material. Recent reviews on jets and their relationship with circumstellar disks can be found, for instance, in Frank et al. (2014), Bally (2016), and Anglada et al. (2018).

Jets from YSOs can be imaged with a plethora of tracers, such as forbidden lines (at visible and infrared wavelenghts; see e.g., Reipurth et al. 2002), shocked H_2 emission (infrared; Makin & Froebrich 2018), rotational molecular lines (millimeter/submillimeter; Zapata et al. 2010), or radio continuum emission (Carrasco-González et al. 2010). These tracers evince the gas content of jets, whether in ionized, atomic or molecular state. However, considering that dust is found alongside gas in molecular clouds, it is to be expected that dust could also be a constituent of the jet material, although its detection has been far more elusive. The study of dust in jets is important, since it can reveal key clues on the origin of mass-loss. While dust along the jet body can be entrained material from the environment, tracing it closer to the central YSO may indicate that dust is an intrinsic part of the jet from its launching point, thus tracing the original wind ripped off from the circumstellar disk.

Reiter et al. (2017) have recently reported the detection of a dusty jet in HH 1019, observed silhouetted against the background in the optical. This is probably the best direct evidence of dust in a jet, strongly suggesting the ejection of a dusty disk wind. As discussed by these authors, several previous works indirectly deduced the presence of dust in jets (e.g. Agra-Amboage et al. 2011; Podio et al. 2011). Moreover, millimeter/submillimeter dust emission has been detected along jets (e.g. Chini et al. 2001; Gueth et al. 2003), although it has not been not possible to ascertain whether this dust was originally part of the disk, or it is just environmental material entrained by the jet. Since optical obscuration precluded Reiter et al. (2017) to trace the dusty jet in HH 1019 up to the central star, it was not possible to determine its origin and therefore, entrainment cannot be completely ruled out.

In this paper, we present millimeter observations of L1448C, clearly showing a dusty jet emerging from a protoplanetary disk. L1448C (Curiel et al. 1990; Bachiller et al. 1991) is a paradigmatic example of a class 0 protostar, the first stage of protostellar evolution (André et al. 1993). This source is the powering source of an energetic, highly collimated jet/outflow, whose gas component is traced, for instance, by molecular rotational lines (Bachiller et al. 1995; Girart & Acord 2001; Hirano et al. 2010), shocked H_2 (Bally et al. 1993; Davis et al. 1994), water masers (Chernin 1995; Hirota et al. 2011), atomic forbiden lines (Dionatos et al. 2009), and radiocontinuum emission from shock-ionized gas (Curiel et al. 1990). A distance estimate of 232 ± 18 pc has been obtained by parallax measurements using Very Long Baseline Interferometry observations of the water masers associated to the source (Hirota et al. 2011). We will use this distance in our calculations. Note, however, that Ortiz-León et al. (2018) recently questioned the reliability of that distance. They proposed a value of 293 ± 22 pc for the nearby cloud NGC 1333 in Perseus, for which Hirota et al. (2008) had obtained 235 ± 18 pc. Assuming that distance (293 pc) for L1448C would increase all calculated masses by a factor of $(293/232)^2 = 1.6$.

7.2 Observations

We used archival ALMA observations at 1.3 mm, carried out on 2014 August 28 for project 2012.1.00647.S. The spectral set-up consisted in four spectral windows. Two of them, intended for continuum data, had a bandwidth of 2 GHz each, sampled over 128 channels, and centered at 218 and 233 GHz. The other two, aimed at spectral line data, had bandwidths of 234.375 MHz sampled over 3840 channels, and were centered at rest frequencies 219.56036 and 231.32186 GHz. The continuum maps presented in this paper were obtained from the two spectral windows of 2 GHz bandwidth and the line-free channels in the other two spectral windows, so the final central frequency is 225.4648 GHz. We also present spectral line data of the $C^{18}O$(2-1) transition from the spectral window centered at the rest frequency of this line (219.56036 GHz), with a spectral resolution of 61.03 kHz (0.08 km s^{-1}). Velocities in this paper are given with respect to the kinematical definition of the Local Standard of Rest (LSR).

The phase center of the observations was set at R.A.(J2000) = $03^h25^m38.8^s$, Dec(J2000) = $+30°44'05''$. The source J0237+2848 was used to calibrate the bandpass, complex gains, and flux density scale. The initial calibration was carried out by ALMA staff with version 4.2.2 of the Common Astronomy Software Applications (CASA) package. Version 4.6.0 of CASA was used for further processing and imaging.

We performed phase-only self-calibration on the continuum visibilities, and the obtained solutions were interpolated in frequency and applied to the spectral line data. Maps were obtained with Brigg's weighting, applying a robust parameter 0.5 (as defined in task CLEAN of CASA), unless stated otherwise. Images were deconvolved with the CLEAN algorithm. Continuum emission was subtracted from the visibilities before obtaining the data cube of line emission. The maps presented in the paper have been corrected by the primary beam response of the ALMA antennas.

7.3 Results

We detected both continuum and $C^{18}O$(2-1) line emission toward L1448C. The continuum emission (Fig. 7.1) peaks at R.A.(J2000) $= 03^h25^m38.875^s$, Dec(J2000) $= +30^\circ44'05.27''$ (the astrometric accuracy of these data is $\simeq 40$ mas) with a flux density 173.4 ± 1.0 mJy. Two structures are evident in the image. The brightest one is elongated morphology in the NE-SW direction, with a flux density 158.6 ± 0.3 mJy. Its orientation is nearly perpendicular to the outflow processes in the region, which suggests that the continuum emission is tracing dust related to a circumstellar disk. The flux density for this central structure is consistent with the value obtained by Tobin et al. (2015) at 225.05 GHz, $S_\nu \simeq 160.4$ mJy (from observations with an angular resolution $\simeq 0.5''$). We obtained dust masses assuming optically thin emission, from the formula

$$M_{\rm dust} = \frac{S_\nu d^2}{\kappa_\nu B_\nu(T)} \, , \tag{7.1}$$

where S_ν is the flux density, d is the distance to the source, κ_ν is the opacity coefficient per unit dust mass, and $B_\nu(T)$ is the Planck function at temperature T. Assuming an opacity coefficient at 1.3 cm $\kappa_\nu = 0.9$ cm^2 g^{-1} (appropriate for the protostellar phase, Ossenkopf & Henning 1994). Therefore, for a temperature of 20 K (typical for circumstellar disks, Andrews & Williams 2005), we obtain a dust mass for the disk-like structure of 670 $M_\oplus$. Assuming a gas-to-dust ratio of 100, the total mass would be $\simeq 0.2$ $M_\odot$. This is probably an underestimate of the total mass, since the optically-thin approximation may not be appropriate for the brightest emission close to the center.

The second structure is a jet-like feature perpendicular to the major axis of the brightest central disk-like emission. The extension to the NW, up to $\simeq 3''$ (650 au) from the emission peak and reaching up to $\simeq 10\sigma$ is a robust detection. A weaker southeast counterpart is also detected. There are several blobs at a $\simeq 5\sigma$ level, distributed to the NW on a roughly in the same direction along a string up to $12''$ (2800 au) from the central source. We believe this string of blobs is also real, since there is no feature in the synthesized beam with that orientation. The northernmost structure in the image, elongated E-W, is most likely spurious, since there are dirty beam sidelobes with that orientation, and there is a similar feature to the south and at the same distance from the central source. We

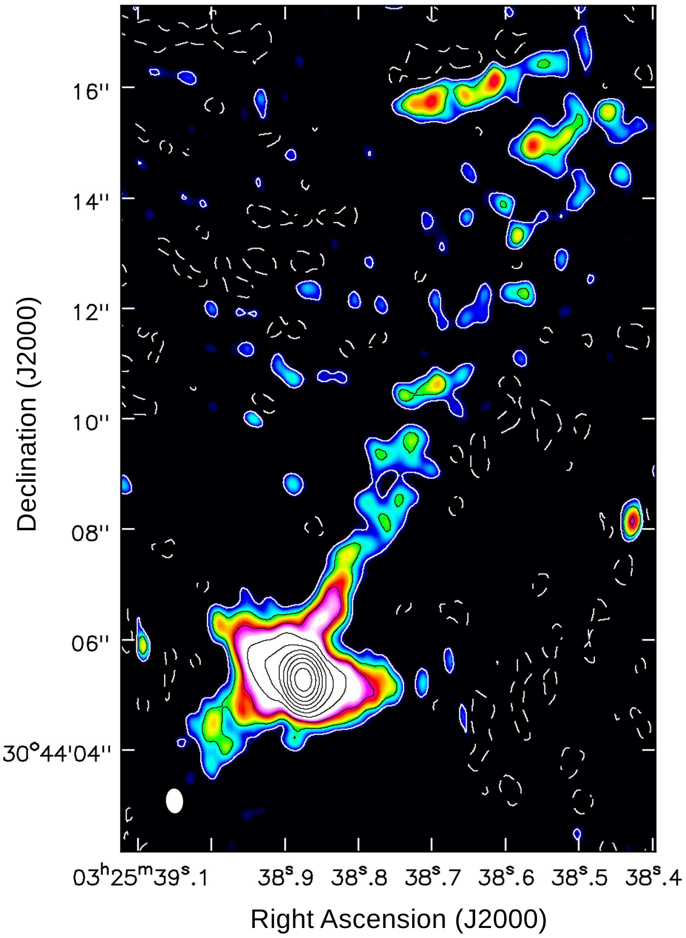

Figure 7.1: Continuum emission at 225.5 GHz in L1448C. White and black contour levels are -2, and 2^n times 60 μJy beam^{-1} (the rms of the map), with n=1 to 10. The ellipse at the bottom left corner represents the synthesized beam, with full width at half maximum $0.43'' \times 0.28''$, P.A. = 3.8°

estimate flux densities 12.9 ± 0.7 and 1.86 ± 0.22 mJy for the NW (including the weaker blobs) and SE lobes, respectively. The collimated appearance of this continuum emission, and its orientation similar to other outflow tracers in the region, suggest that it is tracing dust in a jet. The position angle of the NW jet is $\simeq -35^\circ$ near the star and changes to $\simeq -15^\circ$ at distances $\simeq 1.5'' - 3''$ away from it. Beyond this brightest jet-like extension, the string of weaker blobs have a general position angle $\simeq -26^\circ$. We note that the position angle at the base of the jet is very close to that of the proper motions of water masers, at scales $\lesssim 60$ mas (P.A. = -34°, Hirota et al. 2011), while the orientation of the string of weak continuum blobs is closer to that of the large-scale molecular outflow (P.A. = -21°, Bachiller et al. 1995). We obtained dust masses of 1.2 and 0.2 $M_\oplus$ for the NW and SE jet lobes, respectively, assuming a jet temperature of 700 K (appropriate for a jet from a Class-0 object; Flower et al. 1985; Dionatos et al. 2009; Panoglou et al. 2012).

The velocity-integrated $C^{18}O$ emission shows an elongated morphology, with two main peaks separated by $\simeq 0.6'' = 140$ au (Fig. 7.2). The peak of the continuum emission is located exactly midway between both $C^{18}O$ local maxima. The major axis of the $C^{18}O$ structure is oriented at a position angle $\simeq 60^\circ$, which is similar to that of the main axis of the central continuum emission and nearly perpendicular to the innermost jet-like feature also seen in continuum. The velocity-integrated flux density of the line emission is 1.673 ± 0.024 Jy km s^{-1}. Assuming local thermodynamic equilibrium with a kinetic temperature of $\simeq 20$ K, and optically thin emission, this implies total gas mass $M(H_2) \simeq 0.003$ $M_\odot$ for a molecular abundance $CO/H_2 = 10^{-4}$ and a solar isotopic abundance $^{16}O/^{18}O = 489.5$. This is two orders of magnitude lower than the disk mass obtained from the continuum emission (under the assumption of a gas. -to-dust ratio of 100). A significantly lower gas-to-dust ratio and/or a higher $C^{18}O$ abundance may partly explain this discrepancy. It is also possible that a fraction of the disk-like structure seen in the continuum is part of a flattened envelope that has not jet fallen onto the disk traced by $C^{18}O$. However, we believe that the gas mass may be grossly underestimated from the $C^{18}O$ data. This is because the dust emission becomes optically thick in the inner part of the disk (see, e.g., Gómez & D'Alessio 2000). In that case, no line emission can be detected, even in the presence of a large amount of gas. Thus, it seems that most of the $C^{18}O$ line misses most of the disk mass, located at those central regions.

Fig. 7.2 also shows a position-velocity (PV) diagram along the major axis of the $C^{18}O$ structure (position angle 60°). It clearly shows the signature of a rotating Keplerian disk, extending up to at least a radius $\simeq 2''$ (460 au), and with the SW and NE halves being red and blueshifted, respectively. The line is seen in absorption toward the center, as expected in the inner parts of a circumstellar disk (Gómez & D'Alessio 2000). The velocity of this local minimum, which is an accurate indicator of the central velocity of the system, is $\simeq 5.1$ km s^{-1}. The dashed line in the figure traces the curve corresponding a the Keplerian velocity law. This particular velocity law was chosen so that it goes through the local maxima in the PV diagram on each half of the disk, as this is the most reliable way to fit the Keplerian behaviour (Gómez & D'Alessio 2000). For a distance to the source of 232 pc, this Keplerian law implies a central stellar mass $M_\star = 0.19 \left[\frac{\sin i}{\sin 43^\circ}\right]^{-1}$ $M_\odot$, where i is the inclination angle of the disk rotation axis with respect to the line of sight. As we expect the jet to align with the disk axis, estimates of the inclination of

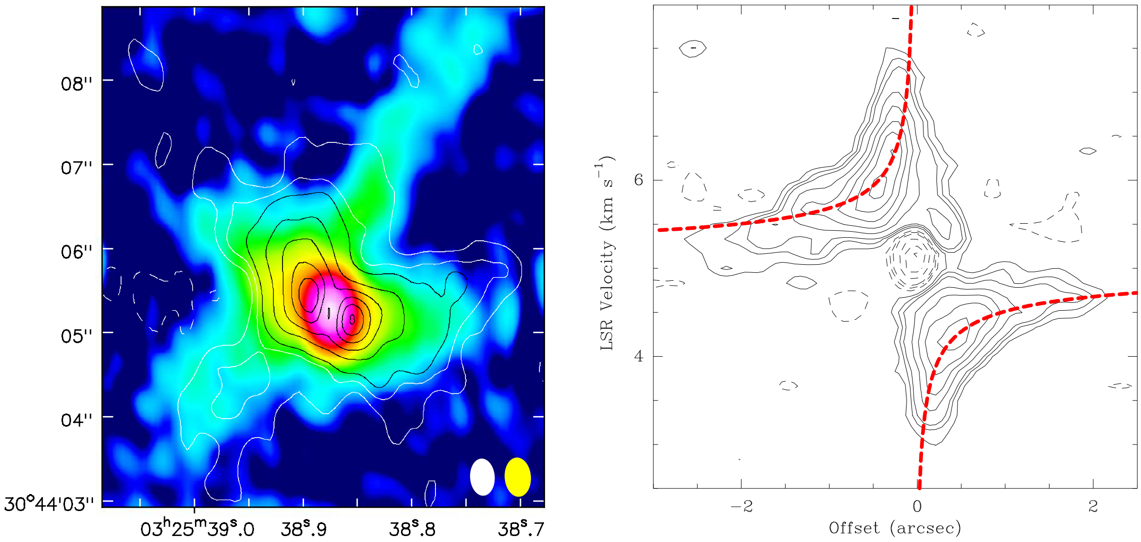

Figure 7.2: Left: Contour map of the integrated intensity of $C^{18}O$(2-1) line emission, superimposed on a color map of the continuum emission (Fig. 7.1). Contour levels are -3, 3, 6 (white) and 9 to 54 at steps of 9 (black) times 2.5 mJy beam^{-1} km s^{-1} (the rms of the map). The white and yellow ellipses at the bottom right corner represent the synthesized beams of the continuum and line emission images, respectively (the beam size of the $C^{18}O$(2-1) line map is $0.46'' \times 0.30''$, P.A.= 4.4°). Right: Position velocity diagram of $C^{18}O$(2-1) emission, along the major axis of the projected disk (position angle = 60°). Contour levels are (in units of mJy beam^{-1}): -6 to -18 with increment step -6, -36 to -72 with increment step -18, 6 to 18 with increment step 6, and 36 to 108 with increment step 18. The rms of the map is 2 mJy beam^{-1}.

the former can be used to constrain the central mass. Despite the uncertainties involved, the inclination angle obtained with VLBI observations of the jet traced by water masers (Hirota et al. 2011), $i = 43^\circ$, is probably the most reliable estimate of the current disk inclination, considering the high positional and kinematical accuracy of these data and that they trace the innermost scales of the jet ($\simeq$ 60 mas). With this inclination angle, the central protostellar mass is $\simeq 0.19$ $M_\odot$.

Other estimates of jet inclination at larger scales have been obtained, but given the possibility of precession (Hirota et al. 2011), they may not accurately reflect the inclination of the disk at present. For instance, Girart & Acord (2001) estimated an inclination of $i \simeq 69^\circ$ from the proper motions in the SiO outflow $\simeq 10''$ from the center (an inclination angle that we recalculate as $\simeq 62^\circ$ using the new distance estimate of 232 pc). At scales $\simeq 20''-30''$, Bachiller et al. (1995) obtained an inclination angle $i \simeq 70^\circ$ from a geometrical modelling of the CO outflow, while Tobin et al. (2007) obtained $i \simeq 49^\circ \pm 8^\circ$ by fitting both the spectral energy distribution and the infrared images. In any case, all these estimates would imply a low central mass (< 0.2 $M_\odot$) considering the Keplerian law we obtained.

In addition to the Keplerian pattern, the PV diagram shows some slightly redshifted material (0.5 km s^{-1} with respect to the central velocity) on the SE half of the disk, at an offset $\simeq 0.29''$ from the center. This could represent foreground accreting material from the envelope onto the disk, or a parcel of outflowing material being launched from the disk.

7.4 Discussion

The most novel result in our data is the detection of a dust jet traced by millimeter continuum emission. This is the first time that thermal dust emission has been detected in a jet, and traced up to its origin from a circumstellar disk. We have thus found a new tracer of jets/outflows in YSOs, probing their dust content rather than gas, and therefore, it can provide a wealth of information that cannot be obtained with the traditional tracers of mass loss. The presence of dust emission can be relevant, for instance, in the derivation of physical parameters of dust in protoplanetary disks, since part of the emission normally attributed to disks can in fact arise from a jet. The detection of dust absorption in the optical by Reiter et al. (2017) was an important step forward in the study of dust in jets, but the detection of millimeter continuum emission opens a new window of opportunity in jet studies. For instance, dust emission can be studied in all sources, while optical absorption requires a bright background, which is present only in particular cases. Moreover, millimeter emission provides quantifiable physical parameters more readily, such as masses, and the dust properties in jets can eventually be derived by observing at different wavelengths, to obtain its spectral energy distribution.

Another important advantage of studying millimeter dust emission a jets is that it is less affected by extinction than optical studies and therefore, we can trace then jets at small scales. In the case of our data in L1448C, we imaged the jet very near its origin, providing key information on the origin of jets. The exact mechanism of jet launching is still debated. While it is clear that a magneto-hydrodynamic process must be at work to power a wind, its details and, in particular, the area from which this wind emerges is not clear. For instance, in the X-wind theory (Shu et al. 1994), the wind is launched close to the stellar surface, whereas in the case of a disk wind (D-wind, Blandford & Payne 1982), it can arise from a larger range of radii along the circumstellar disk. This difference in the launching zone has direct consequences in the wind particle composition that can be proved observationally. MHD mechanisms would accelerate charged particles in the disk-star system, which in their turn can drag neutral particles away from the disk. If part of the wind originates in the disk, outside the dust sublimation radius (dust is sublimated at $T > 1500$ K, occurring roughly at radii < 0.2 au, Panoglou et al. 2012), dust could be found in wind and jets from YSOs. But no dust should be present in jets in the case of an X-wind, powered close to the star. The dust jet in L1448C can be traced back to the keplerian disk itself, with no gap between disk and jet. This strongly indicates that dust is being ripped out of the disk, rather than being environmental entrained material. This implies that at least part of the wind from the protostar-disk system is being launched beyond the dust sublimation radius, as expected in D-wind models.

With this being the first detected case of thermal dust emission in a YSOs jet, it is difficult to ascertain whether this type of dusty jet is widespread, or it is only present in very particular cases. The detection we present here has only been possible with the high sensitivity of ALMA, so it is possible that additional new cases can now be detected. We speculate that the presence of dust emission in jets is favored in the very early stages (Class 0 objects), since the temperature of jets in more evolved YSO is expected to be higher in later phases ($\simeq$ 2000 and 3000 K in Class I and Class II objects, respectively; Panoglou et al. 2012). At such high temperatures the dust would be sublimated.

Another outstanding characteristic in our data is the large size of the Keplerian disk detected with $C^{18}O$. The Keplerian law can be traced up to a radius $\simeq 450$ au. This is the largest keplerian disk ever found in a Class 0 object (Yen et al. 2017; Lee et al. 2018), and such a large size was not expected at these earliest stages (Seifried et al. 2016). Forming a Keplerian disk would require infalling material to overcome magnetic breaking, and the disk radius would subsequently grow with time as the YSO evolved from the Class 0 to Class I stages. From the existing data on Keplerian disks around Class 0 protostars, Yen et al. (2017) fitted a power-law function for the disk radius $R_d \simeq 44 \times \left(\frac{M_\star}{0.1 M_\odot}\right)^{0.8}$ au. For a central protostellar mass of $M_\star = 0.19$ $M_\odot$ au, we should then expect $R_d \simeq 74$ au in L1448C. The significantly larger size of the Keplerian disk in L1448C indicates that disks can form faster than previously thought. In any case, existing data on resolved Keplerian disks around Class 0 and Class I YSO is is still scarce, and firm conclusions about their evolution cannot be established.

In summary, our results in this paper show that dust can be a constituent of protostellar jets, and that (sub)millimeter continuum emission can be a valuable tool to study mass loss in YSOs, complementing the traditional gas tracers. With the high sensitivity and angular resolution of ALMA, this tool can be used to image jets in other star-forming regions, for a complete characterization of the dust content of collimated mass-loss and how they relate to protoplanetary disks.

7.5 Conclusions

We presented continuum emission and $C^{18}O$(2-1) emission at 1.3 cm carried out with ALMA toward the Class O protostar L1448C. We detect, for the first time, thermal dust emission in a protostellar jet. The jet is traced up to its origin in a circumstellar disk. This detection suggests that jets can be powered by disk winds launched from a wide range of radii, even beyond the dust sublimation radius, as proposed in D-wind models. This is in contrast with X-wind models, in which jets are launched close to the star, where dust should not survive. Our results open a new window of study of mass-loss in YSO, since the classical observational tracers of jets and outflows are related to the gas component. We speculate that Class 0 YSOs are the best target to study dusty jets, since the temperature of jets in more evolved objects is expected to be higher ($2000 - 3000$ K), and dust would be sublimated. The $C^{18}O$(2-1) line emission clearly traces a Keplerian disk around L1448C. Its radius ($\simeq$ 450 au) is significantly larger than in other Class 0 objects. This indicates that, at least in some objects, the formation of Keplerian disks is faster than expected.

Chapter 8

Dense gas and exciting sources of the molecular outflow in AFGL 437

8.1 Abstract

We present Very Large Array (VLA) high resolution observations of the $NH_3(1,1)$ and $NH_3(2,2)$ molecular transitions towards the high mass star forming region AFGL 437. Our aim was to investigate if the poorly collimated CO molecular outflow previously detected in the region is the result of a projection effect, with no intrinsic bipolarity, as suggested by Gómez et al. We complemented our observations with radio continuum archived data from the VLA at 2 and 3.6 cm, and with unpublished public data at 450 μm taken with Submillimetre Common-User Bolometer Array at the James Clerk Maxwell Telescope. Ammonia emission was found mainly in three clumps located at the south and east of the position of the compact infrared cluster of AFGL 437, where the CO outflow seemed to have its origin. One of the $NH_3(1,1)$ clumps coincides with the maximum of $NH_3(2,2)$ and with a local peak of emission at 450 μm. A near infrared source (s11) is also found at that position. Our continuum map at 2 cm shows extended elongated emission associated with the infrared source AFGL 437W. This elongated morphology and its spectral index between 3.6 and 2 cm ($\simeq 0.4$) suggest the presence of a jet in AFGL 437W. We suggest that several molecular bipolar outflows may exist in the region. The observed CO outflow would be the superposition of those individual outflows, which would explain its low degree of collimation observed at larger scales.

8.2 Introduction

Mass-loss phenomena are one of the best-known manifestations of the star formation process. In our current understanding of the formation of low-mass stars via accretion

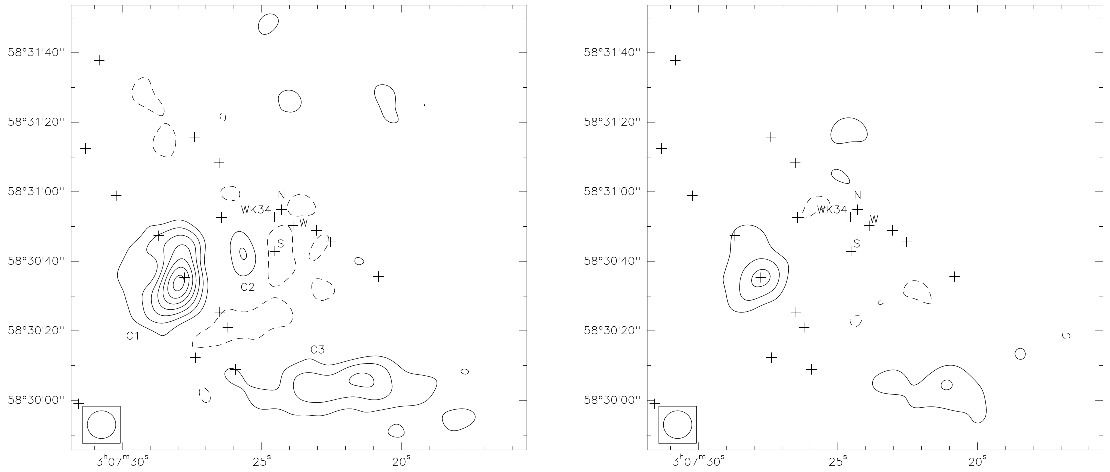

Figure 8.1: Integrated intensity map of the main hyperfine component of the $NH_3(1,1)$ (left) and $NH_3(2,2)$ (right) lines. The lowest contour levels and the increment step are 3 times 5.4 mJy beam^{-1} km s^{-1}, the rms of the map (beam= $8''$, shown at the bottom left-hand corner of each map). Ammonia clumps are labelled as C1, C2, and C3. Crosses mark the position of the infrared sources detected with Spitzer (Kumar Dewangan & Anandarao 2010), of which the better studied ones are labelled. Axes are right ascension and declination in equinox J2000.

(e.g., McKee & Ostriker 2007), highly collimated jets are necessarily present in the first stages of protostellar evolution, coeval with the formation of circumstellar disks. Jets could be the agent releasing angular momentum excess, so that the protostar can continue accreting material from its environment.

Evidence for highly collimated mass-loss is widespread in low-mass young stellar objects (YSOs): e.g., jets traced by Herbig-Haro objects, radio continuum emission, or masers, as well as bipolar molecular outflows. However the case for high-mass stars ($M \geq 8$ $M_\odot$) is less clear. Energetic mass loss is indeed present in those sources, although it is, in general, less collimated than in low-mass objects (Wu et al. 2004). Highly collimated jets seems to be restricted to the earliest phases of the evolution ($< 10^4$ years; Shepherd 2005) of massive YSOs.

This is important from a more global perspective, since it is not yet clear whether high-mass stars form via accretion, like their low-mass counterparts (e.g., Yorke & Sonnhalter 2002; McKee & Tan 2003; Krumholz et al. 2009), or by coalescence of lower-mass objects (Bonnell, Bate & Zinnecker 1998). The presence of circumstellar disks and collimated outflows are key ingredients of the accretion scenario. The detection of disks (Patel et al. 2005) and jets (e.g., Martí, Rodríguez & Reipurth 1993; Rodríguez et al. 1994; Davis et al. 2004; Patel et al. 2005) in several high-mass objects clearly indicate that formation via accretion is possible in these objects, but we still do not know if this process is of general application.

Here we will study the AFGL 437 region, which hosts an interesting molecular outflow. The AFGL 437 region comprises a cluster of at least ~ 20 YSOs (Weintraub & Kastner 1996; Kumar Dewangan & Anandarao 2010), although infrared images are dominated by a compact ($\sim 15''$) central cluster of four sources (named AFGL 437N, S, E, and W by Wynn-Williams et al. 1981), which seem to have recently emerged from the near side of the molecular cloud. AFGL 437 shows clear signs of ongoing star formation, such as the presence of radio continuum emission (probably tracing ultracompact HII regions associated with sources W and S, Wynn-Williams et al. 1981; Torrelles et al. 1992; Kurtz, Churchwell & Wood 1994), water masers (close to sources N and W, Torrelles et al. 1992), and a molecular outflow traced by CO (Gómez et al. 1992). At least sources W and S are thought to be massive stars, of early B type (Wynn-Williams et al. 1981; Torrelles et al. 1992).

The molecular outflow, observed with single dish at $13''$ angular resolution (Gómez et al. 1992), is roughly oriented in the north-south direction, but it shows a very low degree of collimation, with high-velocity CO emission completely surrounding the central cluster. Interestingly, all observed CO isotopes show the same distribution of blue- and red-shifted gas. Given the location of the YSOs close to the edge of the parental cloud, Gómez et al. (1992) suggested a possible interpretation for the nature of the molecular outflow, alternative to more classical models: if the winds from the YSOs, that can be isotropic at the origin, shock obliquely against the walls of the cavity opened in the cloud, they can produce a laminar flow of molecular gas along these walls. When this flow is observed under a particular angle of view, it may give the appearance of a bipolar molecular outflow. The observed bipolarity would then be a projection effect, not an intrinsic characteristic of the mass-loss itself. An alternative explanation for the morphology of the molecular outflow would be the superposition of several outflows excited by different sources in the cluster.

The IR observations showed two different sources towards AFGL 437N (Rayner & McLean 1987; Weintraub & Kastner 1996), one of which (WK 34) is associated with a bipolar polarized nebula (Weintraub & Kastner 1996; Meakin, Hines & Thompson 2005) oriented N-S (i.e., roughly in the same direction as the CO outflow) with a centrosymmetric polarisation pattern. This led Weintraub & Kastner (1996) to suggest that WK 34 is the main driving source of the molecular outflow. However, the nature of this source is still uncertain: while Meakin et al. (2005) argued that it is a low-mass YSO, recent SED modelling including Spitzer data (Kumar Dewangan & Anandarao 2010) suggest that it could be massive, but of young age, with effective temperature still not sufficient to create an HII region. On the other hand, high-resolution infrared observations show elongated (monopolar) emission associated with source AFGL 437S (Alvarez et al. 2004). This suggests that more than one source in the region could be undergoing mass loss.

In this paper we present high resolution ammonia observations of the AFGL 437 region, designed to test whether the bipolarity of the outflow is as a projection effect (as suggested by Gómez et al. 1992) or if, alternatively, the observed outflow is the superposition of individual outflows from different sources. In the case of a projection effect, we should expect the ammonia to show a spatio-velocity pattern similar to that of CO isotopes, with

Table 8.1: Observed properties of NH_3(1,1) clumps.

Clump	R.A.[1] (J2000)	Dec [1] (J2000)	$I(1,1;m)$ [2] (mJy beam^{-1})	$I(1,1;s)$ [3] (mJy beam^{-1})	V_1 [4] (km s^{-1})	ΔV_1 [5] (km s^{-1})	$I(2,2;m)$ [6] (mJy beam^{-1})	V_2 [7] (km s^{-1})	ΔV_2 [8] (km s^{-1})
C1	03 07 27.9	58 30 34	53.3 ± 1.1	18.3 ± 1.1	-41.11 ± 0.02	2.21 ± 0.05	23.4 ± 0.6	-41.04 ± 0.03	1.96 ± 0.07
C2	03 07 25.7	58 30 42	28.8 ± 1.0	12.2 ± 1.1	-40.00 ± 0.02	1.29 ± 0.05	17.6 ± 1.0	-40.19 ± 0.03	0.85 ± 0.06
C3	03 07 21.4	58 30 06	36.7 ± 1.1	13.1 ± 1.7	-40.43 ± 0.02	1.34 ± 0.05	18.7 ± 1.1	-40.42 ± 0.03	1.05 ± 0.07

1. Coordinates of the positions of the local peak in the integrated intensity map of NH_3(1,1) (see Fig. 8.1). Units of right ascension are hours, minutes, and seconds; units of declination are degrees, arcminutes, and arcseconds.
2. Intensity of the main hyperfine component of the NH_3(1,1) line, at that position.
3. Intensity of the inner satellite component of NH_3(1,1).
4. LSR velocity of the NH_3(1,1) line.
5. Full width at half maximum (FWHM) of the main hyperfine component of the NH_3(1,1) line. It was derived from a simple Gaussian fit, without considering the magnetic hyperfine structure within the lines.
6. Intensity of the main hyperfine component of the NH_3(2,2) line.
7. LSR velocity of the NH_3(2,2) line.
8. FWHM of the main hyperfine component of the NH_3(2,2) line.

blueshifted gas to the south and redshifted one to the north. On the other hand, if this is a more classical example of molecular outflow, we expect ammonia emission to peak near the exciting source of the outflow, and possibly tracing a disk/toroid elongated in the E-W direction, i.e., perpendicular to the collimation axis (e.g., Estalella et al. 1993; Wiseman et al. 2001).

We complement the ammonia observations with archival data of continuum emission at centimetre and submillimetre wavelengths to further study the nature of the sources in this region.

8.3 Observations

We observed the (1,1) and (2,2) inversion transitions of the NH_3 molecule (rest frequencies 23694.496 and 23722.634 MHz, respectively) towards the AFGL 437 region, using the Very Large Array (VLA) of the National Radio Astronomy Observatory[1] in its D configuration on 2004 August 16 (project AG665). The phase centre was located at R.A.(J2000) $= 03^h07^m23.7^s$, Dec(J2000) $= 58^\circ30'50''$. We observed both lines simultaneously in dual circular polarisation, using the 4IF mode of the VLA. This allowed us to sample each line with 63 spectral channels of 48.8 kHz (0.62 km s^{-1}) width, centred at $V_{\rm LSR} = -39.4$ km s^{-1}. The flux calibrator was J0137+331, with an assumed flux density of 1.05 Jy using the latest VLA values (1999.2). The phase and bandpass calibrator was J0359+509, with bootstrapped flux density of 9.5 Jy. We calibrated and imaged the data using the standard procedures of the Astronomical Image Processing System (AIPS) of the National Radio Astronomy Observatory (NRAO). Continuum emission was subtracted using task UVLIN. Mapping and deconvolution was carried out with task IMAGR, using a natural weighting

---

[1] The National Radio Astronomy Observatory is a facility of the National Science Foundation operated under cooperative agreement by Associated Universities, Inc.

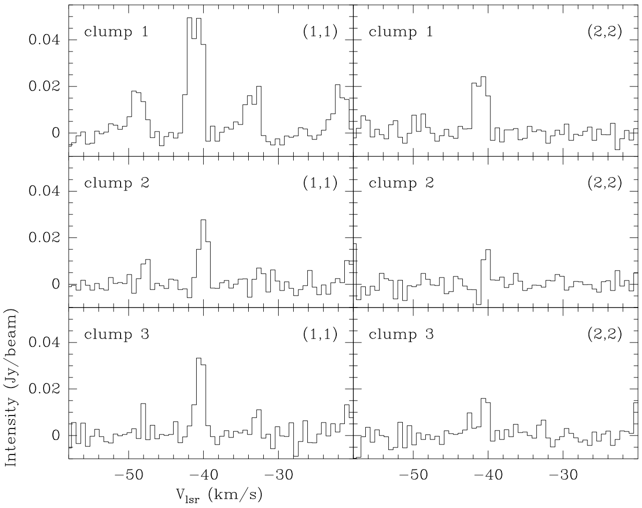

Figure 8.2: Spectra of the NH_3(1,1) and (2,2) lines at the position of the peaks of the clumps shown in Fig. 8.1.

of the visibilities. To improve the signal-to-noise ratio for extended emission we convolved the resulting images with a Gaussian beam, to obtain a final synthesised beam size of $8''$.

We have also reprocessed archival radio continuum data of this region at 2 and 3.6 cm. These observations correspond to VLA projects AC240 (1989 March 19, B configuration), AT121 (1991 May 25, D configuration), and AT122 (1991 January 30, CnD configuration), and were published in Torrelles et al. (1992; projects AT121 and AT122) and Kurtz et al. (1994; project AC240). The description of those observations can be found in these papers. Further self-calibration was possible for the data observed in 1991. We combined together the visibility data at each wavelength before imaging. With this combination we can properly sample the emission at both, larger (as traced by the Torrelles et al. data), and smaller scale (given by the higher-resolution Kurtz et al. data). Imaging of the combined data was carried out with a robust weighting of the visibilities, with robust parameters 0 and 5 for the data at 3.6 and 2 cm, respectively. With these parameters, the final data have a similar size of their synthesised beams ($1.01'' \times 0.84''$ at 3.6 cm, and $1.18'' \times 1.11''$ at 2 cm).

We have also retrieved publicly available submillimetre data at 450 and 850 μm, taken with SCUBA at the James Clerk Maxwell Telescope (JCMT)[2] on 2003 November 6, corresponding to project M03BU13. The data at 850 μm have been presented in Curran & Chrysostomou (2007) and Matthews et al. (2009), but in this paper we are using for our analysis the original data ($\simeq 14''$ angular resolution), without applying any spatial convolution (final angular resolution of $20''$ in Matthews et al. 2009). The data at 450 μm are presented here for first time. The angular resolution of the JCMT at 450 μm is $\simeq 8''$.

---

[2] The James Clerk Maxwell Telescope is operated by the Joint Astronomy Centre on behalf of the Science and Technology Facilities Council of the United Kingdom, the Netherlands Organisation for Scientific Research, and the National Research Council of Canada.

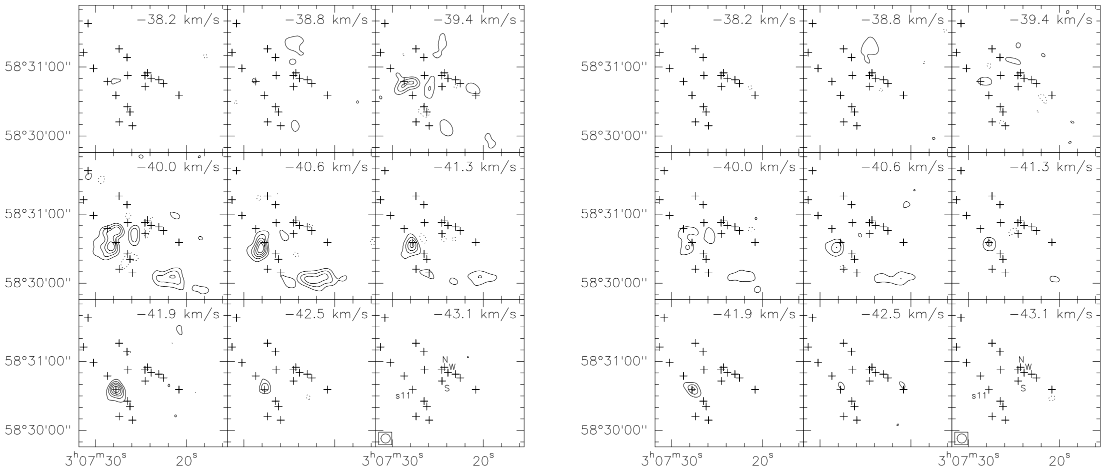

Figure 8.3: Channel maps of the main hyperfine component of the $NH_3(1,1)$ (left) and $NH_3(2,2)$ (right) lines. The lowest contour level and the increment step are 3 times 3.3 mJy beam^{-1}, the rms of the maps (synthesized beam= 8$''$, shown at the bottom left-hand corner of the channel with velocity −43.1 km s^{-1}).

8.4 Results

8.4.1 Ammonia observations

Fig. 8.1 shows the integrated intensity maps of the main hyperfine component of $NH_3(1,1)$ and (2,2) lines. No significant emission is present at the central cluster of stars. Two clumps are clearly present in both maps, to the east and south of the centre (labelled as C1 and C3 in the figures). Their morphology appears elongated, specially in the (1,1) map. The spectra toward the peaks of those clumps are shown in Fig. 8.2. The main and inner satellite components of the electric quadrupole hyperfine structure of the (1,1) transition are evident. A weaker clump (labelled C2) is also visible in the (1,1) map, west from C1. In tables 8.1 and 8.2 we list the observed and the derived physical parameters, respectively, of those three clumps. Line intensities, central positions and widths in Table 8.1 were obtained with Gaussian fits to the emission. Physical parameters in Table 8.2 were obtained following the formulation of Ho & Townes (1983), and Mangum et al. (1992).

Clump C1 (the most intense one in NH_3) appears to have the highest column density. Moreover, its lines are wider than the rest. There is an infrared source, detected in Spitzer IRAC bands (s11, Kumar Dewangan & Anandarao 2010), close to its maximum, at the exact position of the $NH_3(2,2)$ peak. These characteristics may imply that C1 harbours a protostar inside. No infrared source appears clearly associated to the peak of clumps C2 and C3.

Channel maps are shown in Fig. 8.3 for the (1,1) and (2,2) lines. We do not see any obvious velocity pattern within the region, although there is a hint of redshifted emission to the north (see panel at −38.8 km s^{-1}). This would suggest a trend (redshifted to the

Clump	τ_{11}^1	T_R^2 (K)	$N_{H_2}^3$ (10^{22} cm^{-2})	Size^4 (arcsec)	M^5 (M$_\odot$)
C1	0.6	18	1.4	21 × 12	5
C2	1.4	20	0.5	11 × 8	0.7
C3	0.8	19	0.5	40 × 13	4

1. Optical depth of the main hyperfine component of the NH_3(1,1) line.
2. Rotational temperature.
3. Column density of hydrogen, assuming local thermodynamic equilibrium, with kinetic and excitation temperature of NH_3 lines equal to T_R, and an abundance of NH_3 relative to hydrogen of 10^{-8}.
4. FWHM size of the clump.
5. Estimated mass of the clump.

Table 8.2: Physical parameters of NH_3(1,1) clumps.

north, and blueshifted to the south) similar to that found in the CO outflow (Gómez et al. 1992), although the low signal to noise ratio of the emission, apart from clumps C1 and C2 precludes any firm conclusion based on the velocity pattern.

We note that single-dish observations (obtained with the Effelsberg antenna, angular resolution $\simeq$ 40"; Wu et al. 2006) show ammonia emission associated with the central cluster, specially in the (2,2) transition. Since we do not detect this in our observations, it is possible that the emission detected by Wu et al. (2006) is extended and relatively uniform, so that either it is below the sensitivity limit when observed at $8''$ resolution, or a fraction of it is missed because of the lack of short interferometer spacings. To estimate the amount of emission that our interferometric observations are missing, we have convolved our integrated intensity maps with an elliptical Gaussian, to obtain a final angular resolution of $42.2''$, corresponding to that of Effelsberg at the ammonia frequency. We then compared the integrated intensities tabulated by Wu et al. (2006) with the values in our convolved map. At the position given by Wu et al. (2006), the VLA is recovering $\simeq$ 12% and 33% of the NH_3(1,1) and (2,2) emission, respectively. Therefore, we are missing a significant fraction of the NH_3 emission, which would complicate any conclusion based on large-scale structures. However, at smaller scales, we are confident that the individual ammonia clumps seen in Fig. 1 are real structures, given their good correspondence with submillimeter emission (see next section). To get a complete picture of the overall distribution of ammonia map, we should combine both interferometric and single-dish data. Unfortunately, the available single-dish data are not enough to properly carry out such a combination, since the Wu et al. (2006) maps are not fully sampled (their observed points have full-beam separation).

8.4.2 Submillimeter continuum emission

The SCUBA maps at 850 μm presented in Curran & Chrysostomou (2007) and Matthews et al. (2009) showed extended, elongated emission oriented in the northwest-southeast direction. However, in the maps at 450 μm, (Fig. 8.4), we can clearly distinguish two local

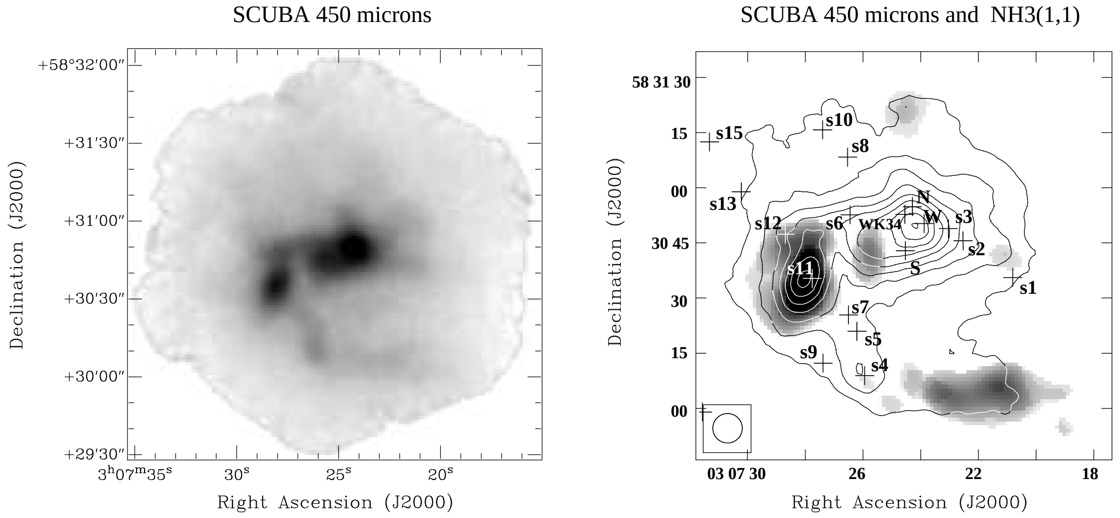

Figure 8.4: (Left) Map of the emission at 450 μm. (Right) An overlaid of 450 μm emission (contours) with integrated emission (greyscale) of the main component of the NH_3(1,1) line. Contours are -5, 5, 10, 15, 20, 25, 30, 35, 40, 45 and 50 times 0.152 Jy beam^{-1}, the rms of the map (beam$\simeq 8''$, shown at the bottom left-hand corner of the right map).

maxima. One of them is located at the position of the central cluster, and the other one coincides with C1 (with its maximum located at R.A.(J2000) = $03^h07^m28.1^s$, Dec(J2000) = $58°30'35''$). We also note that the central submillimeter emission extends to the east, toward C2. There is also a weaker finger of emission elongated toward the south that peaks at the position of the IR source s4 (see Fig. 8.4), and extended, very faint emission coincident with C3. Apart from the central peak, the submillimeter emission tends to follow the distribution of NH_3. This gives us confidence that the ammonia clumps seen in Fig. 8.1 are real entities, and not artifacts generated by the lack of short spacings in the interferometer.

From the map at 450 μm, we can estimate the mass of the observed submillimeter clumps, using the formula $M = S_\nu d^2/(\kappa_\nu B_\nu(T_d))$, where S_ν is the flux density, d is the distance to the source (2 kpc), κ_ν is the mass absorption coefficient, and $B_\nu(T_d)$ is the Planck function for the dust temperature, T_d. The value of κ_ν is highly uncertain, and is very sensitive to the particular dust properties of the object. We have adopted the prescription suggested by Hildebrand (1983), $\kappa_\nu = 0.1(250\mu\mathrm{m}/\lambda)^\beta$ cm^2 g^{-1}, which assumes a gas to dust ratio of 100. To estimate the dust emissivity index (β) we convolved the 450 μm map with an elliptical gaussian, to match the angular resolution of the one at 850 μm. After this convolution, the ratio between those maps is $\simeq$ 9, which yields $\beta \simeq 2.2$, a value within the range found in other high-mass stars (Molinari et al. 2000). With these parameters, flux densities of 6.9 and 5.6 Jy represent masses of 44 and 39 $M_\odot$ for the central submillimeter peak and the one associated with the ammonia clump C1, respectively. In the latter case, the mass obtained from the submillimeter data is larger

Table 8.3: Centimeter radio continuum sources.

Source	$S(3.6cm)^1$ (mJy)	$S(2cm)^2$ (mJy)	$\alpha(3.6-2)^3$
W	22.1 ± 0.7	28.3 ± 2.2	0.4 ± 0.2
S	1.5 ± 0.4	< 2	< 0.5

1. Flux density at 3.6 cm.
2. Flux density at 2 cm.
3. Spectral index between 3.6 and 2 cm, defined as $S_\nu \propto \nu^\alpha$.

than the one from ammonia (5 $M_\odot$), but consistent with our estimate that the ammonia data may be recovering only $\simeq$ 12% of the total flux.

8.4.3 Centimeter continuum emission

Maps of the continuum at 3.6 and 2 cm are shown in Fig. 8.5. As reported previously (Wynn-Williams et al. 1981; Torrelles et al. 1992; Kurtz et al. 1994), there are two main radio continuum sources, as seen in Fig. 8.5, associated with sources AFGL 437W and S. Parameters of the continuum sources are shown in Table 8.3. However, our map at 2 cm shows extended, elongated emission in AFGL 437W, in the NE-SW direction (P.A. $\simeq 60^\circ$). This elongated emission was not clearly seen in the individual datasets that we combined together to obtain this map. It is possible that the elongated structure only shows up with good enough coverage of the uv-plane, which would also explain why it is not seen in the 3.6 cm data. If this interpretation is correct, further observations at 3.6 cm with a better uv-coverage could detect the elongated structure.

The elongated radio continuum emission suggests the presence of a jet, and it is reminiscent of other jets traced by radio continuum in high-mass star-forming regions, like Cepheus A or W75N (Torrelles et al. 1996, 1997). The derived spectral index of this source (0.4 ± 0.2) is similar to that expected from constant-velocity winds ($\simeq 0.6$). Following the formulation by Reynolds (1986), the spectral index would indicate the presence of a confined jet (i.e, narrower than a purely biconical shape). This formulation assumes a power-law dependence of width (w) with distance from the center (r), of the form $w \propto r^\epsilon$. In our case, the derived index is $\epsilon \simeq 0.8$.

The mass loss rate of the ionized jet can be estimated from eq. 19 of Reynolds (1986). We assumed a wind velocity of 500 km s^{-1}, a turnover frequency for the radio continuum emission of 10 GHz, a temperature of the ionized gas of 10^4 K, a jet opening angle of $\simeq 30^\circ$, and an inclination angle with respect to the line of sight of 45°. We have chosen a turnover frequency between the two observed ones, since the derived spectral index (0.4) is partially optically thick. However, the value of the mass loss rate depends only weakly on the turnover frequency (to the power of -0.15), and the possible error introduced by this value is small. Under these assumptions, we obtain a mass-loss rate of $\simeq 5 \times 10^{-6}$ $M_\odot$ yr^{-1}. The assumed velocity of 500 km s^{-1} would imply a momentum rate of $\simeq 2.5 \times 10^{-3}$ $M_\odot$ km s^{-1} yr^{-1} for this jet, which could be enough to drive the large scale CO outflow

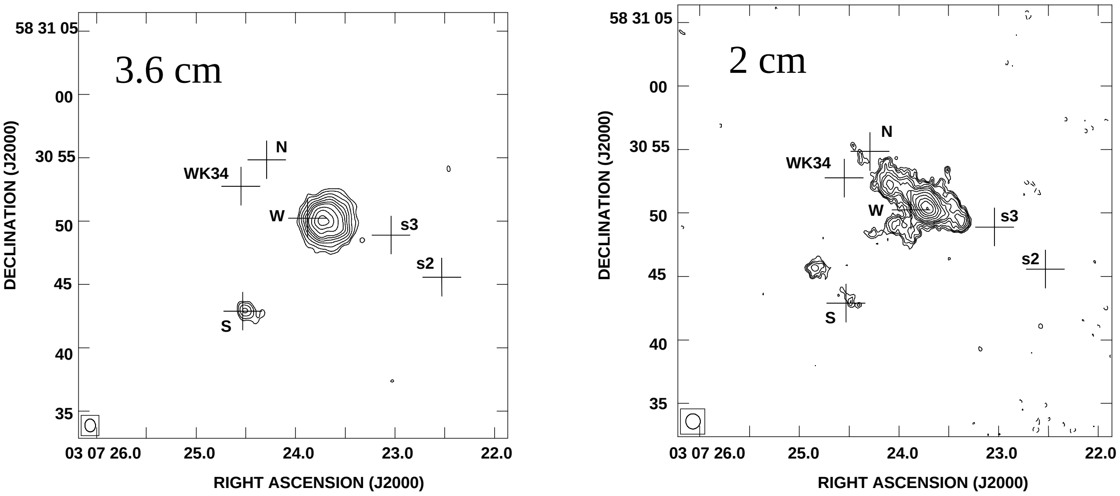

Figure 8.5: (left) Radiocontinuum emission at 3.6 cm in the central cluster of AFGL 437. Contour levels are -4, 4, 6, 10, 15, 20, 25, 30, 40, 50 and 60 times 0.042 mJy beam^{-1}, the rms of the map (beam= $1.01'' \times 0.84''$, shown at the bottom left-hand corner of the map). (Right) Radiocontinuum emission at 2 cm. Contours are -4, 4, 5, 6, 8, 10, 12, 15, 20, 25, 30, 35 and 40 times 0.1034 mJy beam^{-1}, the rms of the map (synthesized beam= $1.18'' \times 1.11''$).

in the region, given that the derived momentum rate of jet and outflow are of the same order (Gómez et al. 1992).

We also note that mid-infrared images of this source (de Wit et al. 2009) show extended emission slightly elongated along the same direction.

In the 2 cm map, there seems to be also some radio continuum emission $\simeq 3.7''$ northeast of AFGL 437S, and an extension to the southeast of AFGL 437W. We have searched in data archive for possible infrared counterparts of those emissions, but none was found. At this point, we cannot ascertain whether these represent two real sources, or they are instrumental artifacts. If they are indeed real sources, the lack infrared counterpart for the weak 2 cm continuum emission may suggest the presence of young, deeply embedded sources. Some weak continuum emission may also be associated with AFGL 437N.

8.5 Discussion

Gómez et al. (1992) suggested an interpretation for the molecular outflow in terms of motions of gas along the wall of a cavity opened in the molecular cloud by the massive stars in the cluster. With this anisotropic distribution of molecular gas, even if the stellar winds are isotropic, the outflow could appear as bipolar, and of low collimation, to the observer.

Our NH_3 observations were specifically designed to test whether this "alternative" interpretation for the outflow is valid, or this is a more "classical" bipolar outflow, where there is intrinsic collimation in the mass-loss process, probably driven by source WK 34. There are several key characteristics to be investigated with these observations, such as the velocity pattern, the morphology, and the location of NH_3.

8.5.1 The velocity pattern of NH_3

If the interpretation given by Gómez et al. (1992) for the outflow, as motions along the walls of a cavity is correct, this drag of material should be seen in all molecular tracers. In particular, the spatial distribution of blue- and redshifted velocities of the dense gas traced by NH_3 should be similar to the one seen in CO.

Our results (Fig. 8.3) are not conclusive to reject the Gómez et al.'s hypothesis. There is some hint of more redshifted gas to the north, and more blueshifted one to the south, but the low signal-to-noise ratio of the emission, specially that to the north does not allow firm conclusions. On the other hand, the most intense ammonia emission (C1) seems to be related to a particular infrared source (s11), which also emits in the submillimeter. The ammonia seems to trace individual clumps, well defined in velocity, rather than a continuous distribution with a velocity gradient, which one could expect from the model proposed by Gómez et al. (1992).

8.5.2 The morphology and location of NH_3

Classical examples of bipolar outflows show interstellar toroids of dense gas, perpendicular to molecular outflows and/or jets (e.g., Torrelles et al. 1983; Wiseman et al. 2001). In the past, these interstellar toroids have been proposed as the collimating agents of these outflows, although the actual collimators seem to be much smaller circumstellar disks. However, given the usual relationship outflow-interstellar toroid, the presence of a dense structure (traced with NH_3) perpendicular to the outflow, and located close to is center, would have favored a more "classical" interpretation of the outflow. Moreover, ammonia emission has been used as a tool to identify the excitation source of bipolar outflows. Excitation source of outflows usually coincides with the maximum emission of ammonia (Anglada et al. 1989). This is usually confirmed with the presence of local enhancements of temperature (with a higher ratio of the emission of ammonia (2,2) to (1,1) transitions), and turbulence (wider ammonia lines).

The overall distribution of NH_3 does not show any preferential orientation with respect to the molecular outflow. Only clump 3 shows an E-W orientation, roughly perpendicular to the outflow. However, it is located to the south, on the blueshifted lobe of the CO emission, rather than towards the central cluster, and no infrared source is located near its maximum.

Using the maximum of ammonia (clump C1) as a criterium to search for the powering source of the outflow, source s11 would be a good candidate. Its spectral energy distribution (Kumar Dewangan & Anandarao 2010) and its distinctive nature as a submillimeter source shows that s11 is a YSO. Nevertheless, source s11 is clearly offset from the center of the outflow, and it is hard to imagine that it could be its main driving source. However, we note that both, the redshifted and blueshifted CO lobes show extensions to the east (Gómez et al. 1992). We suggest that these extensions could in fact be part of an independent outflow driven by source s11, while the bulk of the CO outflow would be driven by the sources in the central cluster.

8.5.3 Sources of mass loss in the region

There are several sources in AFGL 437 that could be undergoing mass-loss simultaneously. Source WK 34 is associated with an infrared polarized nebula (Weintraub & Kastner 1996; Meakin et al. 2005), and has been suggested to be the dominant exciting source of the outflow. The infrared nebula and its association with a water maser (Torrelles et al. 1992; Weintraub & Kastner 1996) clearly indicate that this source is an active source of mass-loss. Source AFGL 437S also shows elongated infrared emission (Alvarez et al. 2004), which is also suggestive of a star undergoing mass-loss, although this extension is weak, and close to the resolution limit of the maps.

Our radio continuum map at 2 cm (Fig. 8.5) shows, for the first time, the presence of a collimated jet associated to source AFGL 437W. The previous detection of both radio continuum and water maser emission (Torrelles et al. 1992) already signaled this source as a young object, but now we see that its mass loss is highly collimated.

Therefore we have strong evidence that at least WK 34 and AFGL 437W (and possibly AFGL 437S) are undergoing collimated mass loss. This seems not to support the model of Gómez et al. (1992), which suggested that the mass loss could be isotropic (and the observed CO bipolarity would be a projection effect). We now favor that the observed CO outflow is the superposition of several bipolar outflows, which would explain its low degree of collimation. Sources WK 34, AFGL 437W (and possibly AFGL 437S) could be responsible for the bulk of high-velocity CO emission close to the center. We also propose that source s11 is a young embedded object that could drive an additional outflow, traced by the eastern extensions of the CO lobes. Weintraub & Kastner (1996) and Kumar Dewangan & Anandarao (2010) noticed that the infrared emission near WK 34 is oriented in the N-S direction next to the source, but it bends to the northeast away from it. Kumar Dewangan & Anandarao (2010) suggested that this bending may be due to the interaction of the outflow from WK 34 with mass loss from source AFGL 437N, but we suggest that it could reflect the interactions between the outflows from WK 34 and AFGL 437W.

This superposition of several individual outflows, giving rise to complex morphologies when observing at low angular resolution, is also found in other high-mass star forming regions (e.g., Beuther et al. 2002, 2006; Ginsburg et al. 2009).

An alternative scenario would be that only one source is significantly driving the (low-collimation) outflow, even when present evidence is of highly collimated jets, if both a collimated jet and a low-collimation wind are driven simultaneously by the same source. Evidence for simultaneous presence of high- and low-collimation mass loss has been found for the first time in a high-mass young star in water maser observations of Cepheus A

(Torrelles et al. 2011).

To test these scenarios, we propose that the molecular outflow should be observed with millimeter/submillimeter interferometers, at scales of a few arcseconds, to be able to discriminate the possible individual outflows driven by these sources. Being able to trace the molecular outflow close to its driving source(s) would provide direct evidence of whether there is a superposition of outflows or if one source is responsible for it.

8.6 Conclusions

We presented new interferometric NH_3(1,1) and (2,2) observations of the region of high-mass star formation AFGL 437, with the aim to understand the nature of the low-collimation bipolar molecular outflow previously detected in CO (Gómez et al. 1992). These observations were complemented with archive data of radio continuum emission at 2 cm, 3.6 cm, and 450 μm. Our main conclusions are as follow:

1. The ammonia emission in our interferometric maps is located mainly in three clumps at the south and east of the central cluster.
2. The analysis of the velocity pattern of the ammonia transitions in the whole region is not conclusive and, in principle, it does not allow us to accept or reject the model proposed by Gómez et al. (1992).
3. One of the clumps seen in NH_3(1,1) coincides with the maximum of NH_3(2,2) emission, and with a local maximum of emission at 450 μm. A near infrared source (s11) is also found at that position. We identify this source as *possible* active young stellar object, and it might be a source of mass-loss in the AFGL 437 region.
4. The radiocontinuum map at 2 cm shows extended, elongated emission in the source AFGL 437W, not detected in previous studies. This elongated morphology and its spectral index ($\simeq 0.4$) suggest the presence of a jet in that source.
5. The collimated mass loss observed in sources WK 34 and AFGL 437W sources does not support the model proposed by Gómez et al. (1992), which suggested an isotropic mass loss in the region.
6. We suggest that several bipolar outflows may exist in the AFGL 437 region. The CO outflow would be the superposition of them, what would explain its low degree of collimation. An alternative scenario is that the CO outflow could be produced by a main source driving both less and highly collimated winds. Observations with millimeter/submillimeter interferometers to scales of several arc seconds may identify the individual outflows.

Chapter 9

Conclusions

In this thesis we studied the physical and chemical properties of a sample of molecular clouds in different evolutionary stages, ranging from pre-stellar cores to active star-forming regions (both of low and high mass). We analyzed the physics, kinematics and chemical evolution of these regions mainly with tracers of dense molecular gas (transitions of the NH_3 and CCS molecules), which provides us with information on the velocity structure, temperature and mass. The comparison between different molecular tracers and clouds in different stages can shed light on the chemical evolution of the molecular gas as star formation proceeds, whether individual molecular lines are reliable tracers of the gas content, and whether the molecular abundance ratios can be used as a clock of cloud evolution.

Most of our data were obtained with interferometers (specially the Very Large Array). The molecular line emission in the regions we studied extend over several arcminutes, which is beyond the field that an interferometer like the VLA can reliably image, we had to use techniques such as mosaicing and combination with single-dish data to improve our maps. We summarize our main conclusions as follows:

- The CCS and NH_3 line emission appears to be spatially anticorrelated in all regions where we observed both molecules, down to the smallest scales we traced ($\simeq 5''$). This happens in starless molecular clouds (TMC-1) and in active star-forming regions (GF9-2 and L1448). The Suzuki et al. (1992) scenario of chemical evolution (with CCS being abundant in early phases and NH_3 in later stages) explain the small scale CCS-NH_3 spatial anticorrelation in most cases, except in L1448C.

- Part of the CCS emission around L1448C shows kinematical signs of interaction of the powerful molecular outflow from this Class-0 protostar. This suggests that CCS abundance may be enhanced due to the interaction of outflows with ambient material, and thus the emission of this molecule can be present in later stages of evolution than assumed in the Suzuki et al. (1992) scenario. This possible regeneration of CCS is similar to the case of B1-IRS previously presented by de Gregorio-Monsalvo et al. (2005). These results suggest that the production and destruction of CCS molecules is a continuous process during the evolution of molecular clouds, and they may be present in a relatively advanced stage of the star-formation process. As a direct consequence of these findings, the abundance ratio [CCS/NH_3] may not be an straightforward clock to date cloud evolution, specially in the presence of molecular outflows.

- The anticorrelation between CCS and NH_3 indicates that neither molecule alone can be used to completely characterize the morphology and kinematics of a molecular cloud. This clearly is illustrated in the region south of L1448C, which shows and accelerating pattern close to the source (traced by NH_3) and a deceleration in the outer areas (traced by CCS). Thus, both molecules are necessary to obtain a complete picture of the properties and physical processes in this molecular cloud.

- Our interferometric NH_3 maps and the CCS single-dish images from other authors show a filamentary structure in core B of the starless region TMC-1. The typical spacing between cores in that filaments ($\simeq 0.1$ pc) is consistent with that expected in models of structure formation from fragmentation of a filament.

- Maps of the mean velocity of NH_3 emission in in GF9-2 shows a possible "blue spot" as defined by Mayén-Gijón et al. (2014). The observed pattern indicates possible infall and rotation motions in the region. This is the first time this "blue spot" effect is found in a low-mass star forming region.

- We did not confirm the presence of water maser emission in GF9-2, reported with single-dish observations. If present, it would be the lowest-luminosity YSO to host this type of emission. In a subsequent search for water maser emission in very low-luminosity YSOs (including proto brown-dwarfs) using the Effelsberg antenna, we also failed to obtain any detection. Our results suggest that the correlation between water maser luminosities and bolometric luminosities does not hold at the lower end of the (sub)stellar mass spectrum. We speculate that there could be a (proto)stellar luminosity threshold below which it is not possible to pump water masers.

- Using ALMA archival data we detected, for the first time, thermal dust emission from a protostellar jet in L1448C. The jet is traced up to its origin in a circumstellar disk. This opens a new window of opportunity in the study of mass-loss in YSO, since it traced the dust component of jets, rather than the gaseous component that is observed in the traditional studies. Moreover, our result suggests that jets can be powered by disk winds launched from a wide range of radii (beyond the dust sublimation radius), as proposed in D-wind models.

- We also detected a Keplerian disk with $C^{18}O$ line emission, with a radius $\simeq 450$ au. This size is significantly larger than other Keplerian disks in Class-0 YSOs, which indicates that the formation of Keplerian disks could be faster than previously expected.

- We tested the model that the low-collimation molecular outflow in AFGL 437 may be the result of the interaction of an isotropic wind interacting with an anisotropic environment, as proposed in Gomez et al. (1992) . However, our results suggest that several bipolar outflows may exist in the AFGL 437 region. The low-collimation CO outflow of this region could be the superposition of them.

Appendix: CCS and NH_3 Column density

We calculated the NH_3 physical parameters following the methods derived by Ho & Townes (1983) and Mangum et al. (1992). The optical depth (τ) of the NH_3 (1,1) transition was estimated with:

$$\frac{T_B(1,1,m)}{T_B(1,1,s)} = \frac{1-\exp[-\tau(1,1,m)]}{1-\exp[-a\tau(1,1,m)]} \tag{1}$$

where T_B is the brightness temperature, m and s indicate the main and satellite component, $\tau(1,1,m)$ is the optical depth of the main component, a is the ratio of the intensity for the satellite to main component ($a = 0.28$ and $a = 0.22$ for the (1,1) satellites). It is assumed equal beam-filling factors and excitation temperatures for the hyperfine components.

The rotational and excitation temperatures (T_r and T_{ex}) were calculated using:

$$T_r = \frac{-41.5}{\ln[\frac{-0.282}{\tau(1,1,m)} \times \ln\{1 - \frac{T(2,2,m)}{T(1,1,m)} \times [1 - e^{-\tau(1,1,m)}]\}]} \tag{2}$$

$$T_{ex} = \frac{-41.5}{\ln\{\frac{-0.283 * \Delta v(2,2)}{\tau(1,1,m)\Delta v(1,1)} \times \ln(1 - \frac{T_B(2,2,m)}{T_B(1,1,m)} \times [1 - e^{-\tau(1,1,m)}])\}} \tag{3}$$

where Δv is the velocity width of the transition in km s^{-1}.

The NH_3 (1,1) and total NH_3 column density are calculated with

$$N(1,1) = 6.60 \times 10^{14} \frac{T_{ex}}{\nu(1,1)} \tau(1,1,m)\Delta v \tag{4}$$

$$N_{TOT}(NH_3) = \frac{N(1,1)Q_{rot}}{(2J+1)g_I g_K} e^{E(J,K)/T_{ex}} \tag{5}$$

where g_I is the nuclear spin degeneracy, g_K is the K-degeneracy, $E(J,K)$ is the energy of the inversion state above the ground state (in kelvins), $\nu(1,1)$ is the transition frequency in GHz, and Q_{rot} is the rotational partition function.

The CCS column density can be obtained from

$$N_{CCS} = \frac{8\pi\nu^3}{c^3 A_{ji} g_j} \frac{Q(T_{rot}) \int I_\nu dv}{[B_\nu(T_{ex}) - B_\nu(T_{bg})]} \frac{e^{E_j/kT_{rot}}}{(e^{h\nu/kT_{ex}} - 1)} \tag{6}$$

Which assumes the optically thin approximation, where ν is the frequency of the transition, Q is the partition function, $\int I_\nu dv$ is the integrated intensity, E_j is the energy of the upper state (1.61 K; Wolkovitch et al.1997), T_{rot} is the rotational temperature, g_j is the statistical weight of the upper rotational level, A_{ji} is the Einstein coefficient for the overall transition (4.33×10^{-7} s^{-1}). The hydrogen column density was obtained assuming a fractional abundance with respect to H_2 of 0.9×10^{-10} for CCS (Lai & Crutcher 2000).

Bibliography

Agra-Amboage, V., Dougados, C., Cabrit, S., & Reunanen, J. 2011, A&A, 532, A59

Aikawa, Y., Ohashi, N., Inutsuka, S.-i., Herbst, E., & Takakuwa, S. 2001, ApJ, 552, 639

Alcalá, J. M., et al. 2014, A&A, 561, A2

Alvarez C., Hoare M., Glindemann A., Richichi A., 2004, A&A, 427, 505

André, P. 1994, The Cold Universe, 179

André, P. 1995, Ap&SS, 224, 29

André, P., Di Francesco, J., Ward-Thompson, D., et al. 2014, Protostars and Planets VI, 27

André, P., Men'shchikov, A., Bontemps, S., et al. 2010, A&A, 518, L102

André, P., & Montmerle, T. 1994, ApJ, 420, 837

André, P., Motte, F., & Bacmann, A. 1999, ApJ, 513, L57

André, P., Ward-Thompson, D., & Barsony, M. 1993, ApJ, 406, 122

André, P., Ward-Thompson, D., & Barsony, M. 2000, Protostars and Planets IV, 59

Andrews, S. M., Liu, M. C., Williams, J. P., & Allers, K. N. 2008, ApJ, 685, 1039

Andrews, S. M., & Williams, J. P. 2005, ApJ, 631, 1134

Anglada, G. 1995, Revista Mexicana de Astronomia y Astrofisica Conference Series, 1, 67

Anglada, G. 1996, Radio Emission from the Stars and the Sun, 93, 3

Anglada, G., Estalella, R., Lopez, R., Rodriguez, L. F., & Canto, J. 1991, A&A, 252, 639

Anglada G., & Rodríguez L. F. 2002, RevMexAA, 38, 13

Anglada, G., Rodriguez, L. F., Canto, J., Estalella, R., & Lopez, R. 1987, A&A, 186, 280

Anglada, G., Rodríguez, L. F., & Carrasco-González, C. 2018, A&ARv, 26, 3

Anglada, G., Rodriguez, L. F., Torrelles, J. M., et al. 1989, ApJ, 341, 208

Arce, H. G., Shepherd, D., Gueth, F., et al. 2007, Protostars and Planets V, 245

Bachiller, R. 1996, ARA&A, 34, 111

Bachiller, R., & Cernicharo, J. 1986, A&A, 168, 262

Bachiller, R., Guilloteau, S., Dutrey, A., Planesas, P., & Martin-Pintado, J. 1995, A&A, 299, 857

Bachiller, R., Martin-Pintado, J., & Fuente, A. 1991, A&A, 243, L21

Bachiller, R., Martin-Pintado, J., Tafalla, M., Cernicharo, J., & Lazareff, B. 1990, A&A, 231, 174

Bachiller, R., & Pérez Gutiérrez, M. 1997, ApJL, 487, L93

Bachiller, R., Pérez Gutiérrez, M., Kumar, M. S. N., & Tafalla, M. 2001, A&A, 372, 899

Bacmann, A., Lefloch, B., Ceccarelli, C., et al. 2003, ApJL, 585, L55

Bajaja, E., & van Albada, G. D. 1979, A&A, 75, 251

Balfour, S. K., Whitworth, A. P., Hubber, D. A., & Jaffa, S. E. 2015, MNRAS, 453, 2471

Bally, J. 2016, ARA&A, 54, 491

Bally, J., & Devine, D. 1994, ApJL, 428, L65

Bally, J., Devine, D., Hereld, M., & Rauscher, B. J. 1993, ApJL, 418, L75

Bally, J., & Lada, C. J. 1983, ApJ, 265, 824

Bally, J., Reipurth, B., & Davis, C. J. 2007, Protostars and Planets V, 215

Barrado, D., Morales-Calderón, M., Palau, A., et al. 2009, A&A, 508, 859

Barrado y Navascués D., & Martín E. L. 2003, AJ, 126, 2997

Barrado y Navascués, D., Stauffer, J. R., Morales-Calderón, M., et al. 2007, ApJ, 664, 481

Barsony, M., Ward-Thompson, D., André, P., & O'Linger, J. 1998, ApJ, 509, 733

Belloche, A., André, P., Despois, D., & Blinder S. 2002, A&A, 393, 927

Benson, P. J., Caselli, P., & Myers, P. C. 1998, ApJ, 506, 743

Benson, P. J., & Myers, P. C. 1989, ApJS, 71, 89

Bergin, E. A., & Langer, W. D. 1997, ApJ, 486, 316

Bergin, E. A., Langer, W. D., & Goldsmith, P. F. 1995, ApJ, 441, 222

Bergin, E. A., & Tafalla, M. 2007, ARA&A, 45, 339

Beuther, H., Churchwell, E. B., McKee, C. F., & Tan, J. C. 2007, Protostars and Planets V, 165

Beuther, H., Kainulainen, J., Henning, T., Plume, R., & Heitsch, F. 2011, A&A, 533, A17

Beuther, H., Ragan, S. E., Johnston, K., et al. 2015, A&A, 584, A67

Beuther, H., Schilke, P., Gueth, F., McCaughrean, M., Andersen, M., Sridharan, T. K., & Menten, K. M. 2002, A&A, 387, 931

Beuther, H., Zhang, Q., Sridharan, T. K., Lee, C.-F., & Zapata, L. A. 2006, A&A, 454, 221

Bilalbegović, G., & Baranović, G. 2015, MNRAS, 446, 3118

Bjerkeli, P., van der Wiel, M. H. D., Harsono, D., Ramsey, J. P., & Jørgensen, J. K. 2016, Nature, 540, 406

Blandford, R. D., & Payne, D. G. 1982, MNRAS, 199, 883

Blitz, L. 1993, Protostars and Planets III, 125

Bolatto, A. D., Wolfire, M., & Leroy, A. K. 2013, ARA&A, 51, 207

Bonnell I. A., Bate M. R., Zinnecker H., 1998, MNRAS, 298, 93

Bontemps, S., André, P., Terebey, S., & Cabrit, S. 1996, A&A, 311, 858

Boogert, A. C. A., Schutte, W. A., Helmich, F. P., Tielens, A. G. G. M., & Wooden, D. H. 1997, A&A, 317, 929

Bourke, T. L., Crapsi, A., Myers, P. C., et al. 2005, ApJL, 633, L129

Bourke, T. L., Myers, P. C., Evans, N. J., II, et al. 2006, ApJL, 649, L37

Bouy, H., Huélamo, N., Pinte, C., et al. 2008, A&A, 486, 877

Brand, J., Cesaroni, R., Comoretto, G., et al. 2003, A&A, 407, 573

Braun, R., & Walterbos, R. A. M. 1985, A&A, 143, 307

Breen, S. L., Caswell, J. L., Ellingsen, S. P., & Phillips, C. J. 2010, MNRAS, 406, 1487

Briceño, C., Calvet, N., Kenyon, S., & Hartmann, L. 1999, AJ, 118, 1354

Bussmann, R. S., Wong, T. W., Hedden, A. S., Kulesa, C. A., & Walker, C. K. 2007, ApJ, 657, L33

Cabrit, S., & Andre, P. 1991, ApJL, 379, L25

Carney, M. T., Yıldız, U. A., Mottram, J. C., et al. 2016, A&A, 586, A44

Carrasco-González, C., Rodríguez, L. F., Anglada, G., et al. 2010, Science, 330, 1209

Chandler, C. J., Terebey, S., Barsony, M., Moore, T. J. T., & Gautier, T. N. 1996, ApJ, 471, 308

Chen, X., Arce, H. G., Zhang, Q., et al. 2010, ApJ, 715, 1344

Chen, H., Myers, P. C., Ladd, E. F., & Wood, D. O. S. 1995, ApJ, 445, 377

Chernin, L. M. 1995, ApJL, 440, L97

Cheung, A. C., Rank, D. M., Townes, C. H., Thornton, D. D., & Welch, W. J. 1968, Physical Review Letters, 21, 1701

Chini, R., Ward-Thompson, D., Kirk, J. M., et al. 2001, A&A, 369, 155

Churchwell, E., Winnewisser, G., & Walmsley, C. M. 1978, A&A, 67, 139

Ciardi, D. R., Woodward, C. E., Clemens, D. P., Harker, D. E., & Rudy, R. J. 1998, AJ, 116, 349

Claussen, M. J., Wilking, B. A., Benson, P. J., et al. 1996, ApJS, 106, 111

Codella, C., Welser, R., Henkel, C., & Benson, P. J., Myers, P. C., 1997, A&A, 324, 203

Comerón, F., Neuhäuser, R., & Kaas, A. A. 2000, A&A, 359, 269

Comerón, F., & Reipurth, B. 2006, A&A, 458, L21

Contreras, Y., Garay, G., Rathborne, J. M., & Sanhueza, P. 2016, MNRAS, 456, 2041

Curiel, S., Raymond, J. C., Moran, J. M., Rodriguez, L. F., & Canto, J. 1990, ApJL, 365, L85

Curiel, S., Torrelles, J. M., Rodríguez, L. F., Gómez, J. F., & Anglada, G. 1999, ApJ, 527,

Curran R. L., Chrysostomou A., 2007, MNRAS, 382, 699

Curry, C. L. 2000, ApJ, 541, 831

Dame, T. M., Hartmann, D., & Thaddeus, P. 2001, ApJ, 547, 792

Davies, J. I., Baes, M., Bianchi, S., et al. 2017, PASP, 129, 044102

Davis, C. J., Dent, W. R. F., Matthews, H. E., Aspin, C., & Lightfoot, J. F. 1994, MNRAS, 266, 933

Davis C. J., Varricatt W. P., Todd S. P., Ramsay Howat S. K., 2004, A&A, 425, 981

De Gregorio-Monsalvo, I., Chandler, C. J., Gómez, J. F., et al. 2005, ApJ, 628, 789

de Gregorio-Monsalvo, I., Gómez, J. F., Suárez, O., et al. 2006, AJ, 132, 2584

de Wit W. J. et al., 2009, A&A, 494, 157

Devine, K. E., Chandler, C. J., Brogan, C., et al. 2011, ApJ, 733, 44

Di Francesco, J., André, P., & Myers, P. C. 2004, ApJ, 617, 425

Di Francesco, J., Johnstone, D., Kirk, H., MacKenzie, T., & Ledwosinska, E. 2008, ApJS, 175, 277

Dickens, J. E., Langer, W. D., & Velusamy, T. 2001, ApJ, 558, 693

Dionatos, O., Nisini, B., Codella, C., & Giannini, T. 2010, A&A, 523, A29

Dionatos, O., Nisini, B., Garcia Lopez, R., et al. 2009, ApJ, 692, 1

Dobashi, K., Yonekura, Y., Mizuno, A., & Fukui, Y. 1992, AJ, 104, 1525

Downes, J. J., Román-Zúñiga, C., Ballesteros-Paredes, J., et al. 2015, MNRAS, 450, 3490

Drabek-Maunder, E., Hatchell, J., Buckle, J. V., Di Francesco, J., & Richer, J. 2016, MNRAS, 457, L84

Dunham, M. M., Chen, X., Arce, H. G., et al. 2011, ApJ, 742, 1

Dunham, M. M., Evans, N. J., II, Bourke, T. L., et al. 2006, ApJ, 651, 945

Dunham, M. M., Evans, N. J., Bourke, T. L., et al. 2010, ApJ, 721, 995

Dutrey, A., Guilloteau, S., & Bachiller, R. 1997, A&A, 325, 758

Edwards, S., Ray, T., & Mundt, R. 1993, Protostars and Planets III, 567

Eislöffel, J. 2000, A&A, 354, 236

Eisloffel, J., & Mundt, R. 1997, AJ, 114, 280

Elitzur, M., 1992, ARA&A, 30, 75

Elitzur, M., Hollenbach, D. J., & McKee, C. F. 1989, ApJ, 346, 983

Endres, C. P., Schlemmer, S., Schilke, P., Stutzki, J., & Müller, H. S. P. 2016, Journal of Molecular Spectroscopy, 327, 95

Enoch, M. L., Lee, J.-E., Harvey, P., Dunham, M. M., & Schnee, S. 2010, ApJ, 722, L33

Estalella R., Mauersberger R., Torrelles J. M., Anglada G., Gómez J. F., Lopez R., Muders D., 1993, ApJ, 419, 698

Fehér, O., Tóth, L. V., Ward-Thompson, D., et al. 2016, A&A, 590, A75

Fernández, M., & Comerón, F. 2001, A&A, 380, 264

Fernández-López, M., Arce, H. G., Looney, L., et al. 2014, ApJL, 790, L19

Flower, D. R., Pineau des Forets, G., & Hartquist, T. W. 1985, MNRAS, 216, 775

Forster, J. R., & Caswell, J. L. 1999, A&AS, 137, 43

Frank, A., Ray, T. P., Cabrit, S., et al. 2014, Protostars and Planets VI, 451

Friesen, R. K., Di Francesco, J., Shirley, Y. L., & Myers, P. C. 2009, ApJ, 697, 1457

Friesen, R. K., Kirk, H. M., & Shirley, Y. L. 2013, ApJ, 765, 59

Froebrich, D. 2005, ApJS, 156, 169

Fukui, Y., Iwata, T., Mizuno, A., Bally, J., & Lane, A. P. 1993, Protostars and Planets III, 603

Furuya, R. S., Kitamura, Y., & Shinnaga, H. 2006, ApJ, 653, 1369

Furuya, R. S., Kitamura, Y., & Shinnaga, H. 2009, ApJL, 692, L96

Furuya, R. S., Kitamura, Y., & Shinnaga, H. 2014a, ApJ, 793, 94

Furuya, R. S., Kitamura, Y., & Shinnaga, H. 2014b, The Labyrinth of Star Formation, 36, 283

Furuya, R. S., Kitamura, Y., Wootten, H. A., Claussen, M. J., & Kawabe, R. 2001, ApJL, 559, L143

Furuya, R. S., Kitamura, Y., Wootten, A., Claussen, M. J., & Kawabe, R. 2003, ApJS, 144, 71

Garay, G., Köhnenkamp, I., Bourke, T. L., Rodríguez, L. F., & Lehtinen, K. K. 1998, ApJ, 509, 768

Garden, R. P., Hayashi, M., Hasegawa, T., Gatley, I., & Kaifu, N. 1991, ApJ, 374, 540

Ginsburg, A. G., Bally, J., Yan, C.-H., & Williams, J. P. 2009, ApJ, 707, 310

Girart, J. M., & Acord, J. M. P. 2001, ApJL, 552, L63

Goldsmith, P. F., Heyer, M., Narayanan, G., et al. 2008, ApJ, 680, 428

Gómez, J. F., & D'Alessio, P. 2000, ApJ, 535, 943

Gomez, M., Hartmann, L., Kenyon, S. J., & Hewett, R. 1993, AJ, 105, 1927

Gómez, J. F., Palau, A., Uscanga, L., Manjarrez, G., & Barrado, D. 2017, AJ, 153, 221

Gómez, J. F., Rizzo, J. R., Suárez, O., et al. 2015, A&A, 578, A119

Gómez J.F., Torrelles J. M., Estalella R., Anglada G., Verdes-Montenegro L., Ho P. T. P., 1992, ApJ, 397, 492

Gómez, G. C., & Vázquez-Semadeni, E. 2014, ApJ, 791, 124

Gomez-Ruiz, A. I., Wyrowski, F., Gusdorf, A., et al. 2013, A&A, 555, A8

Güdel, M., Briggs, K. R., Arzner, K., et al. 2007, A&A, 468, 353

Gueth, F., Bachiller, R., & Tafalla, M. 2003, A&A, 401, L5

Guilloteau, S., Bachiller, R., Fuente, A., & Lucas, R. 1992, A&A, 265, L49

Harju, J., Winnberg, A., & Wouterloot, J. G. A. 2000, A&A, 353, 1065

Hartmann, L. 2002, ApJ, 578, 914

Hartmann, L., Calvet, N., Allen, L., Chen, H., & Jayawardhana, R. 1999, AJ, 118, 1784

Hartmann, L., Herczeg, G., & Calvet, N. 2016, ARA&A, 54, 135

Hartquist, T. W., Williams, D. A., & Caselli, P. 1996, Ap&SS, 238, 30

Hartquist, T. W., Williams, D. A., & Viti, S. 2001, A&A, 369, 605

Henriksen, R., André, P., & Bontemps, S. 1997, A&A, 323, 549

Herbst, E., & Klemperer, W. 1973, ApJ, 185, 505

Herbst, E., & van Dishoeck, E. F. 2009, ARA&A, 47, 427

Heyer, M., & Dame, T. M. 2015, ARA&A, 53, 583

Hildebrand R. H., 1983, QJRAS, 24, 267

Hirahara, Y., Suzuki, H., Yamamoto, S., et al. 1992, ApJ, 394, 539

Hirano, N., Ho, P. P. T., Liu, S.-Y., et al. 2010, ApJ, 717, 58

Hirano, N., Kamazaki, T., Mikami, H., Ohashi, N., & Umemoto T. 1999, in Nakamoto, T., ed. Proc. of Star Formation 1999, Nobeyama Radio Obs., 181

Hirano, N., & Liu, F.-C., 2014, ApJ, 789, 50

Hirota, T., Bushimata, T., Choi, Y. K., et al. 2008, PASJ, 60, 37

Hirota, T., Honma, M., Imai, H., et al. 2011, PASJ, 63, 1

Hirota, T., Sakai, N., & Yamamoto, S. 2010, ApJ, 720, 1370

Ho, P. T. P., & Townes, C. H. 1983, ARA&A, 21, 239

Högbom, J. A. 1974, A&AS, 15, 417

Hogerheijde, M. 1998, Ph.D. Thesis,

Howe, D. A., Taylor, S. D., & Williams, D. A. 1996, MNRAS, 279, 143

Huang, Y.-H., & Hirano, N., 2013, ApJ, 766, 131

Jackson, J. M., Finn, S. C., Chambers, E. T., Rathborne, J. M., & Simon, R. 2010, ApJL, 719, L185

Jeans, J. H. 1902, Philosophical Transactions of the Royal Society of London Series A, 199, 1

Jørgensen, J. K., Harvey, P. M., Evans, N. J., II, et al. 2006, ApJ, 645, 1246

Kahn, F. D. 1974, A&A, 37, 149

Kauffmann, J., Bertoldi, F., Bourke, T. L., et al. 2011, MNRAS, 416, 2341

Kauffmann, J., Bertoldi, F., Bourke, T. L., Evans, N. J., II, & Lee, C. W. 2008, A&A, 487, 993

Kauffmann, J., Bertoldi, F., Evans, N. J., II, & C2D Collaboration 2005, Astronomische Nachrichten, 326, 878

Kenyon, S. J., Dobrzycka, D., & Hartmann, L. 1994, AJ, 108, 1872

Kenyon, S. J., & Hartmann, L. 1995, ApJS, 101, 117

Kim, H. J., Evans, N. J., II, Dunham, M. M., et al. 2011, ApJ, 729, 84

Kirk, J. M., Ward-Thompson, D., Palmeirim, P., et al. 2013, MNRAS, 432, 1424

Klein, R., Apai, D., Pascucci, I., Henning, T., & Waters, L. B. F. M. 2003, ApJ, 593, L57

Klein, R. I., & Woods, D. T. 1998, ApJ, 497, 777

Konigl, A., & Pudritz, R. E. 2000, Protostars and Planets IV, 759

Krumholz M. R., Klein R. I., McKee C. F., Offner S. S. R., Cunningham A. J., 2009, Science, 323, 754

Kuiper, T. B. H., Langer, W. D., & Velusamy, T. 1996, ApJ, 468, 761

Kumar Dewangan L., Anandarao B. G., 2010, MNRAS, 402, 2583

Kurono, Y., Morita, K.-I., & Kamazaki, T. 2009, PASJ, 61, 873

Kurtz S., Churchwell E., Wood D. O. S., 1994, ApJS, 91, 659

Kuznetsova, A., Hartmann, L., & Ballesteros-Paredes, J. 2018, MNRAS, 473, 2372

Kwan, J., & Scoville, N. 1976, ApJL, 210, L39

Kwon, W., Looney, L. W., Crutcher, R. M., & Kirk, J. M. 2006, ApJ, 653, 1358

Lada, C. J. 1985, ARA&A, 23, 267

Lada, C. J. 1987, in Jugaku M. P. J., ed., IAU Symp. 115, Star Formation – From OB Associations to Protostars. D. Reidel Publishing Co, Dordrecht, p. 1

Lai, S.-P., & Crutcher, R. M. 2000, ApJS, 128, 271

Langer, W. D., Velusamy, T., Kuiper, T. B. H., et al. 1995, ApJ, 453, 293

Larson, R. B. 1969, MNRAS, 145, 271

Larson, R. B. 1985, MNRAS, 214, 379

Lee, C. W., Bourke, T. L., Myers, P. C., et al. 2009, ApJ, 693, 1290

Lee, K. I., Dunham, M. M., Myers, P. C., et al. 2015, ApJ, 814, 114

Lee, C. W., Kim, M.-R., Kim, G., et al. 2013b, ApJ, 777, 50

Lee, J., Lee, J.-E., Lee, S., et al. 2013a, ApJS, 209, 4

Lee, C.-F., Li, Z.-Y., Hirano, N., et al. 2018, arXiv:1807.05336

Li, Z.-Y., & Shu, F. H. 1996, ApJ, 472, 211

Little, L. T., MacDonald, G. H., Riley, P. W., & Matheson, D. N. 1979, MNRAS, 189, 539

Lo, K. Y. 2005, ARA&A, 43, 625

Luhman, K. L. 1999, ApJ, 525, 466

Luhman, K. L. 2000, ApJ, 544, 1044

Luhman, K. L., Adame, L., D'Alessio, P., et al. 2007, ApJ, 666, 1219

Luhman, K. L., Briceño, C., Stauffer, et al. 2003, ApJ, 590, 348

Machida, M. N., Higuchi, K., & Okuzumi, S. 2018, MNRAS, 473, 3080

Maddalena, R. J., Morris, M., Moscowitz, J., & Thaddeus, P. 1986, ApJ, 303, 375

Maheswar, G., Lee, C. W., & Dib, S. 2011, A&A, 536, A99

Makin, S. V., & Froebrich, D. 2018, ApJS, 234, 8

Malinen, J., Juvela, M., Rawlings, M. G., et al. 2012, A&A, 544, A50

Mangum, J. G., Wootten, A., & Mundy, L. G. 1992, ApJ, 388, 467

Manjarrez, G., M.S. thesis, UNAM, 2008

Marka, C., Schreyer, K., Launhardt, R., Semenov, D. A., & Henning, T. 2012, A&A, 537, A4

Markwick, A. J., Millar, T. J., & Charnley, S. B. 2000, ApJ, 535, 256

Marti J., Rodríguez L. F., Reipurth B., 1993, ApJ, 416, 208

Martín, E. L., Dougados, C., Magnier, E., et al. 2001, ApJ, 561, L195

Martin-Pintado, J., Bachiller, R., & Fuente, A. 1992, A&A, 254, 315

Matthews B. C., McPhee C. A., Fissel L. M., Curran R. L., 2009, ApJS, 182, 143

Matzner, C. D., & McKee, C. F. 1999, ApJL, 526, L109

Mayén-Gijón, J. M., 2015, Ph.D. Thesis, Universidad de Granada

Mayen-Gijon, J. M., Anglada, G., Osorio, M., et al. 2014, MNRAS, 437, 3766

McKee C. F., Ostriker E. C., 2007, ARA&A, 45, 565

McKee C. F., Tan J. C., 2003, ApJ, 585, 850

McKee, C. F., Zweibel, E. G., Goodman, A. A., & Heiles, C. 1993, Protostars and Planets III, 327

Meakin C. A., Hines D. C., Thompson R. I., 2005, ApJ, 634, 1146

Mocz, P., & Burkhart, B. 2018, MNRAS, in press (arXiv:1805.11105)

Mohanty, S., Jayawardhana, R., & Basri, G., 2005, ApJ, 626, 498

Molinari S., Brand J., Cesaroni R., Palla F., 2000, A&A, 355, 617

Molinari, S., Swinyard, B., Bally, J., et al. 2010, A&A, 518, L100 5

Morata, O., Palau, A., González, R. F., et al. 2015, ApJ, 807, 55

Motte, F., & André, P. 2001, A&A, 365, 440

Mouschovias, T. C. 1987, NATO ASIC Proc. 210: Physical Processes in Interstellar Clouds, 453

Muzerolle, J., Briceño, C., Calvet, N., et al. 2000, ApJ, 545, L141

Muzerolle, J., Hillenbrand, L., Calvet, N., Briceño, C., & Hartmann, L. 2003, ApJ, 592, 266

Muzerolle, J., Luhman, K. L., Briceño, C., Hartmann, L., & Calvet, N. 2005, ApJ, 625, 906

Myers, P. C. 2009, ApJ, 700, 1609

Myers, P. C., & Benson, P. J. 1983, ApJ, 266, 309

Nakano, T. 1998, ApJ, 494, 587

Natta, A., & Testi, L. 2001, A&A, 376, L22

Ohashi, N., Lee, S. W., Wilner, D. J., & Hayashi, M. 1999, ApJL, 518, L41

Olano, C. A., Walmsley, C. M., & Wilson, T. L. 1988, A&A, 196, 194

O'Linger, J., Wolf-Chase, G., Barsony, M., & Ward-Thompson, D. 1999, ApJ, 515, 696

Ortiz-León, G. N., Loinard, L., Dzib, S. A., et al. 2018, ApJ, in press, arXiv:1808.03499

Ossenkopf, V., & Henning, T. 1994, A&A, 291, 943

Palau, A., de Gregorio-Monsalvo, I., Morata, Ò., et al. 2012, MNRAS, 424, 2778

Palau, A., Zapata, L. A., Rodríguez, L. F., et al. 2014, MNRAS, 444, 833

Palmeirim, P., André, P., Kirk, J., et al. 2013, A&A, 550, A38

Palous, J., Tenorio-Tagle, G., & Franco, J. 1994, MNRAS, 270,

Panoglou, D., Cabrit, S., Pineau Des Forêts, G., et al. 2012, A&A, 538, A2

Panopoulou, G. V., Tassis, K., Goldsmith, P. F., & Heyer, M. H. 2014, MNRAS, 444, 2507

Pascucci, I., Apai, D., Henning, T., & Dullemond, C. P. 2003, ApJ, 590, L111

Patel N. A. et al., 2005, Nature, 437, 109

Peng, R., Langer, W. D., Velusamy, T., Kuiper, T. B. H., & Levin, S. 1998, ApJ, 497, 842

Perley, R. A., & Taylor, G. B. 2003, The VLA calibrator manual http://www.vla.nrao.edu/astro/calib/manual/index.shtml

Pety, J., Schinnerer, E., Leroy, A. K., et al. 2013, ApJ, 779, 43

Pezzuto, S., Elia, D., Schisano, E., et al. 2012, A&A, 547, A54

Phan-Bao, N., Lee, C.-F., Ho, P. T. P., & Tang, Y.-W. 2011, ApJ, 735, 14

Pineda, J. E., Arce, H. G., Schnee, S., et al. 2011, ApJ, 743, 201

Podio, L., Eislöffel, J., Melnikov, S., Hodapp, K. W., & Bacciotti, F. 2011, A&A, 527, A13

Podio, L., Kamp, I., Flower, D., et al. 2012, A&A, 545, A44

Pratap, P., Dickens, J. E., Snell, R. L., et al. 1997, ApJ, 486, 862

Preibisch, T., & Zinnecker, H. 2001, AJ, 122, 866

Pudritz, R. E., Ouyed, R., Fendt, C., & Brandenburg, A. 2007, in Protostars and Planets V, ed. B. Reipurth, D. Jewitt, & K. Keil (Tucson, AZ: Univ. Arizona Press), 277

Raga, A. C., Reipurth, B., Castellanos-Ramírez, A., Chiang, H.-F., & Bally, J. 2015, AJ, 150, 105

Rayner J., McLean I., 1987, in Wynn-Williams C. G. and Becklin E.E., eds, Proceedings of the Workshop on Ground-based Astronomical Observations with Infrared Array Detectors, University of Hawaii, Honolulu p. 272

Reid, M. J., & Menten, K. M. 1990, ApJL, 360, L51

Reid, M. J., & Menten, K. M. 1997, ApJ, 476, 327

Reipurth, B., & Bally, J. 2001, ARA&A, 39, 403

Reipurth, B., Bally, J., & Devine, D. 1997, AJ, 114, 2708

Reipurth, B., Heathcote, S., Morse, J., Hartigan, P., & Bally, J. 2002, AJ, 123, 362

Reiter, M., Kiminki, M. M., Smith, N., & Bally, J. 2017, MNRAS, 467, 4441

Reynolds, S. P. 1986, ApJ, 304, 713

Rice, T. S., Goodman, A. A., Bergin, E. A., Beaumont, C., & Dame, T. M. 2016, ApJ, 822, 52

Richer, J. S., Shepherd, D. S., Cabrit, S., Bachiller, R., & Churchwell, E. 2000, Protostars and Planets IV, 867

Rodríguez, L. F. 1995, Revista Mexicana de Astronomia y Astrofisica Conference Series, 1, 1

Rodríguez, L. F., Carral, P., Ho, P. T. P., & Moran, J. M. 1982, ApJ, 260, 635

Rodríguez, L. F., Escalante, V., Lizano, S., Canto, J., & Mirabel, I. F. 1990, ApJ, 365, 261

Rodríguez L. F., Garay G., Curiel S., Ramirez S., Torrelles J. M., Gómez Y., Velazquez A., 1994, ApJ, 430, L65

Rodríguez, L. F., Ho, P. T. P., & Moran, J. M. 1980, ApJL, 240, L149

Rodríguez, L. F., Ho, P. T. P., Torrelles, J. M., Curiel, S., & Canto, J. 1990, ApJ, 352, 645

Rodríguez, L. F., & Reipurth, B. 1994, A&A, 281, 882

Rodríguez-Fernández, N.J., Pety, J., Gueth, F. 2008, IRAM Memo 2008-2,

Rohlfs, K. & Wilson, T. L. 2010, Tools of Radio Astronomy. Springer-Verlag.

Rydbeck, O. E. H., Sume, A., Hjalmarson, A., et al. 1977, ApJL, 215, L35

Sakai, N., Sakai, T., Hirota, T., & Yamamoto, S. 2008, ApJ, 672, 371

Sandell, G., Knee, L. B. G., Aspin, C., Robson, I. E., & Russell, A. P. G. 1994, A&A, 285, L1

Santiago-García, J., Tafalla, M., Johnstone, D., & Bachiller, R. 2009, A&A, 495, 169

Sault, R. J., Staveley-Smith, L., & Brouw, W. N. 1996, A&AS, 120, 375

Schilke, P., Walmsley, C. M., Pineau des Forets, G., & Flower, D. R. 1997, A&A, 321, 293

Schneider, S., & Elmegreen, B. G. 1979, ApJS, 41, 87

Scholz, A., & Jayawardhana, R. 2006, ApJ, 638, 1056

Scholz, A., & Jayawardhana, R. 2008, ApJ, 672, L49

Scholz, A., Wood, K., Wilner, D., et al. 2010, MNRAS, 409, 1557

Schwarz, K. R., Shirley, Y. L., & Dunham, M. M. 2012, AJ, 144, 115

Seifried, D., Sánchez-Monge, Á., Walch, S., & Banerjee, R. 2016, MNRAS, 459, 1892

Seo, Y. M., Shirley, Y. L., Goldsmith, P., et al. 2015, ApJ, 805, 185

Seth, A. C., Greenhill, L. J., & Holder, B. P. 2002, ApJ, 581, 325

Shang, H., Li, Z.-Y., & Hirano, N. 2007, Protostars and Planets V, 261

Shepherd D., 2005, in Cesaroni R., Felli M., Churchwell E., Walmsley M., eds, Proc. IAU Symp. 227, Massive Star Birth: A Crossroads of Astrophysics, Cambridge University Press, Cambridge, p. 237

Shirley, Y. L., Claussen, M. J., Bourke, T. L., Young, C. H., & Blake, G. A. 2007, ApJ, 667, 329

Shirley, Y. L., Evans, N. J., II, Rawlings, J. M. C., & Gregersen, E. M. 2000, ApJS, 131, 249

Shu, F. H., Adams, F. C., & Lizano, S. 1987, ARA&A, 25, 23

Shu, F., Najita, J., Ostriker, E., et al. 1994, ApJ, 429, 781

Shu, F. H., Najita, J. R., Shang, H., & Li, Z.-Y. 2000, Protostars and Planets IV, 789

Snell, R. L., Loren, R. B., & Plambeck, R. L. 1980, ApJL, 239, L17

Stanimirovic, S. 2002, Single-Dish Radio Astronomy: Techniques and Applications, 278, 375

Stecklum, B., Melnikov, S. Y., & Meusinger, H. 2007a, A&A, 463, 621

Stecklum B., Meusinger H., & Froebrich D., 2007b, Ap&SS, 311, 63

Sunada, K., Nakazato, T., Ikeda, N., et al. 2007, PASJ, 59, 1185

Suzuki, H., Yamamoto, S., Ohishi, M., et al. 1992, ApJ, 392, 551

Tafalla, M., Santiago, J., Johnstone, D., & Bachiller, R. 2004, A&A, 423, L21

Tafalla, M., Santiago-García, J., Hacar, A., & Bachiller, R. 2010, A&A, 522, A91

Tafalla, M., Santiago-García, J., Myers, P. C., et al. 2006, A&A, 455, 577

Taylor, G. B., Carilli, C. L., & Perley, R. A. 1999, Synthesis Imaging in Radio Astronomy II, 180,

Terebey, S., Shu, F. H., & Cassen, P. 1984, ApJ, 286, 529

Testi, L., Natta, A., Scholz, A., et al. 2016, A&A, 593, A111

Thompson, A. R., Moran, J. M., & Swenson, G. W., Jr. 2001, Interferometry and synthesis in radio astronomy, 2nd ed. New York, Wiley, 692 p.

Thronson, H. A., Jr., Lada, C. J., & Hewagama, T. 1985, ApJ, 297, 662

Tobin, J. J., Looney, L. W., Li, Z.-Y., et al. 2016, ApJ, 818, 73

Tobin, J. J., Looney, L. W., Mundy, L. G., Kwon, W., & Hamidouche, M. 2007, ApJ, 659, 1404

Tobin, J. J., Looney, L. W., Wilner, D. J., et al. 2015, ApJ, 805, 125

Toelle, F., Ungerechts, H., Walmsley, C. M., Winnewisser, G., & Churchwell, E. 1981, A&A, 95, 143

Torrelles J. M. et al., 2011, MNRAS, 410, 627

Torrelles J. M., Gómez J. F., Anglada G., Estalella R., Mauersberger R., Eiroa C., 1992, ApJ, 392, 616

Torrelles, J. M., Gómez, J. F., Rodríguez, L. F., et al. 1996, ApJL, 457, L107

Torrelles, J. M., Gómez, J. F., Rodríguez, L. F., et al. 1997, ApJ, 489, 744

Torrelles, J. M., Gómez, J. F., Rodríguez, L. F., et al. 1998, ApJ, 505, 756

Torrelles, J. M., Patel, N. A., Gómez, J. F., et al. 2001, ApJ, 560, 853

Torrelles J. M., Rodríguez L. F., Cantó J., Carral P., Marcaide J., Moran J. M., Ho P. T. P., 1983, ApJ, 274, 214

Torrelles, J. M., Trinidad, M. A., Curiel, S., et al. 2014, MNRAS, 437, 3803

Torres, R. M., Loinard, L., Mioduszewski, A. J., & Rodríguez, L. F. 2007, ApJ, 671, 1813

Uchida, Y., Mizuno, A., Nozawa, S., & Fukui, Y. 1990, PASJ, 42, 69

Ungerechts, H., & Thaddeus, P. 1987, ApJS, 63, 645

Ungerechts, H., Winnewisser, G., & Walmsley, C. M. 1982, A&A, 111, 339 van Boekel, R., Ábrahám, P., Correia, S., et al. 2006, Proceedings of the SPIE, 6268, 62680D

van Dishoeck, E. F., & Blake, G. A. 1998, ARA&A, 36, 317

Velusamy, T., Kuiper, T. B. H., & Langer, W. D. 1995, ApJL, 451, L75

Vogel, S. N., Wright, M. C. H., Plambeck, R. L., & Welch, W. J. 1984, ApJ, 283, 655

Volgenau, N. H., Mundy, L. G., Looney, L. W., & Welch, W. J. 2006, ApJ, 651, 301

Wang, J.-J., Chen, W.-P., Miller, M., Qin, S.-L., & Wu, Y.-F. 2004, ApJL, 614, L105

Wang, L.-Y., Shang, H., Su, Y.-N., et al. 2014, ApJ, 780, 49

Wang, H., Yang, J., Wang, M., et al. 2001, AJ, 121, 1551

Watson, D. M., Calvet, N. P., Fischer, W. J., et al. 2016, ApJ, 828, 52

Weintraub, D. A. 1990, ApJS, 74, 575

Weintraub D. A., Kastner J. H., 1996, ApJ, 458, 670

Whelan, E. T., Ray, T. P., Bacciotti, F., et al. 2005, Nature, 435, 652

Whelan, E. T., Ray, T. P., Randich, S., et al. 2007, ApJ, 659, L45

White, R. J., Greene, T. P., Doppmann, G. W., Covey, K. R., & Hillenbrand, L. A. 2007, Protostars and Planets V, 117

White, R. J., & Hillenbrand, L. A. 2004, ApJ, 616, 998

Wiesemeyer, H. 1997, Ph.D. Thesis,

Wiesemeyer, H., Cox, P., Gusten, R., & Zylka, R. 1999, The Universe as Seen by ISO, 427, 533

Wiesemeyer, H., Gusten, R., Cox, P., Zylka, R., & Wright, M. C. H. 1998, Star Formation with the Infrared Space Observatory, 132, 189

Williams, J. P., & Cieza, L. A. 2011, ARA&A, 49, 67

Wiseman J., Wootten A., Zinnecker H., McCaughrean M., 2001, ApJ, 550, L87

Wolf-Chase, G. A., Barsony, M., & O'Linger, J. 2000, AJ, 120, 1467

Wolkovitch, D., Langer, W. D., Goldsmith, P. F., & Heyer, M. 1997, ApJ, 477, 241

Wu, Y., Wei, Y., Zhao, M., et al. 2004, A&A, 426, 503

Wu Y., Zhang Q., Yu W., Miller M., Mao R., Sun K., Wang Y., 2006, A&A, 450, 607

Wynn-Williams C. G., Becklin E. E., Beichman C. A., Capps R., Shakeshaft J. R., 1981, ApJ, 246, 801

Yamaguchi, T., Takano, S., Watanabe, Y., et al. 2012, PASJ, 64,

Yates, J. A., Field, D., & Gray, M. D. 1997, MNRAS, 285, 303

Yen, H.-W., Koch, P. M., Takakuwa, S., et al. 2015, ApJ, 799, 193

Yen, H.-W., Koch, P. M., Takakuwa, S., et al. 2017, ApJ, 834, 178

Yorke H. W., Sonnhalter, C., 2002, ApJ, 569, 846

Young, C. H., Bourke, T. L., Young, K. E.,et al. 2006, AJ, 132, 1998

Young, C. H., Jørgensen, J. K., Shirley, Y. L., et al. 2004, ApJS, 154, 396

Young, C. H., Shirley, Y. L., Evans, N. J., II, & Rawlings, J. M. C. 2003, ApJS, 145, 111

Yung, B. H. K., Nakashima, J.-I., Imai, H., et al. 2011, ApJ, 741, 94

Zapata, L. A., Schmid-Burgk, J., Muders, D., et al. 2010, A&A, 510, A2

Zinnecker, H., & Yorke, H. W. 2007, ARA&A, 45, 481

Zuckerman, B., Kuiper, T. B. H., & Rodriguez Kuiper, E. N. 1976, ApJL, 209, L137

Part of the results of this thesis have already been published in international refereed journals. In particular:

- The contents of Chapter 5 can be found in
  "A Search for Water Maser Emission from Brown Dwarfs and Low-luminosity Young Stellar Objects", Gómez, José F.; Palau, Aina; Uscanga, Lucero; Manjarrez, Guillermo; Barrado, David, 2017, The Astronomical Journal, 153, 221.
- The contents of Chapter 8 can be found in
  "Dense gas and exciting sources of the molecular outflow in the AFGL 437 star-forming region", Manjarrez, G.; Gómez, J. F.; de Gregorio-Monsalvo, I., 2012, Monthly Notices of the Royal Astronomical Society, 419, 3338.